N° Ordre……../Faculté/UMBB/2015

REPUBLIQUE ALGERIENNE DEMOCRATIQUE ET POPULAIRE

MINISTERE DE L'ENSEIGNEMENT SUPERIEUR ET DE LA RECHERCHE SCIENTIFIQUE

UNIVERSITE M'HAMED BOUGARA-BOUMERDES

Faculté des **S**ciences de l'**I**ngénieur

Thèse de Doctorat

Présentée par

BENIAICHE Ahmed

Filière : Génie Mécanique
Option : Systèmes Energétiques Avancés

Analyse Expérimentale et Simulation CFD en Vue de l'Etude du Refroidissement des Aubes Rotor/Stator : Cas d'une Turbine à Gaz

---

Soutenue publiquement le : 27 juin 2015.

Devant le jury :

MANSOURI	Kacem	Prof/ UMBB	Président
LIAZID	Abdelkrim	Prof/ ENP Oran	Examinateur
BALISTROU	Mourad	MC. A/ UMBB	Examinateur
HACHEMI	Madjid	MC. A/ UMBB	Examinateur
GHENAIET	Adel	Prof / USTHB	Encadreur
FACCHINI	Bruno	Prof /Florence/Italie	Co-Encadreur
HANOUNE	Noureddine	MC. A/ USTHB	Invité

Année Universitaire: 2014/2015

Bibliography of the candidate:

(a) International Publications In Journals:

1) **TLC Measurements of Heat Transfer Under Rotating Conditions at High Reynolds Number in an Innovative Trailing Edge Cooling System.**
Proceedings of ASME/ Thermal**.**
Paper pp: 413-422, 10 pages.
ISBN: 978-0-7918-4516-5.
DOI: 10.1115/GTINDIA2012-9560.

2) **Nusselt Correlations In Trailing Edge Cooling System With Long Pedestals And Ribs.**
Energy Procedia Journal, Vol. 45 (2014): 1067-1076
ISSN: 1876-6102.
DOI: 10.1016/j.egypro.2014.01.112.

3) **Contribution to Correlate the Nusselt Number in three Cooling Configurations of the Trailing Edge of an Innovative HP NGV.**
Thermal science, Elsevier, 18 page
ISSN: 1290-0729.

4) **Experimental study of a trailing edge cooling system of a rotating gas turbine blade.**
Power and Energy, Imeche part A
ISSN: 0957-6509. pp: 17 pages.
DOI: 10.1177/0957650915594715

(b) International and National Conferences With Reviewers Comities:

1) **TLC Measurements of Heat Transfer Under Rotating Conditions at High Reynolds Number in an Innovative Trailing Edge Cooling System.**
ASME TuboExpo Conference, Mumbai, India 2012.

2) **Nusselt correlations in trailing edge cooling system with long pedestals and ribs.**
ATI 2013, Bologna, Italy 2013.

3) **Contribution to the Estimation of the Nusselt Number AT the Trailing Edge Region of An innovative Blade cooling Geometry Open Tip case.**
9 JM EMP, Algeria 2014

4) **Experimental and Numerical Investigation of Heat Transfer In Innovative Leading Edge Geometry of Blade.**
International conference of heat and mass transfer ICHMT2015, Istanbul, Turkey 2015

Dedication

First, I thank God Almighty for giving me this strength that allowed me to complete this

work, despite the hardships I had during this period

One day I'll be successful and people will ask me which college I went to. I'll say, 'it doesn't matter because it is my parents who made me what I am today'.

Yes: Mom and Dad, even though you are a generation older, even though you are my parents… you both have been the best friends I could ever have had. Thanks mom and dad,

I promise to achieve all the dreams of your life that you couldn't, because you were busy making sure that I achieved mine,

You sacrificed your own happiness, just so that I could be happy. It may take a lifetime, but I'll do everything to repay for what you have done for me. Thanks mom and dad,

I may dedicate this work for you, dears mom and dad.

I dedicate also this

work to my dear wife, thank you for being here for me, for being so

patient and comprehensive,

No words can express my gratitude, acknowledgements and respect, because without you and your support, I couldn't make it that far,

Thanks again for everything you did and you continue to do, to make my life a pure happiness.

My dears two brothers and my darling unique sister,
I love you all of you, for everything we've shared together, for all the joy and sadness we had, for all little things we did and we didn't, you are my dearest persons in this world, as brothers and sister, I only express my great love for you, thank you.

To my little source of joy and light of life, my darling daughter. May God bless you
my little dear new arriving; my son, this is also for you both of you.

To the memory of my grandmother Dahbia.

Finally, I express my acknowledgements to all those who were supporting me, thank you all of you.

Acknowledgements

My Acknowledgements go to Pr. Adel GHENAIET for being my teacher since I was in graduate, and later for accepting to direct my thesis work.

My Acknowledgements go to Pr. André LALLEMAND and His wife Pr. Monique LALLEMAND for their help. Without their recommendation I wouldn't be able to go to Florence. Thank you very much.

Special acknowledgements go to Pr. Bruno FACCHINI from the University of Florence for accepting co-directing my thesis and giving me the opportunity to be a member his team work. No words can express my gratitude

Pr. Carlo CARCASCI thank you for your assistance and help. I really appreciated all critics you gave to me. Thank you again.

My gratitude goes to the Jury members. It is a great honour to accept judging my work. I've been your student and I'll be forever yours, Thank you.

My Acknowledgements go to all the staff members' of the Department of Industrial Energy Engineering, University of Florence: Dr. A. Andreini, Dr. L. Tarchi, Dr. L. Bonnani, Dr. F. Maiuolo, Dr. A. Picchi, my dear friend Dr. Marco Pievaroli (Marchino!). Without your help this work could not be achieved. Thank you for being helpful and kind.

At last, but not least, my recognitions go to miss Alda Vecchi, my 73 years old Italian teacher. Thank you for your help to make my laboratory research stays easy and fine.

At least; my thanks go to my dear friends and colleagues of the laboratory of energetic systems, and Ecole Militaire Polytechnique, for their kindness and support.

ملخص.

تم تقييم الخصائص الهوائية الحرارية لحافة ذنب خاص بنظام التبريد الداخلي لشفرة تربين غازي من خلال التجريب و المحاكاة العددية في ظروف السكون و الدوران. النموذج المدروس يكمن في نسخة قياس 30 إلى1 مطابقة لممر بدون و بوجود مولدات الاضطراب مع وجود صف من 7 أعمدة عريضة.

تم إختبار ستة نماذج من أجل عدد *رينولدس بين 10000 و 40000 و* عدد روزبي حتى 0,23 .التجارب تم إجراؤها باستعمال تقنية البلورات السائلة ذات قاعدة كرومية حرارية و بالمقابل تم إختيار طريقة المعادلات المتوسطة لراينولدس ونافيي- ستوكس بإستعمال البرنامج Ansys Fluent و نموذج $k\ \omega$ – SST لتمثيل الإضطراب مع تدفق الهواء في حالة إستقرار متساوي الحرارة داخل الممرات في ظروف السكون و الدوران .

النتائج المحصل عليها تم عرضها في شكل مخطط ثنائي الأبعاد لتوزيع معامل التبادل الحراري من جهة السطح إضافة إلى اقتراح علاقات إرتباط عدد نوسلت المتوسط كدالة ذات متغيرات: هي عدد راينولدس و عدد براندل و عدد روزبي و مسافة لا بعدية. النتائج المحصل عليها تعتبر ذات أهمية كبيرة للمصممي الشفرات التربينية الغازية.

كلمات مفتاحية: البلورات السائلة ذات قاعدة كرومية حرارية ، نظام تبريد داخلي للشفرات التربينية ، حافة الذنب لشفرة تربينية، معامل التبادل الحراري، عدد نوسلت، عدد راينولدس، عدد روزبي، التحليل العددي لديناميكا الموائع.

Résumé :

Les performances aérothermiques d'un système de refroidissement interne du bord de fuite d'une aube de turbine à gaz sont évaluées expérimentalement et numériquement dans les conditions stationnaires et rotatives. La géométrie étudiée est un modèle à échelle 30 : 1 représentative d'une conduite sans et avec perturbateurs avec une ligne de 7 vannes élargies.

Six géométries sont testées par le moyen de la technique TLC pour un nombre de Reynolds entre 10000-40000 et un nombre de Rotation jusqu'à 0.23. En outre, l'analyse CFD est basée sur ANSYS-Fluent et un modèle de turbulence $k\,\omega-$ SST tout en considérant un écoulement d'air iso-thermique stationnaire à l'intérieur de la géométrie étudiée pour les conditions fixes et rotatives.

Les résultats sont présentés sous forme de cartes 2D illustrant le coefficient d'échange thermique sur la surface en dépression, en plus de corrélations pour le nombre de Nusselt moyenné en fonction de Re, Pr, Ro et une fraction de la hauteur de l'aube. Les résultats obtenus sont d'un grand intérêt pour les concepteurs des systèmes de refroidissement pour les aubes de turbines à gaz.

Mots clés: Cristaux Liquides Thermo-chromiques, Système de refroidissement interne des aubes, Bord de fuite d'une aube, Coefficient d'échange thermique, Nombre de Nusselt, Nombre de Reynolds, Nombre de rotation, CFD.

Abstract:

The aerothermal performances of a trailing edge internal cooling system of a high pressure gas turbine blade were evaluated experimentally and numerically in the stationary and rotating conditions. The investigated geometry consists in a 30:1 scaled model reproducing an innovative typical wedge shaped discharge ribbed duct, with one row of 7 enlarged pedestals.

Six different cooling schemes were tested based on TLC technique, at Reynolds number in between 10000-40000 and Rotation number up to 0.23. On the other hand, CFD analysis used commercial ANSYS-Fluent solver based on $k\,\omega-$SST turbulence model and an isothermal steady air flow inside the studied geometry for both the stationary and rotating conditions.

The obtained results are reported in terms of 2D maps of HTC plotted on the suction side surface and correlations of averaged Nusselt number as function of *Re, Pr, Ro* and a fraction of the blade hight. The obtained results are useful to the designers of gas turbine blades cooling systems.

Keywords: Thermo-chromic liquid crystals, Blade internal cooling, Blade trailing edge, , Heat transfer coefficient, Nusselt Number, Reynolds number, Rotation number, CFD.

Contents

List of figures

List of tables:

Nomenclature

A_h	Inlet section area [mm^2]
#Å	A given region
D_h	Hydraulic diameter [mm]
D	Distance from pedestal's leading edge to inlet section [mm]
d_p	Pedestal width [mm]
d_t	Pedestal thickness [mm]
d_r	Pedestal's distance in model's radial direction [mm]
e	Rib height [mm]
h	Heat transfer coefficient [$W\,m^{-2}K^{-1}$]
H_1	Initial duct height [mm]
Hz	Frequency [Hertz]
i	Line of matrix
j	Column of matrix
k	Thermal conductivity [$W\,m^{-1}K^{-1}$] or Turbulence kinetic energy [m^2s^{-2}]
dl	Pedestal length [mm]
U_b	Bulk velocity defined at the inlet section [ms^{-1}]
u	x Velocity component [ms^{-1}]
v	Normal velocity component [ms^{-1}]
w	Axial velocity component [ms^{-1}]
Nu	Nusselt number [--]
$\overline{Nu_{\#}}$	Averaged Nusselt number of the # inter pedestal region [--]
Nu_{st}	Static Nusselt number [--]
$\frac{Nu}{Nu_{st}}$	Nusselt ratio [--]
P	Pressure [Pa]
P_x	Pitch inter-pedestals distance [mm]
Pr	Prandtl number [--]
P_x/e	Pitch to rib height ratio [--]
$\dot{q}$	Heat flux density [$W\,m^{-2}$]
R_x	Local radius [mm]
Re	Reynolds number [--]
Ro	Rotation number [--]

s	Blade thickness [mm]
T	Temperature [$°C$ *or* K]
T_{co}	Coolant air temperature at the inlet section [$°C$ *or* K]
V	Velocity [ms^{-1}]
x	Radial direction [--]
x/P_x	Dimensionless position [--]
y	Rotation axis direction [--]
y^+	Dimensionless wall distance [--]
z	Axial direction [--]

Greeks

α	Wedge angle of the inclined wall [deg]
ε	Turbulent dissipation
μ	Viscosity [kg m^{-1} s^{-1}]
ρ	Density of coolant [$kg.m^{-3}$]
ω	Eddy frequency (s^{-1})
Ω	Angular velocity [rad s^{-1}]

Acronyms

HTC	Heat Transfer Coefficient
i_{max}	Line ‘s local matrix size
j_{max}	Column’s local matrix size
AR	Aspect ratio
LE	Leading edge
LESs	Large Eddy Simulation
$L0$	Inlet duct region
$L1$	Trailing edge region
PMMA	Poly Methyl Methacrylate
RANS	Reynolds-averaged Navier–Stokes simulation
TLC	Thermochromic Liquid Crystal

Subscripts

co	Coolant
f	Film

for	Forced convection
hub	The hub region
in	Inlet
loss	Conduction losses
max	Maximum
meanX	Correspond to the mean *x* line
meanY	Correspond to the mean *y* line
meanZ	Correspond to the mean *z* line
nat	Natural
ro	Referred to ambient conditions
stat	Stationary
tip	Tip region
w	Wall

Abstract about the thesis work

The trailing edge is one of the most thermally loaded regions of a gas turbine blade that requires more complex cooling scheme to maintain its metal temperature at a level consistent with the component life span. For decades, lot of experimentations have been carried out to understand the heat transfer behaviour at this region of a blade. In this thesis, a 30:1 scaled model of an innovative wedge shaped discharging trailing edge cooling system, composed of seven enlarged pedestals is studied using the non-intrusive thermo-chromic liquid crystals technique TLC to measure the heat transfer coefficient for smooth, +60° and −60° ribbed surfaces with both closed tip and open tip.

The results are reported in terms of detailed 2D maps of HTC on the suction side surface as well as spanwise profiles plotted inside the inter-pedestals ducts, for Reynolds number varied in between 10000 to 40000 and the Rotating number up to 0.23. In addition; the averaged Nusselt number is correlated as a function of Re, Ro, Pr and the dimensionless radial distance.

On the other hand, CFD analyses involving steady-state RANS by means of Ansys-Fluent solver using the $k\ \omega - SST$ turbulence model and the isothermal steady airflow in stationary and rotating conditions allowed to better understanding the developing internal flows, vortical structures and heat transfer prediction. Calculations were performed. A good agreement between CFD and experimental results is found.

The reported research work was supported by:

The Italian Ministry of Education, University and Research (MIUR) and the University of Florence.

General Introduction

Today the design advances of aero-engine or gas turbines in general are mainly driven by the requirement of a high power/thrust ratio at take-off or high specific work. To achieve this goal, manufacturers have generally increased the operating temperature, i. e. the turbine inlet temperature, which in turn has prompted them to use efficient cooling systems to keep the metal temperature below its critical values and thermal barrier coatings for blades parts characterized by high thermal loads. Among these latter, the trailing edge is one of the most critical parts of turbine blade, due to quite strict aerodynamic, thermal and structural requirements. Modern casting technologies allow manufacturing a blade with a very thin trailing edge profile for reducing weight and improving aerofoil efficiency. In addition, internal ducts area reduction and aspect ratio increase made the design of cooling systems more challenging due to mechanical strength and aerodynamics losses. The impingement of the radial multi-pass channels with ribs can not be accommodated in the blade trailing edge because of the thin part of profile, so the most widely used technique to enhance internal heat transfer consists in placing inserts of various shapes, named pedestals, in a slightly converging duct. Circulars pin fins arrays offer technical choices to enhance the overall heat transfer coefficient of the coolant in the blade trailing edge [1]. On the other hand, the enlarged pedestals have a lengthened shape of the base section, and as compared to circular pin fins, they increase structural strength and decrease pressure losses with a limited increase in the heat transfer.

Thesis objectives

According to the technical literature there is a great deal of studies concerning the pedestal shapes and their configurations, and there are several experimentations performed to analyse the capabilities of different trailing edge (TE) cooling schemes and their related pressure drop. Unfortunately, rare the works focusing on the exit discharge part of the blade trailing edge.

The presented thesis work is concerned with an experimental study focusing on studying the aero-thermal performance of an innovative internal cooling system for a trailing edge, under stationary and rotating conditions. The investigated geometry consists of a 30:1 scaled model reproducing a typical wedge shaped discharge duct with one row of enlarged pedestals. The

airflow pattern inside the device simulates a highly loaded blade cooling scheme with a 90° turning flow angle from a radial direction at the hub inlet to a tangential direction at the outlet through a wedge discharge channel. In addition, two different tip configurations were tested; one is a closed section, and another which has (05) holes on the tip outlet discharging at an ambient pressure. To investigate the effect of rotation on the performance of trailing edge cooling system, a rotating test rig previously developed and manufactured at the DIEF (Department of Industrial Engineering, University of Florence), was used.

Further to this experimental work, a complementary numerical study using ANSYS-Fluent code was carried-out to predict the behavior of the flow structure and the heat transfer inside the studied cooling model.

The CFD analysis utilized the same operating conditions as in experimental procedure and its results serve to validate the numerical model. In fact, the working is in low temperatures because of experiments constraints which, in this case, do not reproduce the real operating conditions. For that reason, the complementary numerical study under scaled operating conditions is just a first step with the aim of simulating the real heat transfer phenomenon inside the cooling system, and in overall, all the consistent typical trends are reproduced in total.

Thesis outlines

The dissertation comprises three main parts in addition to an introductory part sketching the problem of turbine blades cooling and the use of TLC technique in heat transfer problems. Chapter 1 introduces a review of the main blade cooling techniques and a comprehensive review of their related research studies. In chapter 2, effects of rotation on the flow field beside the main forces affecting the flow under the rotation conditions are presented. Chapter 3 presents the used test-rig and its different components. In chapter 4, the thermo-chromic liquid crystals technique is introduced by giving a background of its application in the heat transfer studies, and a detailed explanation of its calibration. Chapter 5 introduces first used test rig to evaluate the heat transfer for stationary conditions using a Reynolds number varied between 10000 and 40000, of three configurations of surfaces: smooth surface, Ribs +60° and -60° surfaces, and tip outlet conditions. In chapter 6, the heat transfer measurements related to the rotating conditions (Ro=0.05, 0.10 and 0.15) are presented. All the obtained figures, for the stationary and rotating conditions, are especially post processed using home developed Matlab procedures to obtain 2D maps of local heat transfer coefficient distribution over the heated surfaces. Matlab procedures allowed to

evaluate the local averaged Nusselt number over inter-pedestals vanes for the simple or complex correlations as functions of Reynolds number *Re*, Prandtl number Pr, rotation number *Ro* and a dimensionless distance *Xr*. Chapter 7 is devoted to the numerical simulations of the internal flows and the developing vortical structures and heat transfer inside the studied cooling schemes under the same imposed experimental conditions. To achieve this goal, CFD analyses involving the steady-state RANS Ansys-Fluent solver using $k-\omega-SST$ turbulence model beside the isothermal steady airflow for stationary and rotating conditions was conducted to reproduce the flow field. The validation is conducted by comparison of CFD flow field to PIV measurements for Re = 20000 at stationary and rotating conditions (Ro= 0.23). Later, the aero-thermal results are compared with experimental data obtained for Reynolds number = $\{20000, 30000\ and\ 40000\}$ and Rotation number from 0 to 0.15. Results are reported in terms of detailed 2D maps of HTC over the suction side as well as the averaged Nusselt number evaluated inside the pedestal ducts. Finally, the dissertation ends with the drawn general conclusions together with some suggested critical points for further improvements of this research work.

These obtained results will help to better visualize the complex structure of the flow and to assess the aero-thermal performance of a cooling system for new blade designs. Also, the obtained results are valid for both NGVs and stators configurations, because they focus only on the pedestals region of the trailing edge of the blade.

Chapter 1: Literature Review

Introduction

The first gas turbine was certainly set out by John Barber in the late 18th century. Since that time a number of other patents were lodged and experimental machines were constructed with varying degrees of success. Some of the problems encountered were due to an unavailability of the suitable materials and insufficient of turbomachinery components, the technology efficiency and the construction of compressors and turbines, in general.

It is clear that in the 19th century the concept of gas turbines became known and the efforts of all the pioneers are well documented. In the early part of the 20th century several trials took place. By the late of 1930s the concept of the gas turbine had been around for decades with articles already published and patents applied for up to 50 years ahead of the realisation of this goal.

Riall Sankey who, in his outstanding lecture on heat engines given to the Institution of Mechanical Engineers in November 1917 [1], predicted the future role of gas turbines. He could see a continued dominance and development of steam turbines for some time to come, which at that time had already reached 45 MW. He thought that "*…the steam turbines will hold the field for the large units ……. until a satisfactory gas turbine has evolved*," and also mentioned that during (1902-1917) *"a few experimental turbines have been produced but so far there has been no progress.*" There is no doubt that is the Brown Boveri with is 4 MW and an efficiency of 17.4% at 3000 rpm is the first practical industrial gas turbine which was established in year 1939, in Switzerland [2]. Frank Whittle in the United Kingdom and Hans von Ohain in Germany developed their researches independently, and from which their prototypes were developed. Since that, the gas turbine engine quickly became the standard choice for aircraft propulsion and even if the operating principles remained almost unchanged, but much, sometimes remarkable, developments and improvements have been made. For example, Fig. 1.1 illustrates a modern engine designed to power modern aircraft. The gas turbines are used to generate power and whenever necessary the waste heat can be recuperated by a steam generator for a steam turbine in a combined cycle.

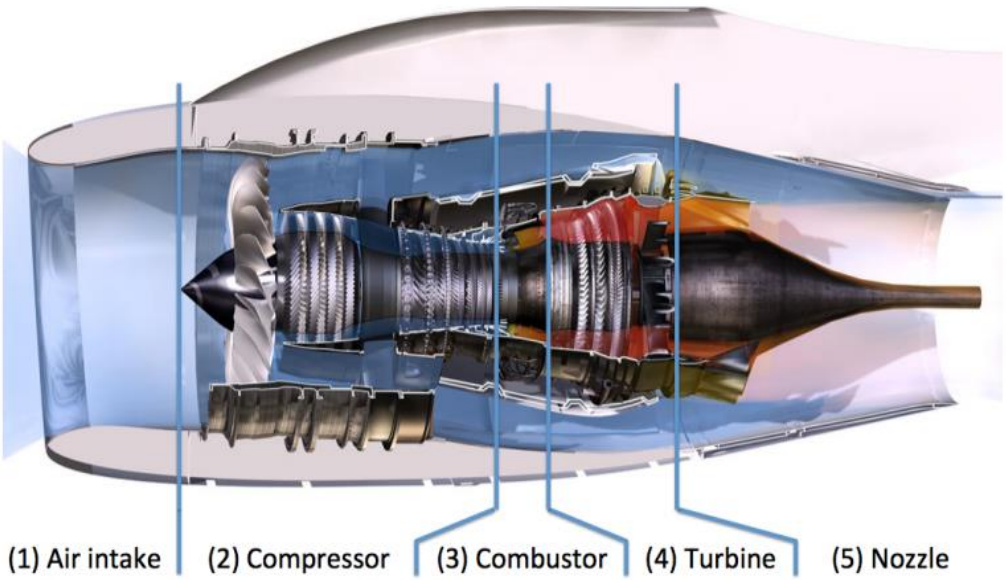

Figure 1. 1 : View of the different parts of an aeronautical engine.

Depending on the type of application or work needed to drive the aircraft: i.e. pure thrust for turbojets or turbofans and torque for turboprops or turbo-shafts, two architectures are possible, but composed of the same parts: The air intake (1) is designed to provide an air mass flow at proper conditions for the compressor (2) to increase air pressure. The compressor (several axial or centrifugal stages) is driven by the turbine via a shaft running through the engine. The high pressure air is then mixed with fuel in the combustor (3) and burns to increase the gas mixture temperature. Finally, the hot gases expand in the nozzle guide vane and a part of the flow energy is extracted by the turbine stages (4). In a turboshaft, most of the flow energy is converted into mechanical energy, whereas in a jet engine the hot gases are accelerated in a nozzle (5) to create thrust. The working principle of this engine relies on the Brayton thermodynamic cycle presented in Fig. 1.2b .

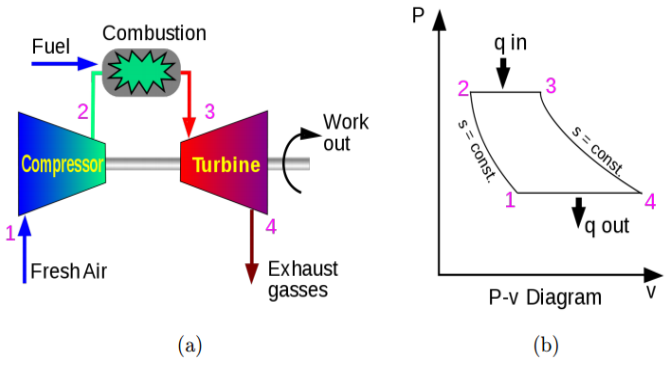

Figure 1. 2 : Gas turbine working principle: (a) simplified scheme (b) ideal Brayton cycle

The increase in power and efficiency can be obtained by increasing the compressor pressure ratio and the turbine inlet temperature. Focusing on the turbine, a rise in temperature however imposes new constraints on the design of this component since the blade material melting point is already surpassed in the existing modern gas turbines and, thus, the life duration can therefore be greatly reduced. Efficient cooling system is consequently needed to protect the blade and insure a longer life duration. In the following, a review is presented for the most used cooling systems.

1.1 Blade cooling systems

Nowadays, modern gas turbines are very powerful and reach higher efficiencies because of increased turbine inlet temperature (TIT) (Fig. 1.3), and the use of cooling systems allow reaching even higher TIT without affecting the blade material.

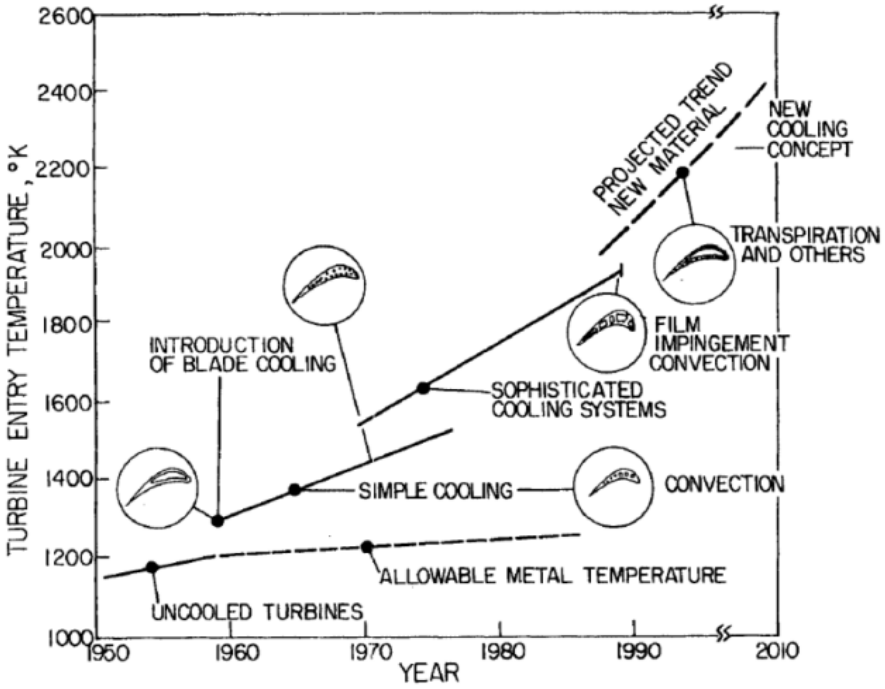

Figure 1. 3 : Improvement of turbine inlet temperature.

Advanced air cooling systems allow the NGVs and blades of gas turbines to operate safely below their material strength limit temperature. The casting technologies are manufacturing thin trailing edges (TE) as converging ducts in order to reduce the weight and insure a better aerofoil, aerodynamic quality and efficiency, subsequently this part of the blade is the most critical. The modern design of thin trailing edges arranges for shapes equipped with pedestals in order to increase the internal heat transfer (Han et al. [3]). Unfortunately, this thin trailing region is subject

to great aerodynamic, thermal and structural stresses, and this is why the local information on the heat transfer is critical in order to prevent, modify and optimize the coolant air and to reduce the internal surfaces. For example, Hart et al. [4] and Speziale et al. [5, 6] gave the main contributions to analyse the fundamental configuration of a radial channel of a rectangular cross-section in orthogonal rotation (i.e., with the rotation axis parallel to the channel height) with an outward flow. However, a key finding of the experimental study by Johnston et al. [7] was that a moderate spanwise rotation amplifies and damps turbulent stresses on the so-called unstable and stable channel side, respectively. The pressure field affects significantly the relative fluid flow and turns it out from the effect of the Coriolis forces that act on both the peripheral and radial directions in a plane perpendicular to the rotation axis. A first result, the secondary flows appeared (i.e., Coriolis vortices) which act mainly on the channel cross-section moving the flow from the channel leading side to the trailing side at mid height of the channel. On the other hand, the fluid layers close to the upper and lower walls are deflected towards the channel leading side, and the distribution of radial velocity component is affected by the pressure field. The velocity profile shape is distorted towards a flattened distribution with an increase in angular velocity, resulting into a Taylor-Proudman regime at the highest rotation rates, with a velocity maxima found close to the walls instead of being at the channel mid-height. In this regard, to quantify the rotational effects the rotation number Ro is introduced. In the open literature, a significant number of contributions in term of flows in rotating cooling channels can be sited. Conversely, with respect to trailing edge specific applications, only a limited number of experimental or numerical contributions are available, and the majority of works concerns ducts for nozzle blades. Later, Lezius and Johnston [8] examined the flow instability caused by rotation. A rotating in a high-aspect-ratio rectangular channel, and the working fluid was water. Stable and unstable regions were observed in the rotating flow. The unstable side showed a turbulence enhancement; whereas the stable side showed a suppression of turbulence.

The effect of accelerating the flow on the heat transfer and pressure losses in specific trailing edge geometries using pin fins and enlarged pedestals in a converging duct has been experimentally analysed by Metzger and Haley [9], Metzger and al. [10, 11]. An important experimental survey was given by Wang et al. [12, 13], in which they performed detailed measurements of the heat transfer on the endwall surface of pedestals array with TLC transient technique. With the same experimental method, Taslim et al. [14, 15] provided two experimental and numerical contributions focusing on studying the effects of jet impingement in a channel with an axial outflow. Hwang and Lui [16, 17], evaluated the heat transfer and the pressure losses

in trailing edge cooling geometries typical of real turbines blades: wedge and trapezoidal ducts, pin shape. They concluded that the effects of Coriolis and centrifugal forces on the fluid flow must be taken into account in the rotor blade cooling channels. Recentely, Facchini et al. [18] performed an experimental analysis about circular pin fins and enlarged pedestals in a converging duct. They showed the effects of an accelerating flow both on the heat transfer and pressure losses in some specific trailing edge cooling geometries.

Chang and Liu [19], and Rallabandi et al. [20] accomplished an experimental thermal analysis in the case of rotor blades channels. The thermal field investigation was accomplished inside a rotating cooling channel of trapezoidal cross-section with axial flow ejection at the TE through slots [19] or holes [20]. Researchers have given ready-to-use correlations applicable even to cooling models with complex geometries under rotation.

Concerning pin arrays performances, only few attempts could be found for investigating the effect of mixed axial-radial inflow conditions such as by Kulasekharan and Prasad [21] and variable cross section ducts by Bianchini et al. [22, 23]. It has been concluded that the mixed orientation (radial – axial) has an effect on the heat transfer. Later, Bonnani et al. [24] performed an experimental survey on the heat transfer of a trailing edge cooling system to study the effects of the rotation in internal cooling ducts based on the same 30:1 scaled model, by testing different configurations: smooth, +60 ribs and -60 ribs with closed tip and open tip, for a Re of 20000 and a Ro varied from 0 to 0.3. For a flat or a ribbed plate with closed tip and open tip, high peaks of HTC were shown in the stationary cases, located near the pedestal leading edge and along the pedestal surface facing the approaching flow. These peaks values were shown to decrease by increasing the Ro number for all configurations. As expected, the presence of ribs induced a global increase in HTC on the wedge section and the tests results show that the +60 rib of the open tip outlet condition reaches the most homogeneous heat transfer distribution all over the heated surface.

Also, Wu et al. [25] conducted an experimental investigation to obtain the heat transfer and the pressure drop data for an integral trailing edge cavity of a test section simulating a novel turbine blade's internal cooling passage with bleed holes. The local heat transfer was measured on both suction and pressure sides by the transient liquid crystal technique, while the pressures at six positions was recorded by pressure transducers, for a high values of Reynolds number, in between 20000 and 50000. Moreover, the flow characteristics and its effects on the heat transfer was analysed for conditions with or without bleed flow. The experimental results showed that,

in the case with a bleed flow, the local heat transfer on the pressure side exceeds that on the suction side in the first and second channels. In the cases without bleed flow, in the first and third channels, local heat transfer on the suction side weakens whilst it increases significantly on the pressure side. For the second channel, the non-bleed condition leads to a more balanced heat transfer distribution between the upstream and downstream channels. Besides that, after the bleed holes are blocked, the heat transfer in the first bend region on suction side declines sharply, while the opposite phenomenon occurs for the second bend region on pressure side. In both bleed and non-bleed cases, the total pressure of six measurement positions decreased continuously along the channel at the same Reynolds number and it increased for a higher Reynolds number. Among all the measurement points, under the same flow rate conditions, the highest speed occurred at position 5, which also produced the maximum difference between the total and static pressures. When the bleed holes are blocked, the total pressure at each measurement position appeared to increase.

Also, the turbulent flow inside a rotating channel provided with transverse ribs along one wall was studied by Coletti et al. [26] by means of 2D time-resolved particle image velocimetry. The measurement set-up was mounted on the same rotating disk with the test section, and allowed obtaining the same accuracy and resolution as in a non-rotating rig, for a Reynolds number of 15 000 and a rotation number of 0.38. As the ribbed wall was heated, both the Coriolis force and the centrifugal force played a role in the fluid dynamics. The mean velocity flow fields highlight the major impact of the rotational buoyancy (characterized by a buoyancy number Bo of 0.31) on the flow along the leading side of the duct. In particular, since the flow is directed radially outward, the near-wall layers experience significant centripetal buoyancy. The recirculation area behind the obstacles is enlarged to the point of spanning the whole inter-rib space. Also, the turbulent fluctuations are significantly altered, and overall augmented, with respect to the non-buoyant case, thus resulting in higher turbulence levels far from the rib. On the other hand the centrifugal force has a little or no impact on the flow along the trailing wall. The vortex identification, proper orthogonal decomposition, and two-point correlations are used to highlight the rotational effects. In particular to determine the effect of the dominant scales of the turbulent unsteady flow, the time-dependent behaviour of the shear layer and of the recirculation bubble behind the wall-mounted obstacles, the lifetime and the advection velocity of the coherent structures. [26]

Concerning the numerical studies, the new modern powerful computational tools allowed a better analysis and understanding of the performance of cooling channels characterized by various cross-section shapes (squared, rectangular, and triangular) and layouts (single pass, double pass) by means of simulations. In the open literature, Donahoo et al. [27], Hamilton et al. [28], and Ooi et al. [29], Loh`asz et al. [30], Luo et al. [31], Viswanathan and Tafti [32], and Spring et al. [33] studied the effect of spacing assessed on a constant section duct in terms of heat dissipation and required pumping power using a steady solver with RANS modelling and wall functions under stationary conditions. Saha and Acharya [34] performed an extensive unsteady analysis with the k-ε turbulence model, using a LES simulation for the validation purposes, on a square pin array. However, the effect of heat conduction inside the pin by means of a conjugate simulation of a bi-periodic pinned flat plate in a staggered configuration was studied by D'Agaro and Comini [35]. Later, Delibra et al. [36] studied the heat transfer and the flow field around a periodic array composed of 8 rows of eight circular pins. Results were partially successful in terms of heat transfer predictions, with both a wall resolved (4) equations eddy viscosity model and a LES computation.

Only few attempts however could be found when investigating the pin arrays performance considering the effect of variable cross section ducts by Di Carmine et al. [37]. The effect of rotation on the flow and the heat transfer at the blade trailing edge was studied computationally in the past for radial ducts by Prakash and Zerkle [38] and U-bended ducts by Iacovides et al. [39]. However, no significant literature was found for wedge shaped duct with mixed axial-radial flow under rotation. The same can be stated concerning the turbulence promoters like the enlarged pedestals: typical turbulators investigated under the effect of rotation are in fact mostly performed by Schuler et al. [40], Prakash and Zerkle [41], or the dimples of Tafti and Elyyan [42].

A complete experimental analysis of channel geometry similar to the one in Taslim et al. [14] was performed by Coletti et al. [43] and by Armellini et al. [44, 45]. Iacovides et al [46] dealt with Reynolds averaged Navier stokes (RANS) solutions for the flow and thermal field in a rotating serpentine passage. Elfert et al. [47] achieved PIV-measurement of secondary flow in a rotating two-pass cooling system with an improved sequencer technique. Saha and Acharya [48] performed unsteady RANS solutions in a rectangular smooth and ribbed channel to investigate the effects of the cross-section's aspect ratio the on the thermal performances. Large eddy simulations (LES) were used by Pallares and Davidson [49] in a rotating square channel,

and also by Felten and Laskowski [50] in a fully developed flow through a spanwise rotating infinite serpentine passage. And later Laskowski et al. [51] provided direct numerical solutions (DNSs) for the same geometry used in [50].

Lately, Andreini et al. [52] gave a numerical analysis of the heat transfer in a trailing edge cooling duct in stationary and rotating conditions for only Re= 20000 and Ro in the range of 0-0.23. They compared the results of the open source code "Open Foam" and the CFX code to the experimental data using a multi-blocks structured mesh composed of 6:2 10^6 hexahedral cells using the k−ω SST RANS model. They stated that the "Open Foam" code gives better results as compared with the CFX. Far ahead, Pascotto et al. [53] gave a numerical investigation using RANS approach and 8 10^6 hexahedral nodes model to study the aerodynamic flow field inside the same geometry studied in [45]. The numerical results were in good agreement to those obtained by PIV experimentation. The simulations were performed for Reynolds number equal to 20000, a rotation number of 0, 0.23, and 0.46, and channel orientations of γ of 0°, 22.5° and 45°, extending the previous results towards new engine-like working conditions. The numerical results were carefully validated against experimental data obtained by the same authors for conditions γ = 0° and Ro = 0, 0.23. The rotation is shown to alter significantly the flow field inside both inlet and trailing edge regions. These effects are attenuated by an increase of the channel orientation from 0° to 45°.

This literature survey shows that the inter-pedestals region of a turbine blade trailing edge is the most critical region and this why the present contribution is focussing on this part to give a better assessment for this innovative cooling scheme. Indeed, our present work is based on the same model and is a continuation of the previous research carried out by Bianchini et al. [22, 23] and Bonnani et al. [24], which take into account the axial redirection of the inlet radial flow and exit tip coolant flow rate. For this purpose, a larger range of *Re* from10000 to40000 and *Ro* up to 0.15 were adopted as being close to the real flows associated with the gas turbine blades operation. The results of the rotating state for a closed tip and an open tip configurations are analysed and compared with the stationary state, under the same Reynolds number. Moreover, different correlations of the averaged Nusselt number of the inter pedestals regions in the exit of the blade trailing edge are presented.

1.2 Trailing edge cooling

During the last decades, improvements of the cooling techniques have become very common in gas turbine industry. Engineers used firstly rough cooling devices by manufacturing blades with smooth and straight radial holes. Such simple cooling techniques required very high coolant flow rates, at higher TIT, which in fact decreased the machine performance. Therefore, a compound of different cooling devices are used today. The first stage needs a higher demand of coolant air, mainly the NGV working at the highest temperature of the thermodynamic cycle. The used cooling devices are different: about NGV stator the coolant flow development is represented in the blade to blade plane, while for the rotor blade there is a radial component too, Fig. 1.4.

Figure 1.4a presents two cooling configurations. For an NG, the coolant low through the blade is guaranteed by the use of an axial duct with constant diameter along the radii. The second form of cooling uses pin fins that are implanted in the wedge duct. An analogous technique is castoff for the rotor blade represented in Fig. 1.4(b) where turbulence promoters are inserted. Figure 1.5 illustrates another technique used in rotor blades where the thin fin trailing edge of the blade is protected by a coolant outflow on the suction side. In fact, the enlarged pedestals are of great interest to redirect the coolant flow.

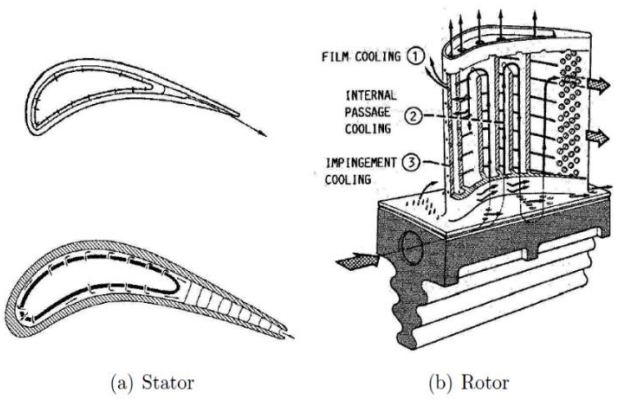

Figure 1. 4 : Cooled turbine blades.

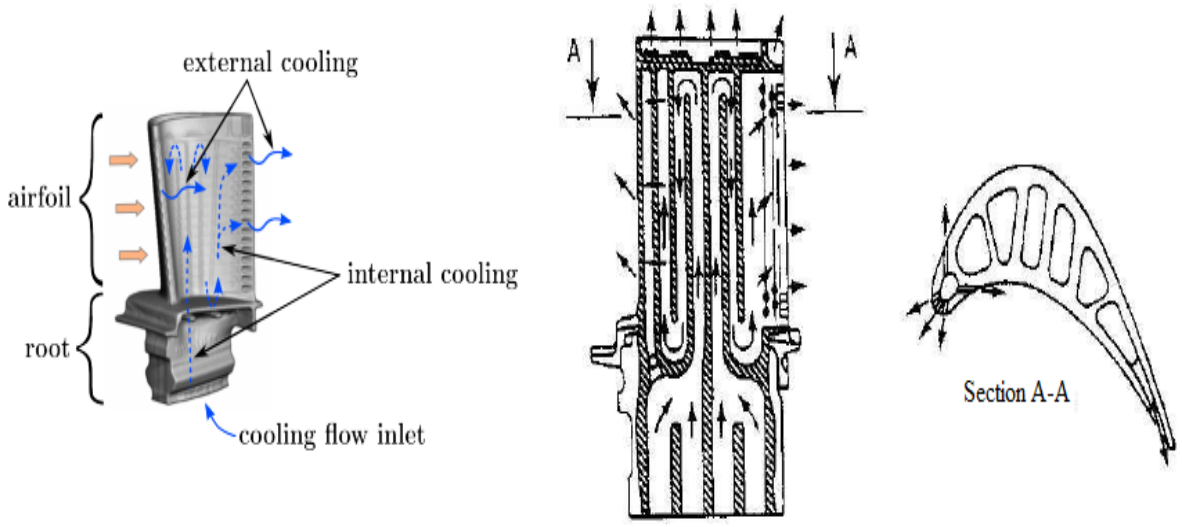

Figure 1. 5 : Rotor blades cooling.

1.3 Literature review of blade cooling techniques

The internal cooling systems represent all the technologies where the heat exchange takes place inside the thermally loaded component, in particular the NGVs and rotor blades of gas turbines. The review of literature provides many reliable results in order to compare and validate experimental and numerical results and data reported in this work. In this section a detailed review of the main cooling devices is reported.

1.3.1 Constant cross section ducts

The problem of constant cross section ducts can be processed as a forced convection problem. In the previous literature correlation treated the smooth circular ducts for fully developed flow, both laminar and turbulent. The Handbook of heat transfer offers about twelve heat transfer correlations for fully developed flow in smooth circular ducts. Also, the friction factor is correlated by ten correlations.

1.3.2 Converging ducts

Few publications treated the heat transfer in converging ducts with accelerated flow. Hwang et Liu [16, 17] used the transient technique to study experimentally the effect of the flow acceleration on the heat transfer. The measurements by thermo-chromic liquid crystal

thermography indicated an increase in the Nusselt number with the flow acceleration and similar results have been noticed for the friction factor.

1.3.3 Pedestals

Pedestals have been used recently as devices for the promotion of heat transfer. Often they are used to cool the trailing edge in heavy-duty gas turbines. Physically, one pedestal is an obstacle put in a unobstructed flow, this may show an external features. However, the use of two pedestals, the inter pedestal region may be considered as a duct where internal flow occurs. These geometries based on the pedestals illustrate both internal and external flows features and cause an increase in the turbulence and the wet surface, because they work as enlarged pin fins.

1.3.4 Pin fins

Pin fins are a prismatic support, generally with circular cross-sections, and they are one of the most common types of internal cooling devices used in turbine blades. They are placed orthogonally to the flow direction to maximize the forced convected fin cooling. Like cylinders in a cross-flow, pins shed wake at the downstream flow. The wake shed by each pin increases the free-stream turbulence, and the boundary layer development over the pin-mounted surface gets disturbed. The wakes from upstream pins also affect both the flow and heat transfer performance of downstream pins. In addition to flow disturbances, pins conduct thermal energy away from the heat-transfer surface, and long pins can increase the effective the wet heat transfer area.

One particular application of the pin fins is the cooling of the trailing edge of a turbine airfoil. In fact, the ribbed channels are not used on this part of the blade to avoid thickening of the downstream part of the airfoil. Thus, pin fins are introduced in a narrow channel from the root of the blade, as illustrated in Fig. 1.6.

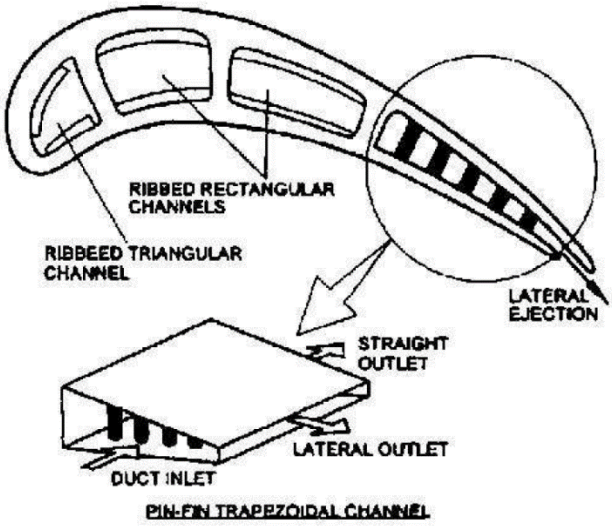

Figure 1. 6 : Schematic reproduction of a pin fins cooling section [21].

1.3.5 Dimple cooling

Dimpled cooling represents an alternative to rib and pin fins cooling due to the relatively low pressure loss penalty (compared with pins) and moderate heat transfer enhancement. A typical test section for dimple cooling studies is shown in Fig. 1.7. These concavities induce flow separation and reattachment with pairs of vortices. The areas of high heat transfer include the areas of flow reattachment on the flat surface immediately downstream of the dimple. The heat transfer in the dimpled channel is typically 2 - 2.5 times greater than the heat transfer in a smooth channel with a pressure loss penalty of 2 to 4 times that of a smooth channel [10]. These values show a little dependence on Reynolds number and channel aspect ratio. However, the dimple size, dimple depth, distribution, and shape each effect the heat transfer distribution in the channel.

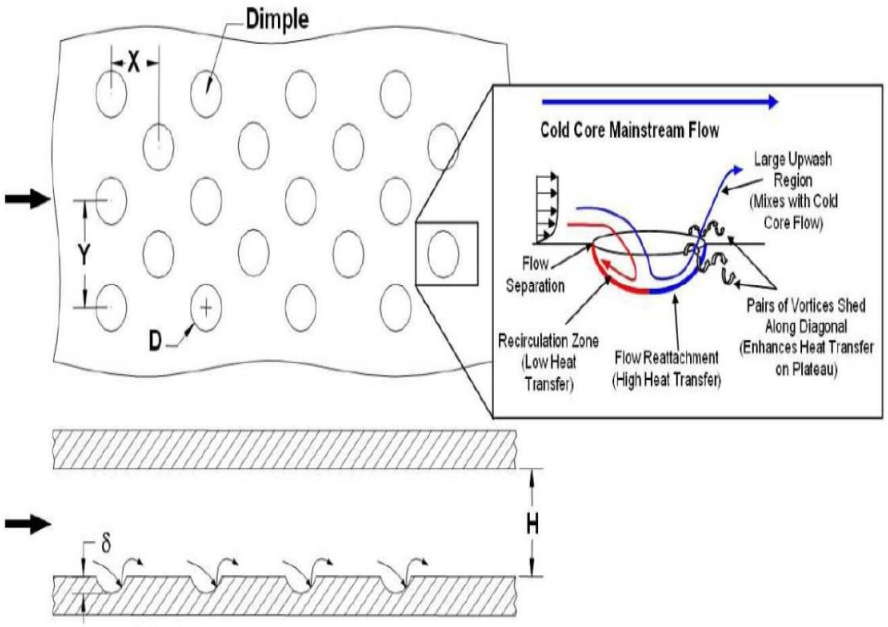

Figure 1. 7 : A typical test model for dimple cooling studies with a conceptual view of dimple induced secondary flow.

1.3.6 Double wall cooling

To enhance heat transfer from the surface of turbine blades, the double wall cooling technique uses a thin gap between two walls. The area exposed for heat transfer enhancement between cooling fluid and the metal is increased. The presence of a thin gap allows applying multiple cooling techniques within the gap, such as network of orifices is connected by small passages to create impingement areas (discussed in the next section) and an outward film cooling. Fig. 1.8 shows an example of a patented cooled blade with double wall channels.

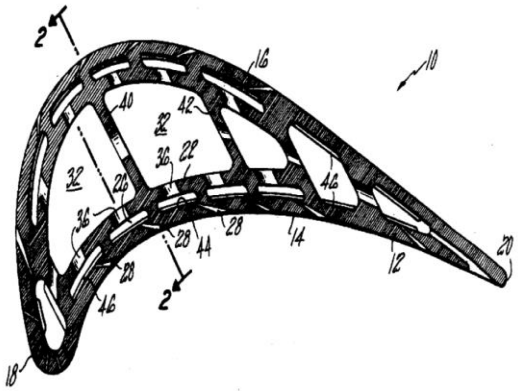

Figure 1. 8 : A sectional view of a turbine blade with double wall cooling [7]

1.3.7 Impingement cooling

All the described internal cooling techniques are characterized by a limited heat transfer augmentation. For a long channel as in multi-pass systems, the coolant flow temperature increases along the channel leading to a reduction of the heat removed from the walls. Another internal cooling technique that guarantees a considerable heat transfer enhancement is represented by the impingement cooling ejected from a hole or slot and directed to the heat transfer target surface. Since the cooling performance of impingement jets is very high, this method provides an efficient means of a component heat load management where sufficient pressure head and geometrical characteristics are available for implementation. Regular arrays of impingement jets are commonly used on the leading edge and mid-span regions of gas turbine blades and vanes to provide relatively uniform and controlled cooling of fairly open internal surface regions. Jets are generally arranged in arrays, including in-line, staggered or arbitrary patterns.

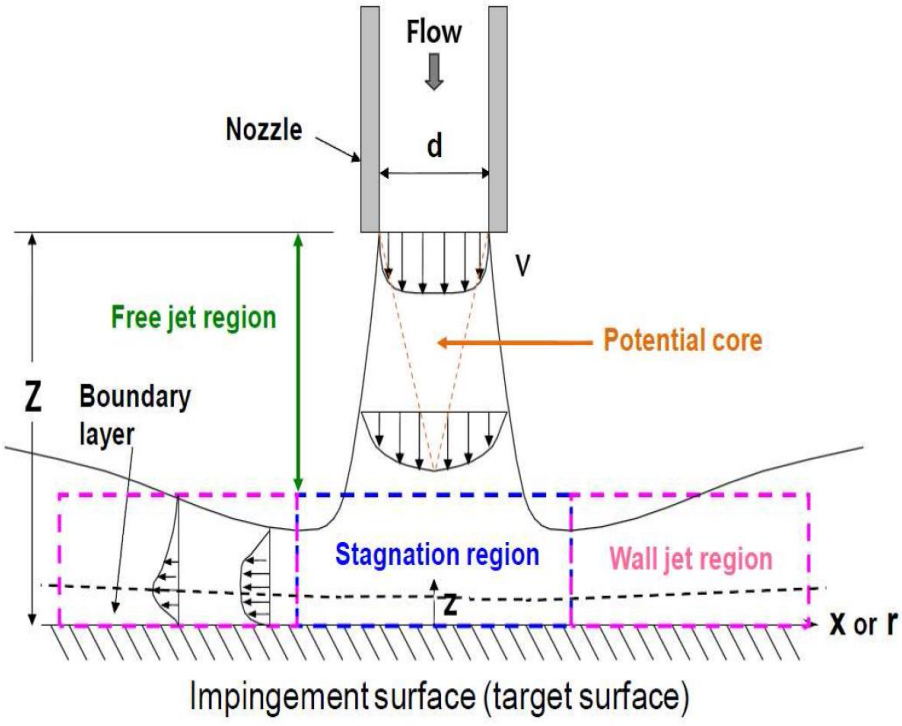

Figure 1. 9 : Schematic diagram of flow regions in an impingement jet.

Fig. 1.9 shows a typical surface impingement caused by a jet. The flow field of an impinging jet from a single round nozzle can be divided into three characteristic regions: the free jet region, stagnation flow and the wall jet regions. In the free jet region, the jet first begins to

broaden due to intensive shear interaction with the surroundings, which produces entrainment of mass, momentum, and energy. This region is called the flow development region. Simultaneously, as the shear layers around the jet grow, the potential core, i. e. The region where the velocity is still equal to the bulk velocity, starts diminishing in width. The core is typically visible up to 6 - 7 jet diameters from the nozzle. Once the free jet is fully developed (absence of core region), its axial velocity can be approximated by a Gaussian distribution.

Flow conditions of impinging flows are typically characterized by the jet Reynolds number, which is generally based on the nozzle or orifice diameter. Depending on the jet Reynolds number, four different jet characteristics can be found:

- Dissipated laminar jet: $\mathrm{Re_j} < 3 \times 10^2$,
- Fully laminar jet: $3 \times 10^2 < Re_\mathrm{j} < 10^3$,
- Transitional or semi-turbulent jet: $1 \times 10^3 < Re_\mathrm{j} < 3 \times 10^3$,
- Fully turbulent jet: $3 \times 10^3 < \mathrm{Re_j}$,

Generally, in internal gas turbine cooling applications, only fully turbulent jets are considered. Near the stagnation point there is the stagnation region that is strongly affected by the presence of the wall. As the jet approaches the wall, the axial velocity component is decreased and transformed into an accelerated horizontal component. The boundary layer around the stagnation point is laminar because of the favourable pressure gradient; the increase of the flow velocity along the wall keeps the boundary layer thin, and consequently, the heat transfer rates are high.

Conclusion

In the present chapter a literature review of the main experimental and numerical works dealing with cooling systems available in the open literature is presented with a presentation of the most used techniques to cool the trailing edge part of a blade. In the next chapter, the effect of the rotation on the cooling will be treated.

Chapter 2: Effect of Rotation

Introduction

The available literature classifies the cooling systems into two categories: internal and external systems. Generally, heat transfer features are enhanced using geometrical components (ribs, pi fins and impingement holes) located within a gas turbine blade in the flow pathway of internal channels. For a stationary component, the study does not care about the effect of rotation, which has to be taken into account for a rotating blade because the rotational effect significantly affects the heat transfer distribution. This is related to the Coriolis and rotational buoyancy forces which alter the flow field and as proved from several experimental studies, a secondary flow is produced and the core flow is asymmetrically distributed in the channel.

2.1 Effect of rotation on flow field

From the literature survey, it has been shown that the Coriolis forces and the centrifugal Buoyancy forces affect the flow field and the heat transfer distribution in the rotating cooling channel by altering the flow structure as compared to the straight non-rotating passages. It is very important to determine the local heat transfer distributions in the rotor blade cooling passages under the typical engine cooling flows, coolant-to-blade temperature difference and rotating conditions. In addition, the effects of the coolant passage cross-section and its orientation on the rotating heat transfer are also important. [24]

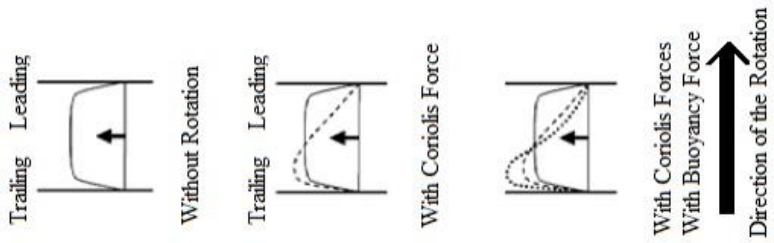

Figure 2. 1 : Conceptually view of effects of inertia, Coriolis and rotational Buoyancy forces on radially outward flow [67].

In fact, the stability of the turbulent boundary layer is affected by Coriolis forces that also alter the radial velocity and temperature distributions. While the distribution of the velocity profile is promoted by the buoyancy forces (Fig.2.1).

The flow in a rotating channel is significantly different from flow in a stationary channel. The secondary flow ducts rotation redistributes the flow velocity and also alters the random velocity fluctuation patterns in the turbulent flows. A rotating high aspect ratio rectangular channel has been used by Lezius and Johnston [8] to inspect the flow instabilities caused by the rotation for the case of water as a working fluid. From Fig. 2.2 stable and unstable regions were witnessed in the rotating flow. The unstable side shows turbulence enhancement; the stable side shows a suppression of turbulence.

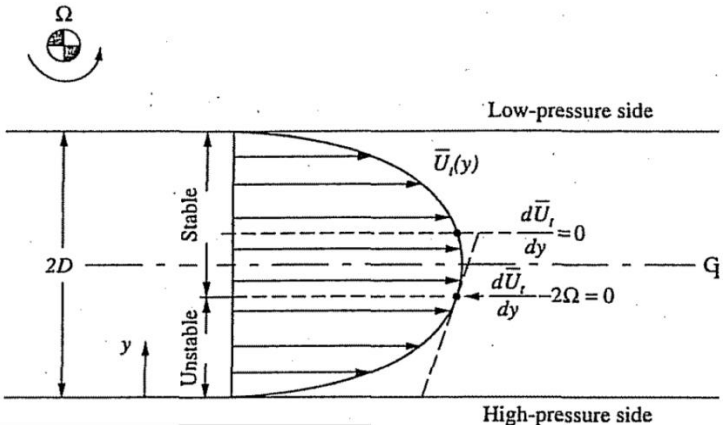

Figure 2. 2 : Lezius and Johnston (1976) [8].

2.1.1 Coriolis Force in internal cooling channels

In internal cooling applications, the position of the model is that the axis a rectangular cross section duct with the rotating axis must be in perpendicular position. The Coriolis forces are normal to the primary flow direction, and are balanced by a pressure gradient, which is generated by the bulk velocity $\left(\frac{\partial p}{2x} \cong 2\rho\Omega u_b\right)$ as illustrated by in Fig. 2.3: The high suction side wall is the trailing edge side (the destabilized side) and the low suction side is the leading side (the stabilized side).

The Coriolis force is proportional to the velocity value: approaching the walls the velocity decreases due to the no-slip condition and consequently the Coriolis force is reduced; on the other

hand the rotation-induced pressure gradient is constant in all of the section of the channel. This unbalance of forces creates a net force which causes the secondary flows in the cross sectional plane of the duct: the fluid is driven from the trailing to the leading side of the duct due to the principle of mass conservation a return flow is established in the interior of the duct, creating the two vortex pattern shown in the right image of Fig. 2.3.

The presence of secondary flows alters the distribution of the radial velocity and the temperature, and increase the friction and heat transfer at the walls with respect to the non-rotating case. This crossflow transports high-momentum fluid from the center of the duct to the trailing side and minimizing the increase at the leading side with respect to the non-rotating case. To take into account the effects of Coriolis force in internal cooling channel, the dimensionless parameters to monitor is the rotation number. The rotation number is defined as:

$$Ro = \frac{\Omega . D_h}{U_b} \propto \frac{Coriolis\ forces}{Inertial\ forces} \tag{2.1}$$

Where Ω is the angular velocity, D_h the hydraulic diameter at the inlet section and U_b the bulk velocity. As reported in Han et al. [3] and Saha and Acharya [48], the typical range of investigated *Ro* for internal cooling ducts is between 0.1 and 0.5. In these analyses, four different angular velocity values were investigated, i.e. 0, 9, 18 and 27 [rad/s], corresponding to the rotation number values of 0, 0.1, 0.2 and 0.3.

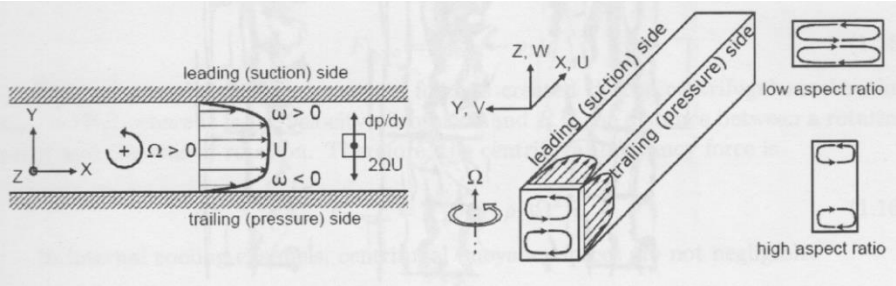

Figure 2. 3: Finite aspect ratio duct [67].

2.1.2 Centrifugal and Buoyancy forces in internal cooling channels

The buoyancy force is a result of acceleration field acting on a fluid that induces difference of density, as it is subscribed in equation 2.2:

$$F_{bu} = V(\rho_2 - \rho_1)a \quad (2.2)$$

With V is the fluid volume. In gravitational field, the gravitational gravity for example: Archimedes' force acting on a solid body immersed in a fluid. In a rotational field, the Buoyancy force is created by the centrifugal acceleration $a_{cen} = \Omega^2.R$, where Ω is the velocity of rotation and R the distance between the considered rotating point and the axis of rotation. Therefore, the centrifugal Buoyancy force is:

$$F_{cen_{bu}} = V(\rho_2 - \rho_1)\Omega^2 r \quad (2.3)$$

To analyze the Buoyancy effect, a non-dimensional parameter is used named Buoyancy number Bo defined as below, where Ro is the Rotation number, Tw the wall temperature, T_c the coolant temperature, r the distance from the axis of rotation and D_h the hydraulic diameter.

Prakash and Zerkle [37] produced a numerical prediction of the fully developed turbulent flow and heat transfer in a radially rotating smooth square duct with isothermal walls. They have shown that when $\Delta\rho/\rho$ = 0.01, the buoyancy force is negligible and only the Coriolis force is significant, but in contrary when $\Delta\rho/\rho$ = 0.13, both the buoyancy and Coriolis effects are significant and considered.

$$Bo = Ro\frac{T_w - T_c}{T_c}\frac{r}{D_h} \quad (2.4)$$

2.2 Objectives of the present work

The improvement of the turbine blade cooling effectiveness is of a great interest to achieve a high thermal cycle efficiency and this is achieved by developing new designs of rotating internal cooling channels and an in-depth knowledge of their complex flow structures. Furthermore, the experimentation is always the first step to well understand the physical phenomenon besides the validating numerical procedure. For that reason, this work is a continuity to the work carried out by L. Bonnani [24] from the University of Florence of an innovative trailing edge cooling device using enlarged pedestals technique, under static and rotating conditions, is undertaken both experimentally and numerically based on a CFD code. The obtained experimental data served in validating the numerical model for low temperatures and results may be extended to estimate the heat transfer exchanges in real operating conditions.

We will be focussing on the following points:

1. The heat transfer coefficient is investigated on the suction side of 30:1 scaled model of the new cooling scheme.
2. Three different surfaces are studied: smooth surface, +60° and -60° ribbed surfaces.
3. Extend the range of Reynolds number from 10000 to 40000.
4. The Effects of Coriolis forces are highlighted with both radial and axial coolant flows, for open and closed tip cases.
5. The Rotation number is in the range of 0-0.23.
6. Three different surfaces are studied: smooth surface, +60° and -60° ribbed surfaces.
7. A numerical investigation is carried out by using ANSYS-Fluent solver in order to predict the flow structure heat transfer phenomenon inside the cooling geometry under imposed working conditions.

Conclusion

In the present chapter, the effect of rotation on internal heat transfer is presented with an illustration of forces induced by rotation effect. The next chapter presents a review of the main rotating test rigs used in the open literature. After that, a detailed presentation is given of the test rig used in this study and its different components.

Chapter 3: The Rotating Test-Rig.

Introduction

The first part presents different types of rotating test rigs, depending on the orientation of the rotation axis which can be horizontal or vertical. The following sub-section illustrates examples of test rigs and the used optical measurements in the rotating conditions. Finally, syntheses with a conclusion on the final adopted approach in our present study are given.

3.1 Rotating test-rigs

Figure 3.1 shows a Multi-function rotating heat transfer test-rig used in investigating the flow and the heat transfer in the case of turbo disk, cavity, shaft and blade. The main parameters: a rotating diameter of 0.8 *m*, a test section of 1.6 *m* in length and the speed of rotation is 3000 *rpm*. Another test-rig is depicted in Fig. 3.2 used in testing the gas film impingement cooling in the rotating turbine blades, snake of shaped passage and a pillar-shaped passage heat transfer. Its main parameters are: a rotating radius of 0.5 *m* and a rotational speed of 2000 *rpm*. Another example of a horizontal rotation axis test-rig is presented by Fig. 3.3 depicting a schematic drawing of the rotating facility located at the Von Karman Institute [53]. The test section (of a wedge shaped duct) is located on a rotating disk of 2.5 *m* diameter of a horizontal axis of rotation. The rotation is entrained by an electric motor a velocity is controlled by an inverter and can reach 160 *rpm* at maximum, connected to the rotating apparatus by a transmission belt. In such rig, the Rotation number inside the channel varies from 0 to 0.33. The instrumentation tools such as the camera, the thermocouples and the pressure taps are located on-board the rotating disk and a data logger records all the data during the tests.

Figure 3. 1 : Multi-function rotating heat transfer test-rig.

Figure 3. 2 : Rotating blade internal heat transfer test-rig.

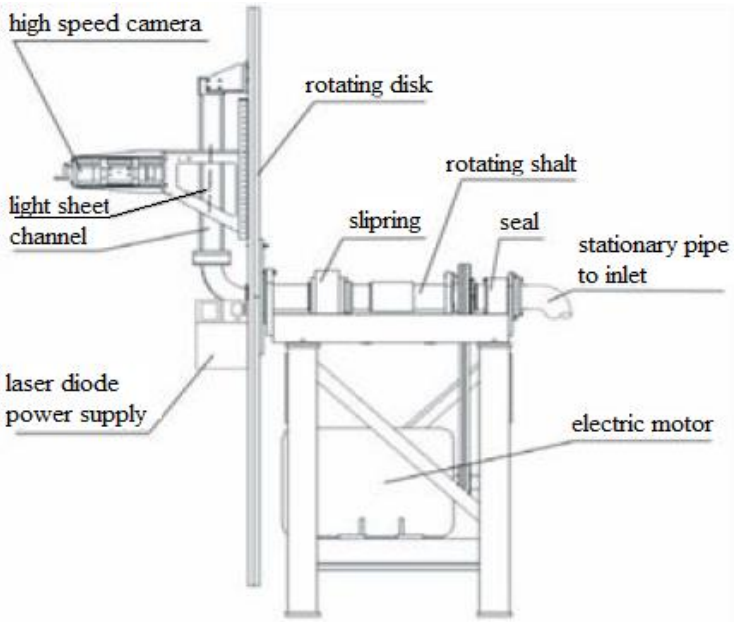

Figure 3. 3: Von Karmann Institute rotating test-rig. [53]

Figure 3.4 illustrates the rotating test rig of Texas A & M University [19] in which the axis of rotation is vertical. An electric motor controlled by an inverter is directly connected with the rig shaft giving a maximum rotational speed of 500 *rpm*. One hundred slip rings ensure the data transfer from the different pickups towards the PC acquisition unit.

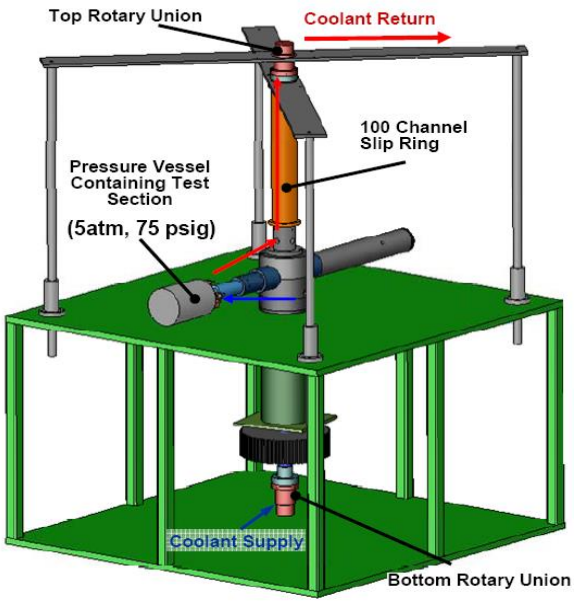

Figure 3. 4: Texas A & M University rotating test-rig. [19]

Synthesis:

The previous test-rigs are characterized by their small geometry and are used to reach a high rotation number Ro about 0.5 which is a reasonable value as reported by Han et al. [3]. The negative aspect of this type of test rig is that there is no way to have an over-view of the internal flow inside the tested geometry because of the used non transparent metallic disks. Furthermore, all studies on these test rigs use global information about pressure and temperature inside the tested geometry. Local information about the local distribution about heat transfer parameters are very limited.

3.2 Present rotating test rig

The test rig used in the Department of Industrial Engineering, University of Florence, is of a horizontal rotation axis with a less space to occupy. The rotation is ensured by an electric motor through a driving belt. The air passes through a manufactured rotary joint insuring the required structural strength. A finite element analyses was used to design the rotating frame and verify the structure that is subject to high centrifugal forces.

The used test rig for the present study is the one manufactured by L. Bonnani and al [24] within the research project PRIN 2007.This constitutes a long term research program funded by the Italian Ministry of Research and Universities, which is coordinated and shared with some Italian Universities such as Udine, Cagliari, Bergamo and Genova.

3.2.1 Rotary joint

The rotary joint was designed and manufactured by CelcoProfil s.r.l (Figures 3.5 and 3.6*)*. The schematic design of shaft and bearings and rotary joint are depicted in Figure 3.7 and 3.8, respectively. To ensure data acquisition a slip rings system is used to allow data transfer and on board instrumentation power supply. Twenty channels are available, two of which are made for high current loads, two other for low voltage power supply, eight for TC-IP protocol communication and remaining are silver made and compensated to connect thermocouples directly to the data switch-acquisition unit.

3.2.2 Electric motor

The rotation is obtained by *MAA132MA4* an asynchronous three-phase electric motor type: Marelli 6.5 kW, torque 50 Nm and a maximum speed of 1450 rpm (50 *hz*). The rotation speed is controlled by a frequency driver type *Lenze 8000* 7*:*5 *kW* 400 *V IP*21.The correct speed transmission between the motor shaft and the joint axis is assured by a toothed belt.

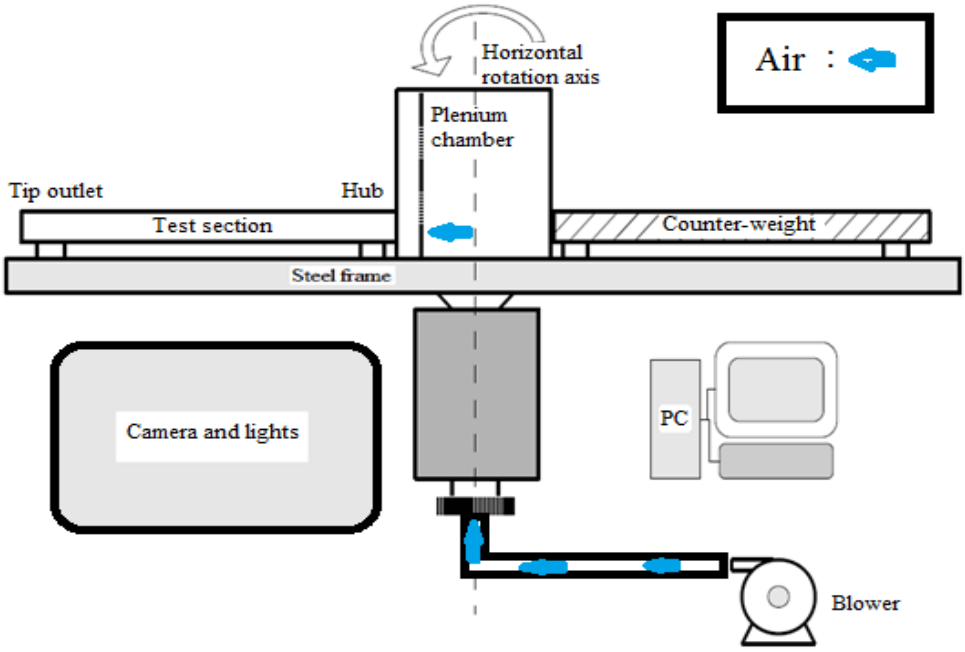

Figure 3. 5 : Layout of the test-rig.

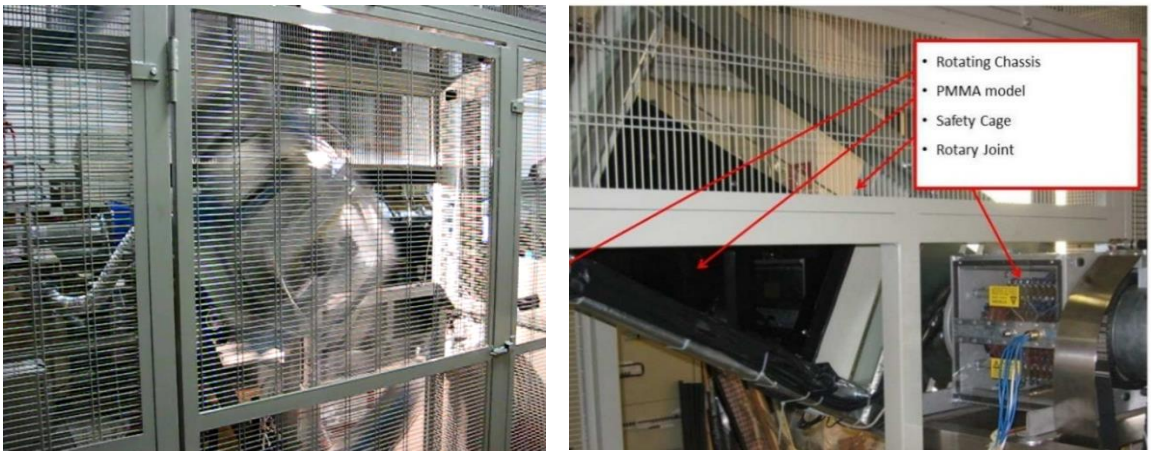

Figure 3. 6: The real rotary test-rig.

Figure 3. 7: Electric motor.

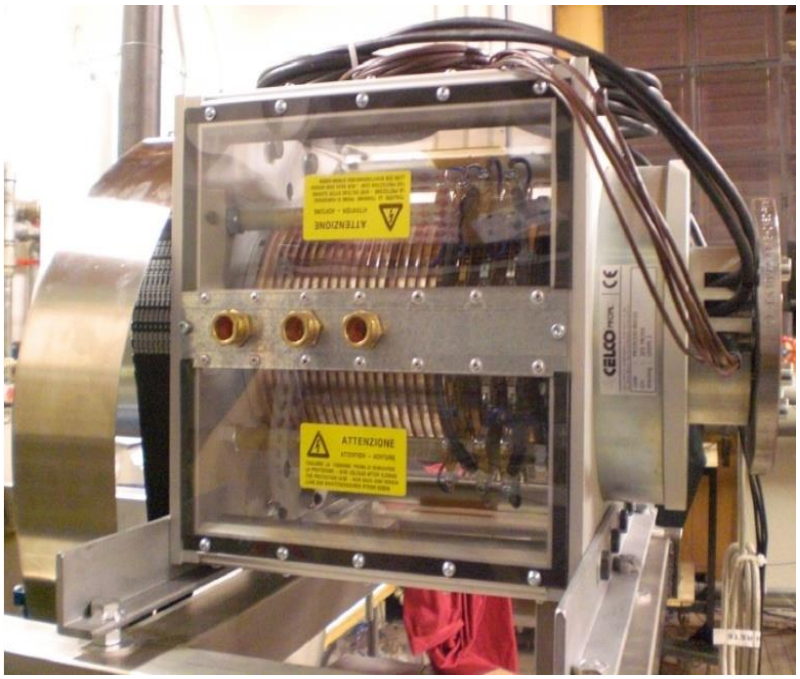

Figure 3. 8 : Rotary joint.

3.2.3 Blower

The required flow rate throughout the model is obtained via a high pressure centrifugal blower (figure 3.9) with a maximum flow rate of 400 m^3/h, and a pressure head of 40 cm H_2O.

Figure 3. 9 : Centrifugal blower.

3.2.4 Trigger circuit design

During the rotation of the test rig, it is necessary to synchronize the measurement chain, which means to take images when they are in the camera's visual field and in the same moment measurements data are documented. For that purpose, a home-made electronic device (Figure 3.10) drives the camera and the flashes at the moment of inquiring measurements data. The circuit is composed of a laser transducer connected directly to the camera and the flashes. The reflected laser signal from a specific device is fixed to the test rig. When the test section is in the camera's field view, it induces an input a square wave signal that produces a transition with an adjustable signal delay. It is necessary to have this adjustable delay to permit reaching the adjustable position within the camera's field view for the purpose of recording. At this position, the test model is brightened by the flashes which are activated simultaneously with the camera's recording, thanks to an activating signal, and by using a very short shutter time about $10^{-4}s$ [67].

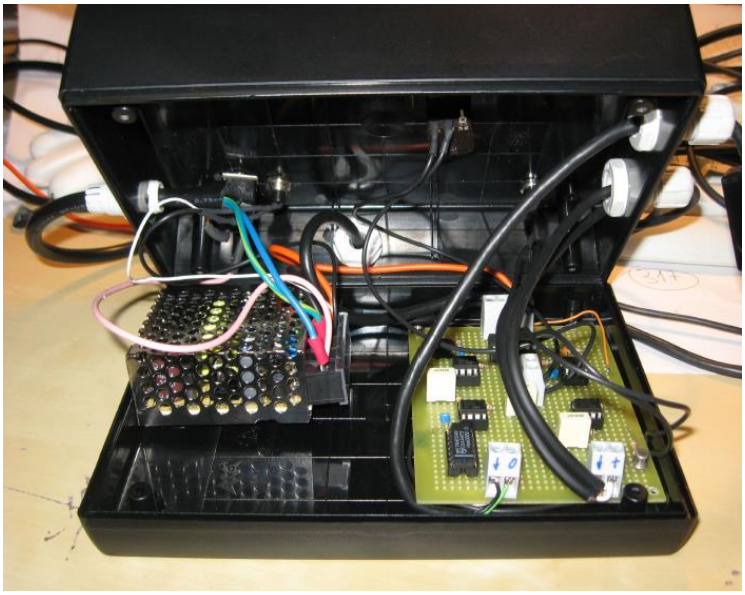

Figure 3. 10 : Trigger circuit.

3.2.5 Scaled model

The studied trailing edge gas turbine blade corresponds to a geometry which is normally have a tiny thickness (few millimeters), and receives the coolant flow of a pressure between 15 and 30 bar and a temperature from 1200 K to 1700 K. These effective operating conditions are hard to be reproduced in the laboratory test conditions. Therefore, by using some non-dimensional parameters such as Reynolds number, Rotational number, Prandtl number, Mach number and many others, the scaling of the model is one of the less prohibitive issues for a reliable scientific study. An appropriate scaled model is selected, which takes into account in the same time the non-dimensional parameters and the requirement for a structural strength. The selected scale for the trailing edge model is 30:1.

The operating conditions of real gas turbine engines are reproduced; Reynolds and Rotation numbers are defined as follows:

$$Re = \frac{\dot{m} D_{L0}}{A_{L0} \mu} \tag{3.1}$$

$$Ro = \frac{\Omega . D_h}{U_b} \propto \frac{Coriolis\ forces}{Inertial\ forces} \quad (3.2)$$

Where Ω is the angular velocity, D_h the hydraulic diameter at the inlet section and U_b is the bulk velocity. Typically the values of *Re* in real cooling ducts vary from 10000 up to 40000 and *Ro* from 0 up to 0:5, respectively. [67]

Conclusion

In this chapter, an overview of test rigs used in the literature to study the heat transfer phenomenon inside the blade cooling systems is presented followed by a description of the current used test rig and its components and characteristics. In the next chapter, the nonintrusive TLC technique used to estimate the HTC over the trailing edge of the blade, and its calibration procedure will be described.

Chapter 4: Experimental procedure

Introduction

This chapter describes the used experimental procedure to study the heat transfer at the trailing edge of a gas turbine blade corresponding to three configurations of innovative cooling schemes. The Heat transfer measurements are performed using the Thermo-chromic Liquid Cristal TLC technique which allowed measurements of a detailed heat transfer coefficient (HTC) maps and the averaged Nusselt number for open and closed tip cases.

4.1 The test-model

The investigated geometry reproduces the internal cooling channel of a turbine blade, the same described and analysed by Bianchini et al. [19], Bonnani et al. [24] and Armellini et al. [45]. The innovation of this geometry is that it insures at the same time an axial and a radial discharging when the tip is open. In the current cooling schemes, there is either an axial or a radial discharging. Also, there are few publications regarding TE redirection geometries in both static and rotating conditions. Also, there is the elimination of the pin-fins and the introduction of long pedestals (Ribs +60°) to reduce the pressure drop and introduce a better guidance effect on the external film cooling.

The discharge duct at the trailing edge region is a shaped wedge which includes a row of seven enlarged pedestals (Figure 4.2 a). The cooling air at the inlet section is radially oriented and then is turned by a channel of a 90° angle towards the trailing edge outlet section. The channel used to guide the flow from the radial inlet to the tangential outlet can be split in 2 parts: the L0 and the L1 region (Figure 4.2 b and Figure 4.2 c).

The *L0* region consists of a constant height channel and a lateral wall that reduces the passage area along the radial direction, used to redirect the coolant flow towards the trailing edge outlet. The inlet section, placed at the hub section, is rectangular with a hydraulic diameter (D_h) of 58.18 mm. The inlet section has a high aspect ratio (AR=7.25).

In the *L1* region is a converging wedge shaped duct with a converging angle α equal to 10° and an initial height (H_1) of 33 mm. Seven pedestals are placed inside the *L1* region and equally spaced with a radial-wise distance (P_z) of 75 mm. Each pedestal has the following dimensions: a length of 84 mm and an extreme diameter of 12 mm.

Measurements were performed at the *L*0 and L1 regions using a smooth and ribbed surfaces (Ribs +60° and ribs -60° of inclination). Two different kinds of tip were tested: an open tip with five holes discharging the fluid at an ambient pressure and a closed tip by replacing the five holes surface with a simple surface.

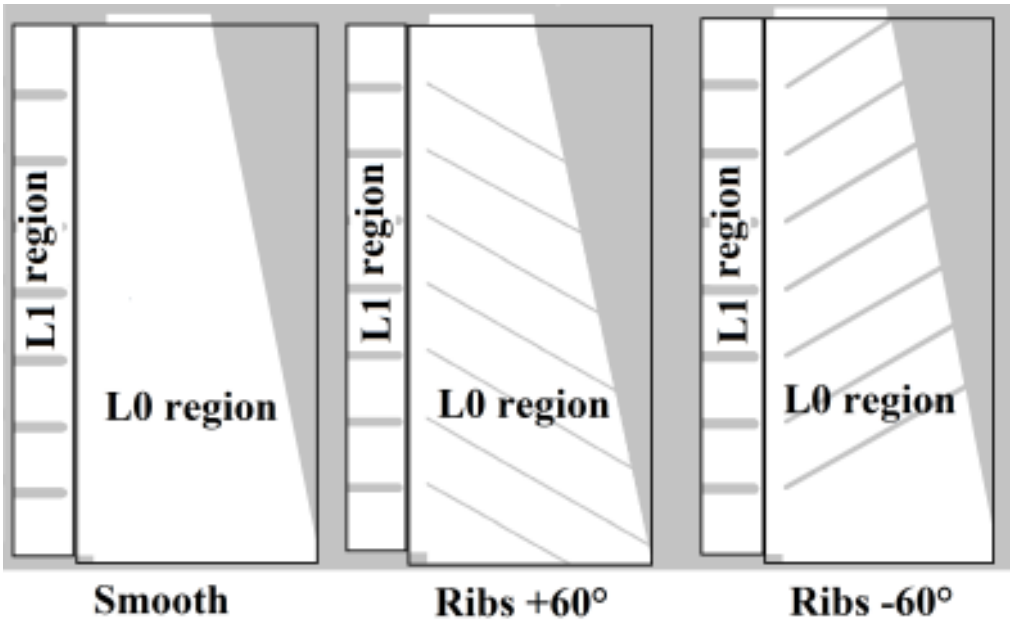

Figure 4. 1 : The three studied configurations.

The inlet section placed at the hub section is rectangular with a hydraulic diameter D_h of 58.18 mm, and a high aspect ratio *AR* = 6.25.

The channel is used to guide the flow from the radial inlet to the tangential outlet. For this purpose, it is split into two (2) regions: the L0 region consists of a constant height channel of a lateral wall of a reducing passage area (to impose a negative gradient) along the radial direction and used to redirect the flow towards the trailing edge outlet. The L1 region consists of a converging wedge shaped duct with an angle $\alpha = 10\ deg$ and an initial height H_1 = 33 mm. The seven pedestals are placed inside the L1 region and equally spaced with a radial distance P_x of 75 mm. Each pedestal has the following dimensions: a length of 84 mm and a thickness of d_z = 12 mm. Therefore, the matching exit angle of TE is equal to 90°.

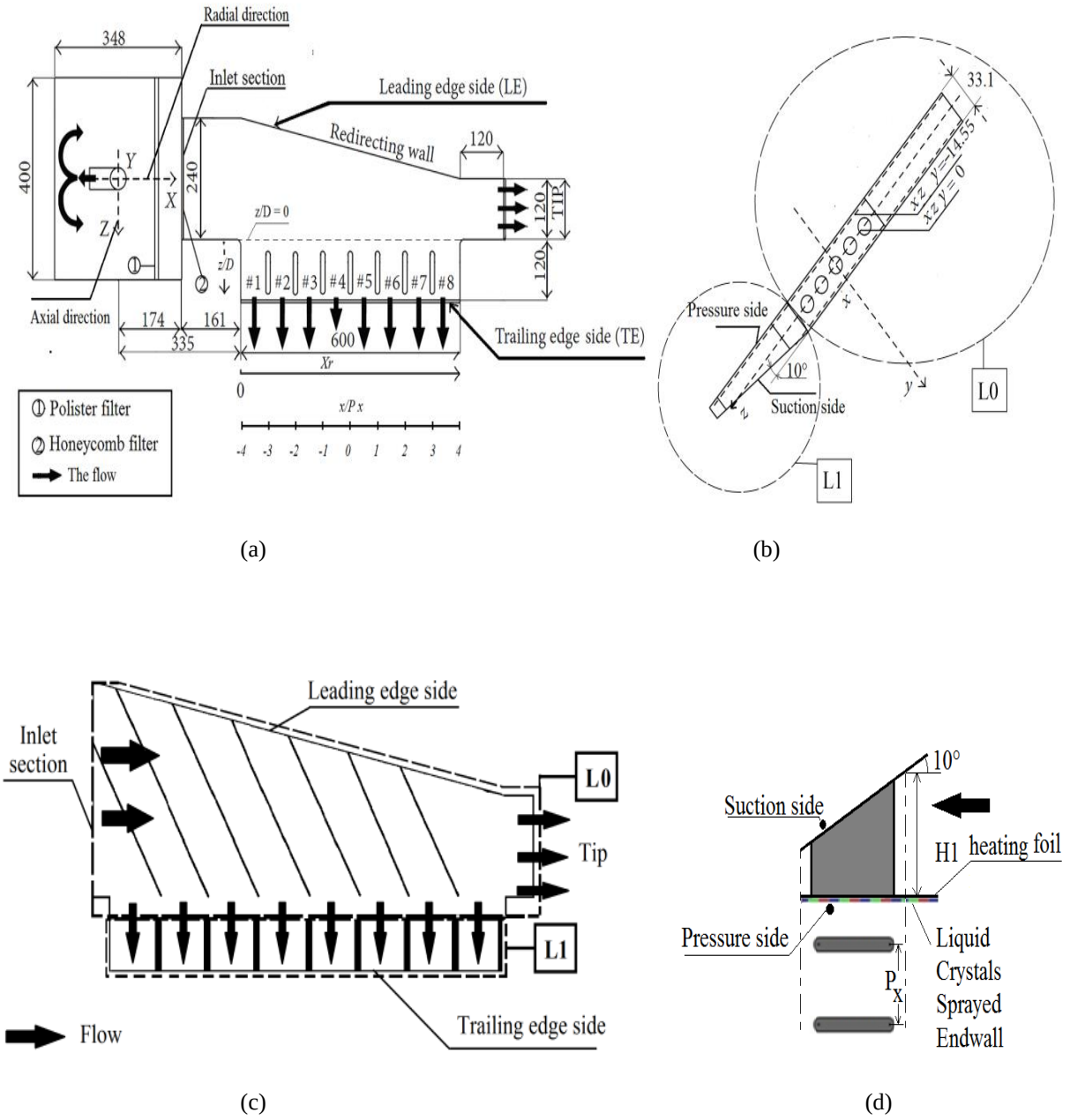

(a) (b)

(c) (d)

Figure 4. 2 : Schematic of the test section with positions of the measurement planes: (a) Top view of the setting chamber (b) Right view of the setting test rig (c) the subdivision of the studied area (d) details of the trailing edge part of the blade.

4.2 The test-rig

The test-rig as depicted in figure 4. 3 contains a rotary joint allowing air passage towards the test section. An inverter controlled electric motor located under the joint enables the rotation

by a transmission belt. A high pressure blower ensures the coolant toward a plenum chamber through a circular duct located at the centre of the chamber bottom wall. A 90° bend is used to turn the air flow towards the opposite wall of the test section via a polyester fiber filter to get the pressure drop necessary to have a uniform flow at the entry of the test section, which is later discharged at the ambient pressure from the trailing edge and the blade tip. The coolant mass flow rate is measured by a pressure transducer and a calibrated nozzle located upstream the blower. A scani-valve located on board of the rotary apparatus inside the plenum chamber and connected through temperature compensated piezo-resistive relative pressure sensors of a maximum accuracy of 5.9 Pa, is used to measure the pressure at 16 different locations. The acquired data of pressure is transmitted via a TCP-IP protocol through the rotary joint slips rings. Several T type thermocouples used to measure the air temperature are connected to a data acquisition/switch unit via compensated silver slips rings.

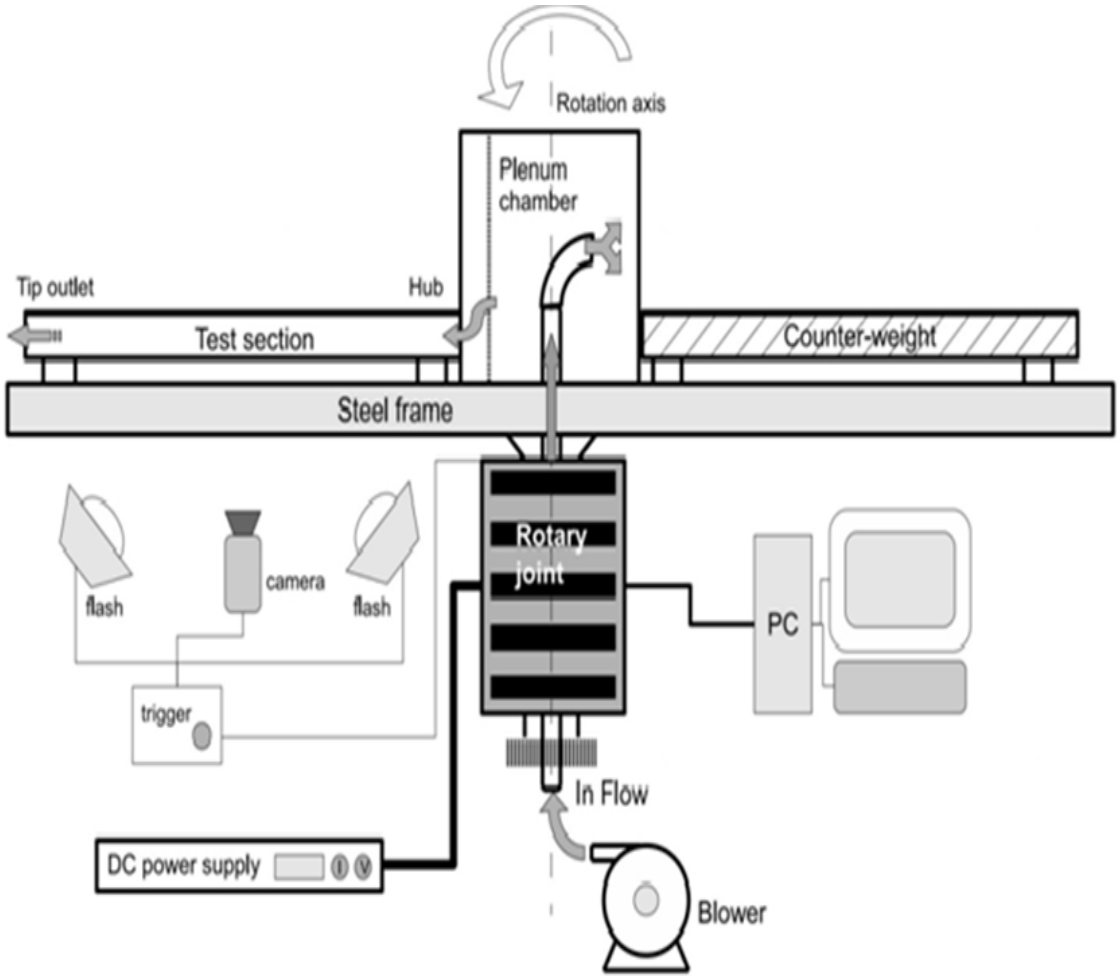

Figure 4. 3 : The test rig.

The measurement of the surface temperatures used a wide band Thermo-chromic Liquid Crystals (30C20W supplied by Hallcrest) steady state technique, active from 30°C to 50°C, calibrated in the same optical condition as a real test. The model was made of transparent medium (PMMA Plexiglas), and to ensure the optical access, the crystals were thinned down with water and sprayed with an airbrush. After preparing the scaled 30:1 model, the TLC is carefully painted on the heated foil. The heating element consists in a 25.4 µm thick Inconel Alloy 600 sheet, applied on the test plate with a double sided tape (Figure 4. 4 (1)). The working conditions are to be fixed by the user (Figure 4. 4 (2)). A digital camera served to record a colour bitmap image (1024x768 pixels) from the TLC painted surface on the PC (IEEE-1394 standard). The illuminating system consists in two studio flashes placed in a steady position at the rig (Figure 4. 4 (3)). In the rotating state, the camera and the flashes are fixed on a stand; hence it was necessary to synchronize the measurement chain as shown by Figure 4. 5. To record an image when the tested geometry crosses the visual field of the camera, a laser transducer triggers electronic device drives the camera and the flashes based on a trigger circuit. The input signal coming from the laser transducer is a square wave signal (green line Figure 4. 5) that produces a transition with an adjustable delay (blue line Figure 4. 5), necessary to ensure a correct position of the test section in the visual field of the camera in order to illuminate flashes. A digital camera was used to record the colour bitmap image (1296x964 pixels with a physical pixel size of 0.5 mm x 0.5 mm) from the TLC painted surface on a PC (IEEE-1394 standard) (Figure 4. 4 (4)). Data acquisitions (Figure 4. 4 (5)) of each single case are used as the entry conditions during the post processing step. A mask picture (Figure 4. 4 (6)) is used during the plotting of the 2D maps of HTC. Without a mask picture, the surfaces down the ribs and the pedestals are less cooled, and will appear black surfaces, and taken into account during the post-processing step which might lead to an error. The parameter hue (Figure 4. 4 (7)) is used to quantify the colour of the painted surface, and its calibration has been performed by replicating the same optical conditions as in real ones, in order to relate the colour of each pixel location to the local wall temperature Tw. The outputs of the post-processing step are the local temperature distribution over the studied geometry (Figure 4. 4 (8)), and by knowing the heat losses, the 2D maps of HTC values are plotted with a possibility to estimate the local Nusselt number and an average Nusselt number (Figure 4. 4 (9)).

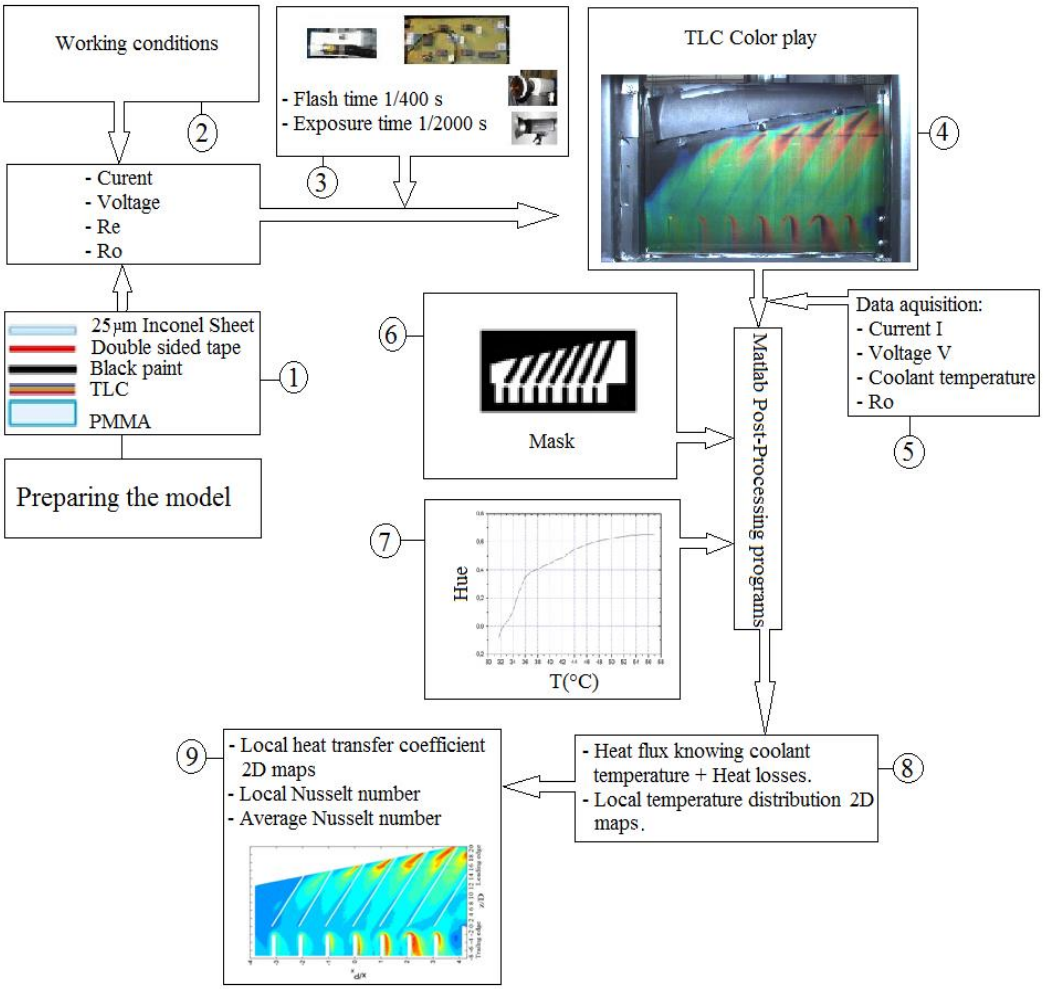

Figure 4. 4 : Experimental data acquisition

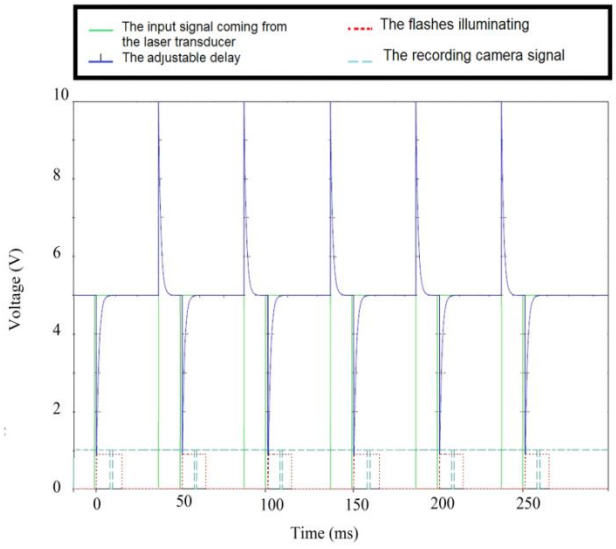

Figure 4. 5 : Signal chart.

4.3 Background of the Thermochromics Liquid Crystals technique

Thermo-chromic liquid crystal (TLC) thermography, as a powerful nonintrusive optical technique for temperature measurements, is capable of providing a high-accuracy continuous temperature field, especially for a complex structured heat transfer surface. The TLC materials are currently supplied by the Hallcrest Ltd. (Glenview, USA) and Merck Ltd. (Pool, UK) [55]. TLC thermography is a cholesteric liquid crystal material that forms a uniform structure. However, under different temperatures the orientations of adjacent liquid crystal molecule planes become different with certain angles, resulting in the reflection of different wavelengths of the visible spectrum of light. When illuminated with a white light this liquid crystal shows different colors, and such optical characteristics depend on its temperature and has a property of being repeatable and reversible. Currently, TLC can be provided with an operating temperature range between −30° C and 150° C, and the TLC may have a bandwidth (active temperature range) of 1° C to 20° C, in which the liquid crystal can be applied for temperature measurements by changing color smoothly from red to blue. The response time of TLC is about 3 10^{-3} s. The accurate relations between the TLC colors and the temperatures can be built through a careful calibration experiment, and subsequently can be used for a precise temperature distribution measurement of any type of surface. Pure TLC materials are organic compounds that can easily degrade when exposed to chemical contamination and ultraviolet (UV) light. Currently, it is possible to use micro-encapsulation process to reduce the degradation. The micro-sized TLC particles are microencapsulated within transparent polymer shells (PMMA), which can significantly improve the stability of liquid crystal materials and make them capable of being handled easily.

4.3.1 Liquid crystals in heat transfer applications

Pure un-encapsulated liquid crystals are known for their color brilliance; however, they suffer from rapid deterioration due to the ultraviolet radiation exposure and are sensitivity to moisture and dust. To overcome these drawbacks, liquid crystals are commonly micro-encapsulated in a protective 5–50 μm, clear, polymer spheres, suspended in a sprayable binder material. In surface thermography applications, the liquid crystals layer is typically deposited as a thin film on an underlying black substrate, as a thin coating beneath the TLC layer which is utilized to absorb the transmitted light. Based on the active temperature bandwidth, in which a

color response is observed, the liquid crystals are subdivided into the scaled narrow-band and wide-band TLCs (figure 4.6). The narrow-band TLCs have an activation interval typically equal to 1 K or less, which indicates a distinct event temperature. In contrast, the wide-band technique utilizes the entire color interval to map the surface temperature distribution on a single image. Favorable in the case of complex heat transfer problems, where a detailed temperature distribution of a high spatial resolution is desired, the wideband technique requires an accurate color-temperature calibration that has to be performed over the full color play interval with a significant number of points.

4.3.2 Calibration of thermo-sensitive liquid crystals

Before being used, the hue-temperature calibration must be conducted. In the past two decades, many studies have been conducted on the calibration methods of the TLC and indicated that the lighting angle and the coating thickness can significantly affect the TLC hue-temperature calibration curves [24].

The relationship between the colour and the temperature of the thermal liquid crystals (TLC) is usually found by a calibration experiment. In the present study, the calibration test was carried out by gradually heating an aluminum plate (calibration plate) of a 5 *mm* thickness which is covered with a liquid crystal film identical to that used in the experiments. The calibration plate was placed at the same position of the studied geometry inside the test rig and equipped with seven fine-gauge type-K thermocouples calibrated to ± 0.1 K (figure 4.7). The thermocouples are housed in small holes drilled in the material at different positions, close to the surface as possible, were used to measure the wall temperature and the degree of surface temperature distribution uniformity. The inlet and outlet passages of the test section were blocked during the calibration test in order to promote the isothermal conditions inside the test section. In fact, the sensor tri-stimulus value correction scheme represents a color calibration procedure by which the sampled TLC colors are ensured to distribute evenly around the white point (figure 4.6). They are corrected via a linear transformation which maps the detected $R^dG^dB^d$ space to the corrected $R^cG^cB^c$ space [55]. For a given wall temperature, the corresponding color image displayed by the liquid crystals is digitized and processed in order to obtain, pixel by pixel, the HSI (hue, saturation, intensity) contents from the RGB (red, green, blue) domain. Among the new parameters H, S, I only hue was retained since it was found to be the only one correlated

with the surface temperature. The temperature is determined by relating the hue to a temperature calibration function. The 8-bit representation of the hue value assures a resolution better than 1%. However, the color temperature relationship is illustrated on figure 4.8.

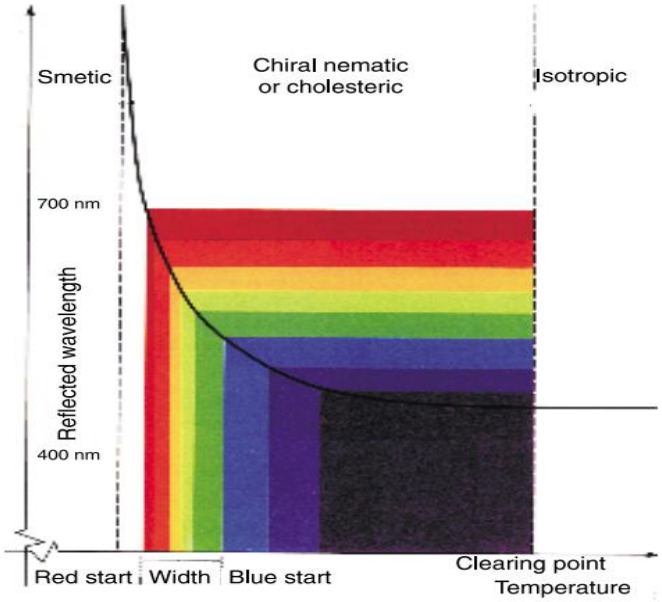

Figure 4. 6 : Typical reflected wavelength (color) temperature response of a TLC mixture. [67]

The most sensitive region is the color transition from red to green and takes place for a temperature variation less than one Celsius degree.

$$Hue = tan^{-1}\left[\sqrt{3}(G-B)/(2R-G-B)\right]/2\pi \quad (4.1)$$

$$S = \sqrt{2/_3}.\sqrt{R^2+G^2+B^2-RG-GB-RB} \quad (4.2)$$

$$I = \frac{R+G+B}{3} \quad (4.3)$$

Hence, the accuracy of the measured temperature depends on the color (hue) value, and varies from 3% to 10% of the full color play range. For the liquid crystals typically used results in an absolute accuracy of 0:15° *C* for low temperatures (red-green color range) and 0:5° *C* for higher temperatures (blue color range).

For further information, please refer to **appendix B**.

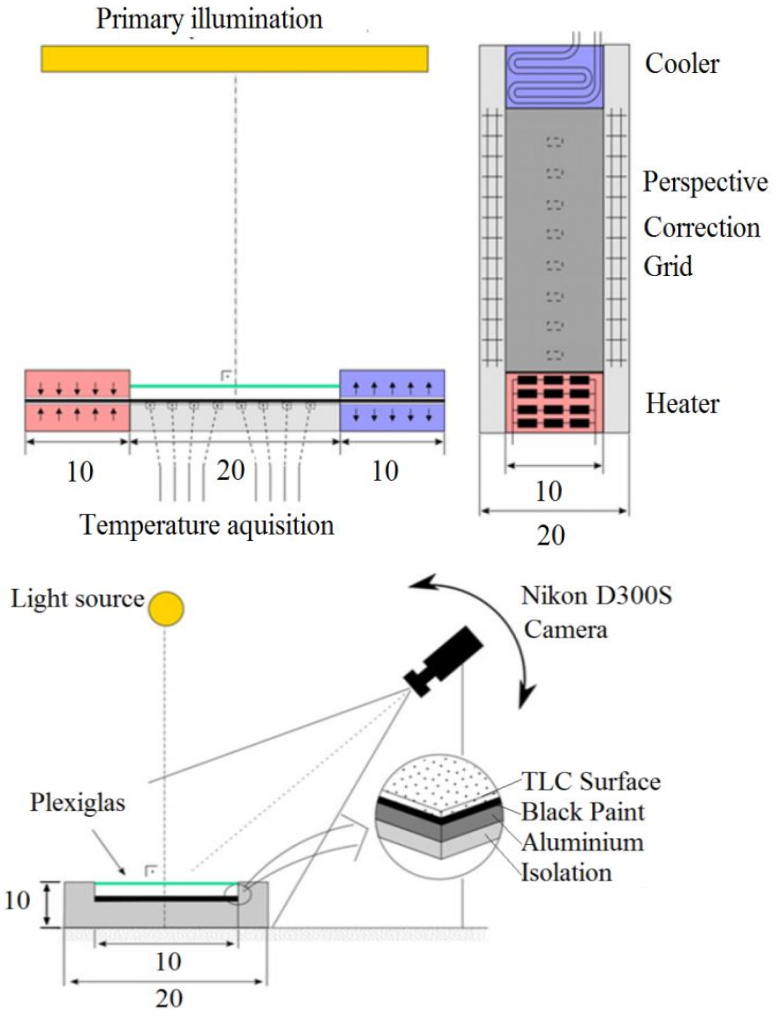

Figure 4. 7 : Schematic of the calibration facility procedure.

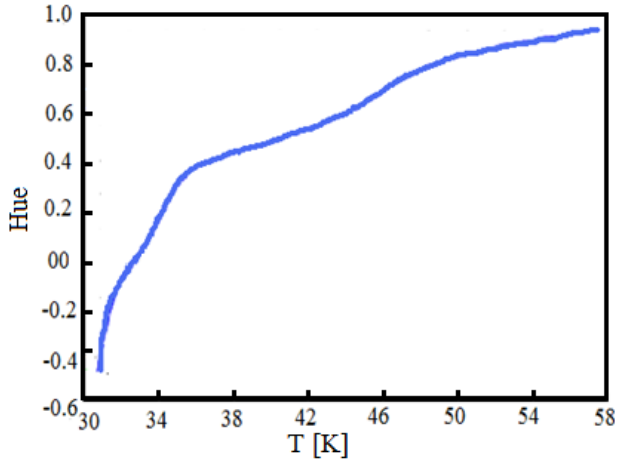

Figure 4. 8 : The hue vs temperature for TLC's calibration sample.

4.3.3 Steady state analyses: Constant flux method

For our purpose, the steady state analysis by considering a constant heat flux is a better way to measure the HTC on the studied surface. The steady state techniques are based on a heated model and the TLC is used to monitor the surface temperature. Usually, a surface electric heater is employed.

In this method, a test matrix is used to evaluate the heat transfer coefficient in the steady state condition. For that purpose, a heated model is employed as a steady state technique and the TLC is used to monitor the surface temperature. Usually, an electrical heater is applied on the surface such that a local flux $\dot{q}$ is imposed and by knowing the local wall temperature, T_w, as determined by TLC, the heat transfer coefficient *HTC* is deduced as follows:

$$\dot{q} = I^2 r \tag{4.4}$$

$$HTC = \frac{\dot{q}}{T_a - T_w} \tag{4.5}$$

T_a is the averaged ambient cooling flow temperature, I is current and r is the electrical resistance of the heater.

The local heat transfer distribution is evaluated by knowing the local convective heat flux and so taking into account the heat losses with the energy balance, and measuring the local surface temperature. This can be done using local thermocouples or optical methods such as Infrared-thermography or Thermo-chromic Liquid Crystals (TLC). Depending on the optical properties of the low conducting substrate, the surface temperature may be measured through the substrate or above.

Many studies have been done at the University of Florence using this technique (see for example Maiuolo et al. [56, 57, and 58]) and refer to Bonnani et al. [24] who included the effects of rotation.

The limits of this TLC technique are the difficulties to affix the heating element on complex geometries (e.g. multiple curvatures, diverging/converging), so that this technique is usually applied to flat plate or single curvature walls. For more complex configurations specific

heating devices might be applicable, but the local electrical field needs to be analyzed, for example, by the FEM approach, as reported in Maiuolo et al. [57] and Caciolli et al. [59].

4.4 Data reduction

The blade part subject of this study is a component of the first stage of a gas turbine. This component, which present dimension equal to a few centimetres, is continuously in contact with coolant flows of temperatures from 1200K up to 1700K and pressures vary from *15* to *45 bar*. Exactly reproducing the effective machine conditions, de facto, is impossible. High pressure, high temperature and small dimensions do not give a scientific unswerving. Therefore, the will to obtain less prohibitive conditions imposes a *scaling* of the problem, using the theory of similitude. Measurements obtained from scaled models can be reported to the real object through some non-dimensional parameters such as the Reynolds number, Mach number, Prandtl number,…etc. Therefore, a scaled model can be bigger than the component that reproduces, allowing detailed measurement. The scale is selected taking into account at the same time the non-dimensional parameter and requirement for structural strength. The Prandtl number depends only on the considered gas (dry air in our experiments) and not on temperature. This way, the studied heat transfer phenomenon is not influenced by the scaling of the real geometry, and results will reproduce those of real gas turbine applications. For which the Reynolds and Nusselt numbers are monitored.

During the heat transfer tests the surface is heated by a constant heat flux and exposed to a cooling air flow and a digital image of the investigated surface is acquired. For the data reduction Reynolds number is estimated at the inlet section of the L0 region similarly to Bianchini et al. [22, 23] and Bonnani et al. [24]:

$$Re = (\dot{m} D_h)/(A_h \mu) \tag{4.6}$$

Where $\dot{m}$ is the mass flow rate at the inlet section, μ the dynamic viscosity of the air evaluated at the film temperature at the inlet section of the L0 inlet region,D_h the hydraulic diameter and A_h the area of the inlet cross-section.

It has been decided to report the Reynolds number definition to the inlet section area instead of evaluating it at each slot, in order to avoid the use of intrusive instruments which may hide a part of the studied areas and by the way lead to losing local information concerning the HTC distribution.

The Heat transfer coefficient is calculated as:

$$HTC = \frac{\dot{q}}{T_w - T_{co}} \tag{4.7}$$

Where $\dot{q}$, T_w and T_{co} are the heat generated by the Inconel heating foil, the wall temperature and the coolant temperature at the inlet section, respectively. This HTC definition must be corrected by including the thermal losses due to conduction through the solid body as follows:

$$H = \frac{\dot{q} - \dot{q_{loss}}}{T_w - T_g} \tag{4.8}$$

By taking into account the thermal losses $\dot{q}$ and the heat generated by the Inconel heating foil, the wall temperature T_w and coolant temperature T_c, the local HTC is defined as follows:

$$HTC = \frac{\dot{q} - \dot{q_{loss}}}{T_w - T_{co}} \tag{4.9}$$

The heat losses $\dot{q}_{loss}$ are 4% in low temperature and 16% in high temperature areas, which are calculated on the heated side by knowing the thermal conductivity and the PMMA plate thickness, according to Bianchini et al. [22, 23] and Bonnani et al. [24]:

$$\dot{q}_{loss} = \frac{k}{s} . \frac{T_w - T_{ro}}{1 + k/(s.h_{conv})} \tag{4.10}$$

T_{ro} is the temperature air before going to the blower.

For the stationary case, the natural convection heat coefficient of the coolant h_{conv} is 5-25 W/m^{2}K [65, 66]. However, for rotation cases, h_{conv} is calculated knowing the average Nusselt number between the hub and tip sides, as follows:

$$\overline{Nu} = \frac{\overline{Nu}_{hub} + \overline{Nu}_{tip}}{2} \tag{4.11}$$

Based on the Reynolds number values, the adequate correlation used to estimate the average Nusselt number at the hub and the tip is given according to [65, 66]:

$$\overline{Nu} = \left(0.037\ Re^{0.8} - 871\right) Pr^{1/3} \text{ , for } \left\{ \begin{array}{c} 0.6 < Pr < 60 \\ 5.10^5 < Re \leq 10^8 \end{array} \right\}, \tag{4.12}$$

The Reynolds number is estimated at the hub side and the tip side, respectively, as follows:

$$Re = \frac{\rho_{co}.V.L}{\mu_{co}}, \quad (4.13)$$

With L is the flat plate length of the flat plate that has a width equal to 0.630 m.

The air density and the dynamic viscosity are estimated at the film temperature T_f(300-317 K).

The calculated Reynolds number values, at the hub and tip positions, are higher than the critical value (5.10^5) to get a turbulent flow.

The forced convection heat coefficient on the outside geometry:

$$h_{for} = \frac{Nu.k_a}{L} \quad (4.14)$$

The dimensionless parameter to take into account in order to reproduce the same rotational condition of real engines is the rotation number, defined as:

$$Ro = \frac{\Omega \cdot D_h}{U_b} \approx \frac{\text{Coriolis Forces}}{\text{Inertial Forces}} \quad (4.15)$$

Where Ω, D_h and U_b are the rotation speed in rd/s; the hydraulic diameter of the inlet section and the Bulk velocity at the inlet section, respectively.

The uncertainty analyses were performed according to the standard of ANSI/ASME PTC 19.1 [60], based on the Kline and Mc. Clintock method [61]. The different errors in measurements are for the temperature ±0.5 K, the differential pressure is ±6.9 Pa, the mass flow rate is ±2-3%, and the heat losses are from 4% to 16% in the high and low temperatures, respectively.

Table 4. 2 : Heat losses for different studied cases

	Low temperature zones					High temperature zones			
Re	10000	20000	30000	40000		10000	20000	30000	40000
$\dot{q}_{loss}$%	5.41	5.62	4.83	5.17		15.72	15.97	15.15	15.48

Conclusion:

In the present chapter, the experimental procedure approaching the working conditions solution using the scaling and dimensionless parameters was presented. In the following chapter, results related to stationary and rotation conditions will be illustrated.

Chapter 5: Results and discussions

Introduction

The investigated geometry is an internal cooling channel of a turbine blade the trailing edge, the same as described and analysed in [22, 23, 24].

The measurements of the heat transfer coefficient correspond to a Reynolds number from 10000 to 40000 defined with respect to the hub inlet section and the Rotation number Ro from 0 to 0.15. Six different configurations were tested corresponding to and three different surfaces: a flat plate and two others corresponding to ribbed surfaces at different angular orientation (Ribs +60° and Ribs −60° respect to the radial direction) for closed tip, and open tip with approximately 12:5% of the inlet flow discharged from the tip. The results are reported in terms of detailed 2D maps of heat transfer coefficient on the suction side as well as spanwise profiles inside the L1 region.

In the 2D HTC maps, the x/P_x is a fraction of the radial distance with the origin located on the mid- span of the L1 region, and z/D is a dimensionless distance with the origin located at the left plan of the inlet section. x, P_x, z and D are respectively, the radial distance, the inter-pedestals distance, the axial distance and the distance from pedestal's leading edge to inlet section (D=32 mm).

In order to facilitate the analysis of different phenomena related to the cooling, all the plots have the same colour range and the same scale for HTC.

5.1 Stationary conditions

5.1.1 Closed tip

Figures 5.1 and 5.2 exhibit that the values HTC are high at L0 region for higher Reynolds numbers, especially near the redirecting wall behind the ribs, but tend to decrease from hub to tip. Same figures show that all the cooling configurations have some peculiar features, where two regions of low HTC are noticed (continued black circle on figures 5.1 and 5.2): The first is located

in the inter pedestal vane near the hub (region #1) and the second is located near the tip along the redirecting wall. For each region, the low value of HTC is attributed to the recirculation zones. Figures 5.1 and 5.2 frame show that the size of these recirculation zones decreases by increasing the Reynolds number. In fact, the flow is fully developed after crossing the inlet section of the L0 region [22, 23, and 24] and due to the fact that the region #1 is directly positioned at a turning angle of 90° of the main flow stream, the average velocity in #1 is low. On the other hand, the size of the recirculation zone at the region #1 reduces the flow cross section; as a result, the heat transfer coefficient is low [24].

Concerning the L0 region, the shrinkage of its cross section along the axial x direction accelerates the flow, resulting in a rise of the heat transfer in this region. In addition to that, the strong turbulence disturbance induces an increase in HTC and helps to sustain an efficient cooling until the downstream parts of the passage, which is a good agreement with the results obtained by Wu et al [25].

The heat transfer distribution differs from the smooth to the ribbed surfaces due to the ribs effect. In fact, without ribs the flow is fully developed inside the L0 region and as much as the coolant flows inside this region, it interacts with the heated plate causing a decrease in the temperature gradient (coolant - heated wall) and subsequently, a decrease of the heat transfer along the radial direction of L0 region. The distribution of HTC is not uniform as seen for the smooth surface where the region near the hub is better cooled than the tip region. However, the existence of ribs disturbs the developed flow inside the L0 region, and increases the turbulence, and the heat transfer exchange as reported by Han et al. [3]. Small recirculation zones appearing just behind the ribs do not allow the main flow to reach the heated plate which causes low values of HTC seen behind the ribs (Figures 5.1b-c and 5.2 b-c).

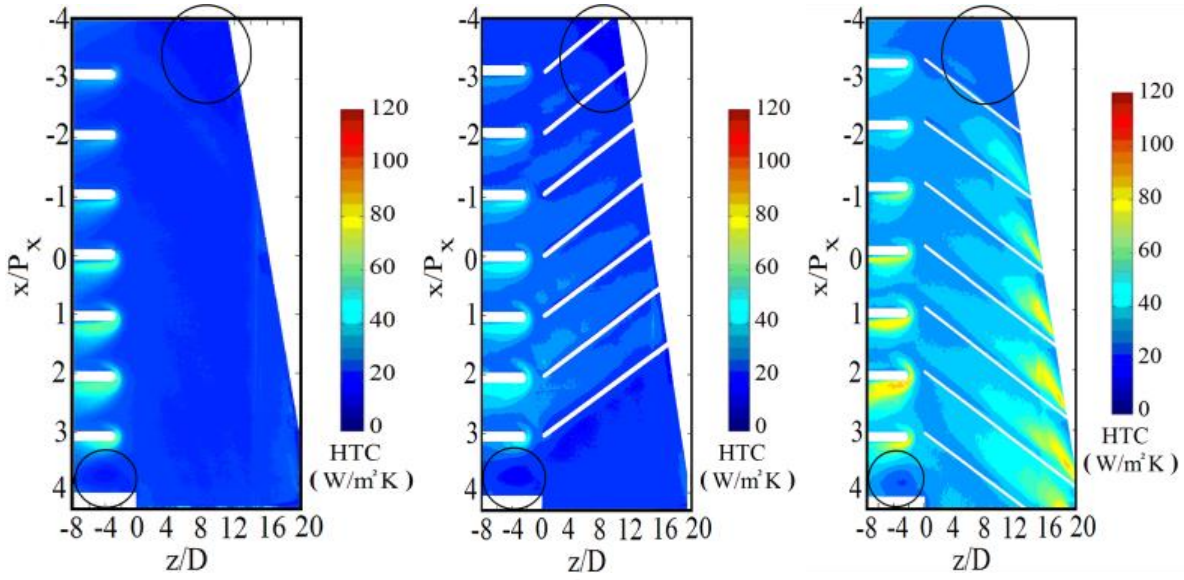

(a) (b) (c)

Figure 5. 1. 2D maps of HTC [W/m^{2}K], Closed tip configuration, Re= 10000,

(a) Smooth, (b) Ribs -60°, (c) Ribs +60°.

(b)

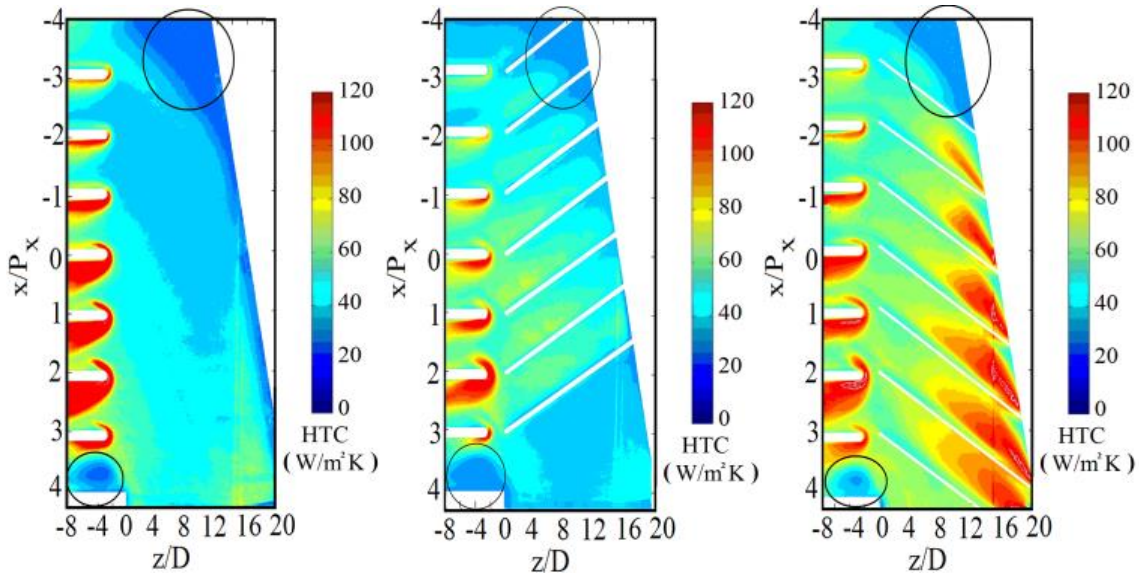

(a) (b) (c)

Figure 5. 2. 2D maps of HTC [W/m^{2}K], Closed tip configuration, Re= 40000,

a) Smooth, b) Ribs -60°, c) Ribs+60°.

The effect of ribs orientation is highlighted by figure 5.1b/c and figure 5.2 b/c. In fact, Ribs +60° and Ribs -60° do not have the same HTC distribution. In fact, when the coolant reaches the ribs near the redirecting wall, in case of configuration Ribs +60°, it first interacts with the ribs and the turbulence disturbance increases. Due to ribs orientation, the flow is oriented in the

direction of the redirecting wall, and such orientation of the redirecting wall boosts turbulence disturbance of the flow. In addition, to the reduction of the flow cross section, there is an augmentation of the heat exchange. As moving forwards the tip, the efficiency of the cooling becomes lower due to increase of bulk temperature between the main coolant flow and the heated plate, as seen from figure 5.3, which illustrates the reduction of coolant temperature potential as noticed by Wu et al. [25] and Gillespie et al. [61]. The coolant temperature potential is defined by Gillespie et al. [61] as follows:

$$\frac{(T_b - T_w)}{(T_{co} - T_w)} = \text{The efficiency of the coolent temperature potential} \quad (5.5)$$

Where T_b the bulk temperature, T_w the wall temperature and T_{co} the temperature of the coolant at the inlet section.

For the case of ribbed surface, ribs at -60° make the flow going into the direction of the L1 region instead of the redirecting wall region, which results in a lower boosting effect of the redirecting wall. The heat exchange efficiency is mainly influenced by the increase of the coolant flow velocity due to reducing the L0 flow cross section as compared to Ribs +60° surface. Moreover, for both -60° and +60° ribs orientations, the HTC values at the mid of pedestal regions (regions #3 to # 6) are lower compared to the flat plate case. This effect may be explained by the rib orientation towards the axial direction which reduces the angle of attack of the coolant facing the leading edge of the pedestal, and the enhancement of the global turbulence inside the L0 region which reduces the heat exchange efficiency.

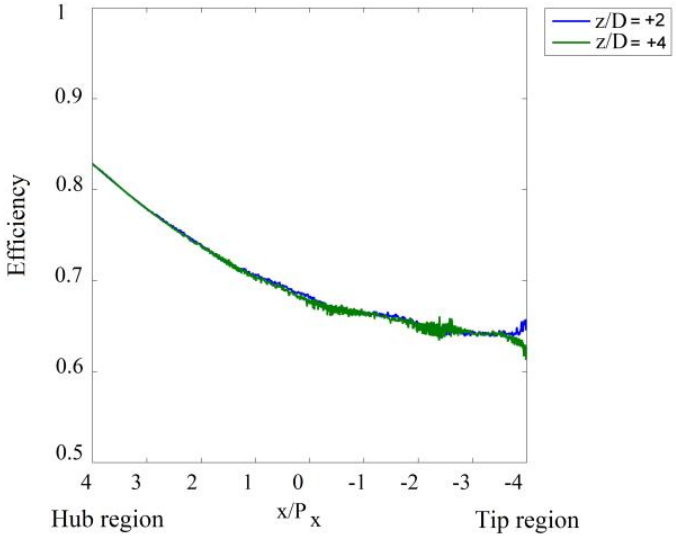

Figure 5. 3. The coolant temperature potential.

Concerning the L1 region, it is possible to notice that the high values of HTC are reached at the leading edge of each pedestal around the stagnation point due to turbulence enhancement, especially for the regions from #2 to #7. The coolant reaches the L1 region after being reoriented and accelerated by the redirecting wall. The contraction of the L1 region in the z direction decreases the cross flow section and the flow is accelerated. Figures 5.1 and 5.2 show high values of HTC around the leading edge of each pedestal and its downstream zone. In fact, Armellini et al. [45], Andreini et al. [52] and Andrei et al. [63] reported that, when the flow reaches the leading edge of the pedestal, the deviation of the approaching boundary layers over the heated plate and the pedestal surface induces the creation of a horse-shoe vortex. The horse-shoe enhances the heat exchanges between the main coolant flow and the heated plate. So, more fresh coolant reaches the heated side of the internal geometry. This observation is in good agreement finding by Wu et al. [25].

To support these explanations, figure 5.4 refers to the PIV data of Andreini et al. [52] and Andrei el al. [63] for *Re* = 20000 which shows the 3D flow structures in the mid of inter-pedestals at the region #4. As shown, the profiles of the mean velocity component V (nondimensionalised by the bulk flow velocity in the inlet channel, U_b) in the planes *y = 0, y = 14.55 mm, z = 150 mm and z = 165 mm*. On the suction side of the pedestal, the flow is dominated by the separation zone and no clear imprint of the horseshoe vortex is revealed at the *plane A xy1*. The flow streamlines exhibit a flow motion from the mid-span pedestal towards the end-walls. By moving towards the channel trailing edge, the averaged flow structure is further complicated by the flow acceleration imposed by the narrowing of the channel and the horse-shoe structures appear larger and there is an air replacement between the pressure and the suction sides of the pedestal (figure 5.4: *plane B xy2*). Similar flow features are observed in other trailing edge inter-pedestal regions, but the only difference, there is a reduction in the separated flow structures downstream of each pedestal when moving towards the blade tip. The outflow, at the inter-pedestal passage trailing edge is almost completely axial close to the blade hub for which a wide recirculation zone affects the discharge flow (figure 5.4*: planes C xz3 and D xz4*). The recirculation zones on the suction side of each pedestal decreases the passage area of the flow which accelerates the flow over the pressure, and results in a better cooling of this side. However, the heat exchange between the flow and the heated plate is lower at the suction side of the pedestal due to the recirculation zone. The intensity of heat exchange is shown to decrease along the L1 region as going from the region #2 toward the region #8. In fact, as explained before, the cooling capacity is decreasing as much

as the flow moves toward the tip region along the L0 region, because of the interaction with the heated plate and turbulence disturbances in the L0 region. For that reason, the region #2 is crossed by a flow having a lower temperature than the region #8 where the flow is warmer. The recirculation zone at the tip region interacts with the coolant as redirected towards the region # 8 by rising its temperature. As the coolant film temperature is higher, the heat exchange decreases at this region.

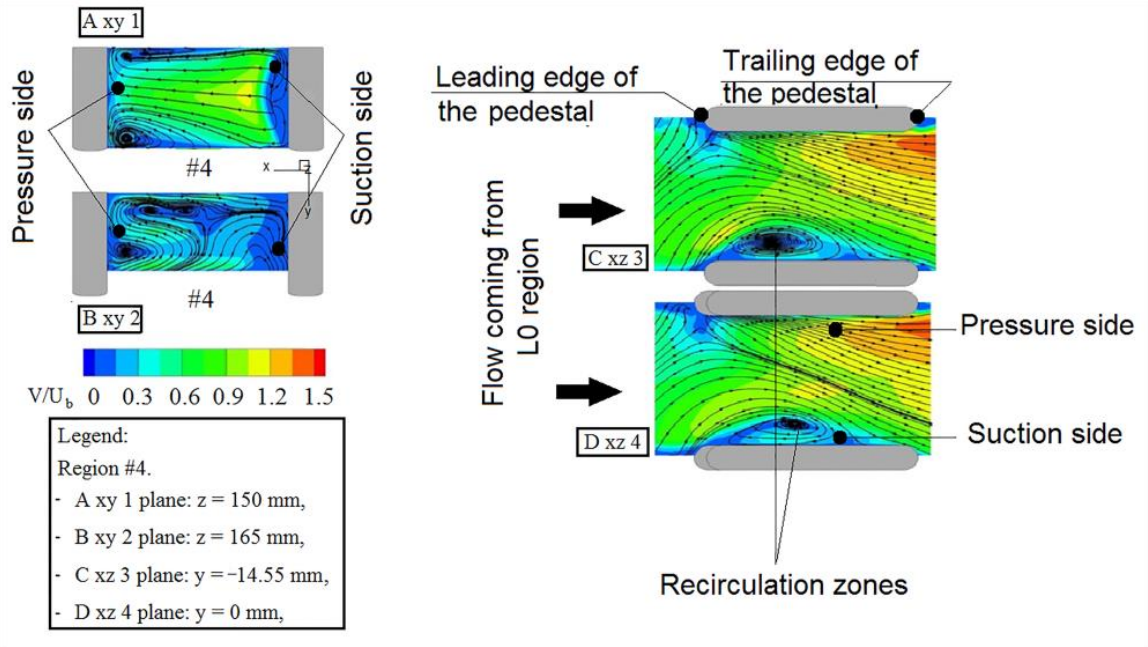

Figure 5. 4. Details of the 3D inter-pedestals flow structures – PIV data [52**]**

5.1.2 Open tip case

In the open tip configuration, a rate of 12.5 % of the coolant flows out through the five holes in the tip region. Contrary to the closed tip, the coolant is insured by the axial direction over the L1 region. In the open tip configuration, there are two directions where the coolant is discharged through the exit at the trailing edge of and also through the five holes from the tip. Figures 5.5 and 5.6 illustrate the obtained HTC distributions. Qualitatively, the distribution of HTC is more homogeneous as compared to the closed tip case. The observed homogeneity may be explained by the disappearance of the recirculation zone at the tip so that the coolant may reach upper of the blade tip region. This favourable direction is shown to affect the values of HTC levels at the pedestal's region. Also, it is seen clear that the intensity of HTC values is lower

for the open tip configuration compared to the closed tip. The development of the flow inside L0 and L1 regions is practically the same as seen in the closed tip case. The effect of redirecting wall on the L0 flow cross section and the reduction of the flow cooling along the L1 region, from the hub towards the tip, are the same as explained previously, but the values of HTC are lower compared to the previous case. This decrease is related to the reduction in the mass flow rate crossing the L1 region of about 12.5%, which reduces the coolant velocity across each inter-pedestal region, hence reducing the heat exchange efficiency.

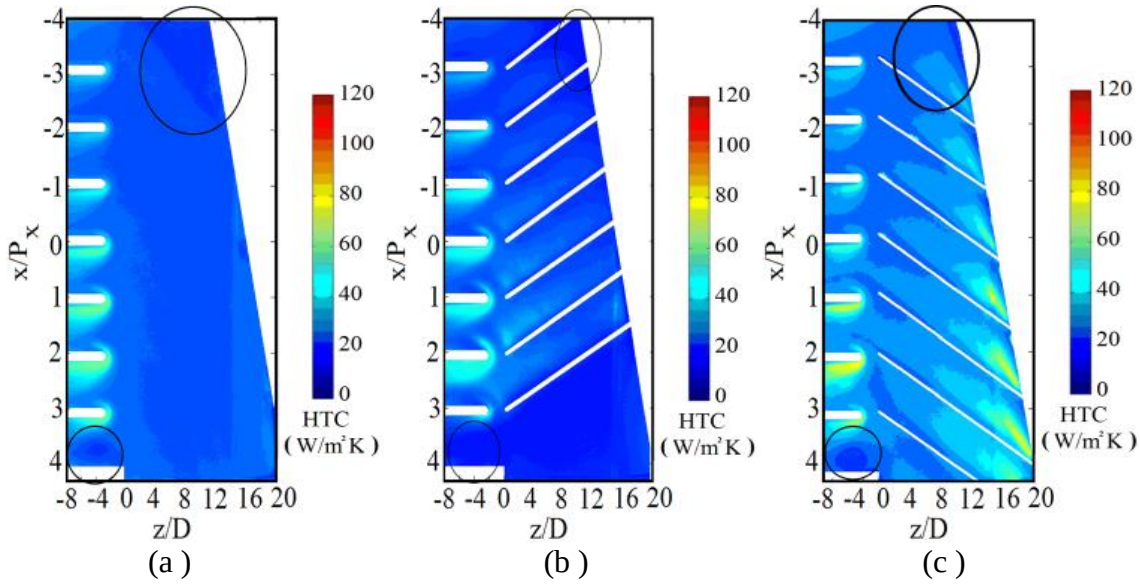

Figure 5. 5. 2D maps of HTC [W/m^{2}K] in region L0, Open tip case, Re =10000:
a) Smooth, b) Ribs -60°, c) Ribs +60°.

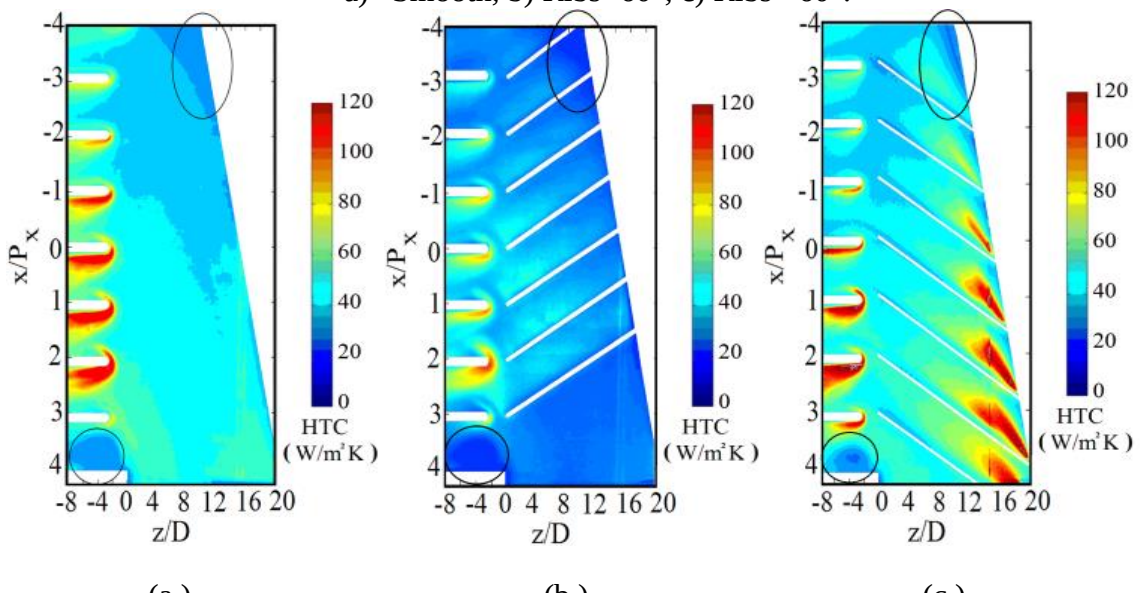

Figure 5. 6. 2D maps of HTC [W/m^{2}K] in region L0, Open tip case, Re =40000:
(a) Smooth, (b) Ribs -60°, (c) Ribs +60°.

5.1.3 Derived HTC correlations for stationary conditions

Two correlations for estimating the average Nusselt number at L0 and L1 regions have been developed by using the local values of HTC. The post processing of the TLC images allowed obtaining 2D maps of HTC distributions. For a given *(i, j)* pixel location of the L1 and L0 regions, a h_{expij} (experimental HTC local value at the *(i,j)* location) is attributed and a local experimental Nusselt number $Nu_{\exp ij}$ is evaluated as follows:

$$Nu_{\exp ij} = \frac{h_{expij} D_h}{k_{co}} \quad (5.1)$$

Where h_{expij} is the experimental HTC local value at the *(i,j)* location of the regions' matrix, D_h the hydraulic diameter, and k_{co} the coolant thermal conductivity estimated at the film temperature T_f.

5.1.3.1 Simple HTC correlation

A simple correlation is proposed for the three surface configurations (smooth, +60° ribs and -60° ribs) as follows:

$$\overline{Nu_{\#Å}} = c.Re^n \text{ , with Å} = \{L0, 1, 2, 3, 4, 5, 6, 7, 8\} \quad (5.2)$$

The coefficient *c* and the exponent *n* are determined by minimizing the standard deviation between the curve fittings and the experimental data. Each data point is the average of six repeated tests with about 10% of uncertainly for each Reynolds number.

For the L0 region, all the data points were fitted for the range of Reynolds numbers in between 10000 and 40000. The obtained c and *n* of the simple correlation form (equ. 5.2) are listed in tables 5.1 and 5.2 .

Table 5. 1 : Coefficient *c* and exponent *n* in the Nusselt correlation – Closed tip

Inter pedestals ID	Smooth		Ribs +60°		Ribs -60°	
	c	*n*	*c*	n	*c*	n
L0 region	0.0831	0.6500	0.0720	0.7007	0.0771	0.6624
# 8 Tip	0.3312	0.5167	0.0617	0.6844	0.7787	0.4292
# 7	0.1013	0.646	0.1151	0.6378	0.5269	0.4833
# 6	0.0653	0.7017	0.1145	0.6386	0.3929	0.526
# 5	0.1028	0.6759	0.0944	0.6683	0.3163	0.5639
# 4	0.2765	0.5906	0.1203	0.6579	0.3498	0.5592
# 3	0.4672	0.5436	0.2548	0.5886	0.1696	0.6385
# 2	0.5857	0.5264	0.5598	0.5263	0.1536	0.6556
# 1 Hub	2.3992	0.3155	0.2294	0.5775	0.4829	0.4588

Table 5. 2 : Coefficient *c* and exponent *n* in the Nusselt correlation – Open tip

Inter pedestals ID	Smooth		Ribs +60°		Ribs -60°	
	c	*n*	*c*	n	*c*	n
L0 region	0.1137	0.6238	0.0733	0.7019	0.1526	0.5889
# 8 Tip	0.7427	0.4298	0.27965	0.52805	0.1168	0.6092
# 7	0.0683	0.6808	0.37495	0.51709	0.1733	0.5825
# 6	0.0452	0.7272	0.07244	0.6775	0.1763	0.5927
# 5	0.0895	0.6801	0.0449	0.7216	0.3518	0.535
# 4	0.0796	0.7007	0.0708	0.6958	0.4561	0.5145
# 3	0.2767	0.5834	0.1705	0.6196	0.3372	0.5495
# 2	0.3548	0.5662	0.326	0.5666	0.4700	0.5230
# 1 Hub	2.1325	0.3242	0.67187	0.46104	0.1447	0.5805

Figure 5.7 illustrates the obtained results for the L0 region for the different cooling configurations, for closed tip and open tip. Concerning L1 region, comparisons of derived correlation results and experimental data are presented in figures 5.8 and 5.9, for closed tip and open tip conditions, respectively. For the closed tip, the maximum discrepancies are shown to be within ±10%; however, for the open tip configuration, discrepancies are within ±13% for Ribs +60° surface, and ±10% for the smooth and Ribs -60° surfaces. As a conclusion, there is a good agreement between the proposed correlation and experimental points.

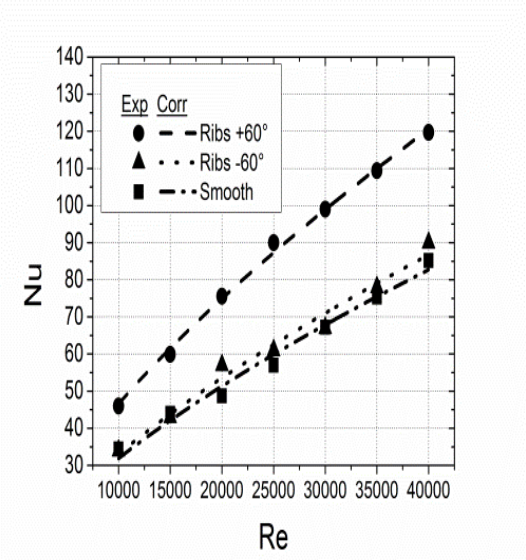

(a)

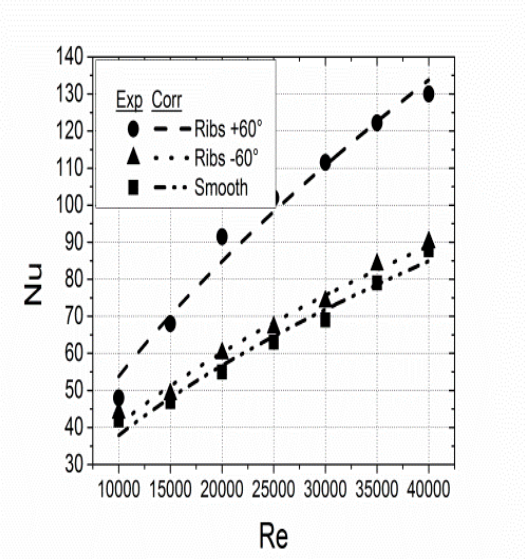

(b)

Figure 5. 7: Average Nusselt number in L0 region for: a) Closed tip, b) Open tip.

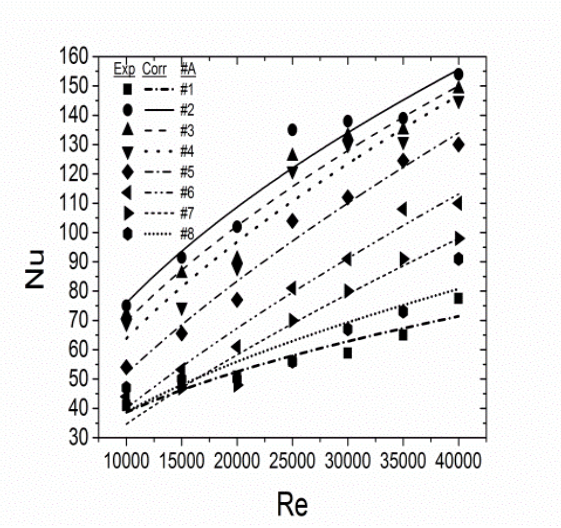

(a)

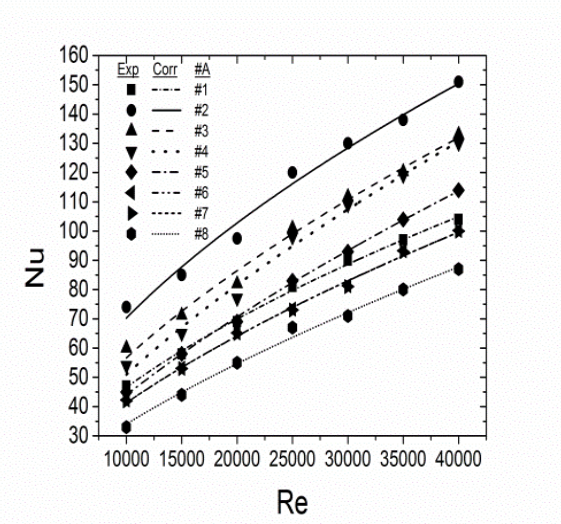

(b)

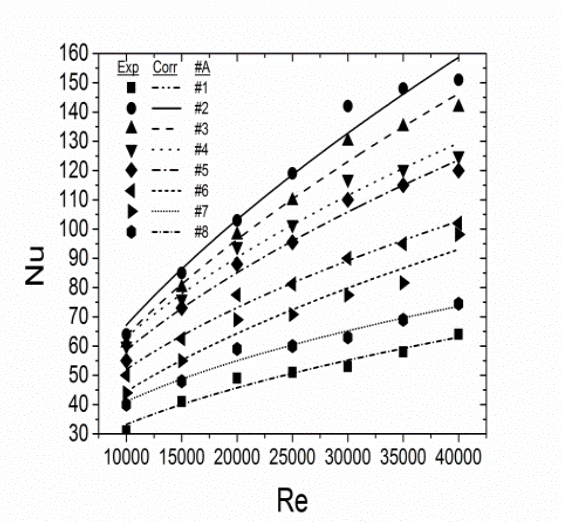

(c)

Figure 5. 8: Correlated Nusselt number, Closed tip: a) Smooth, b) Ribs +60°, c) Ribs -60°.

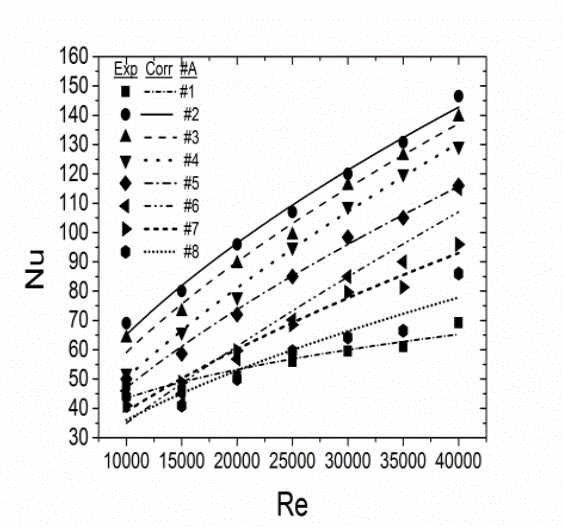

(a)

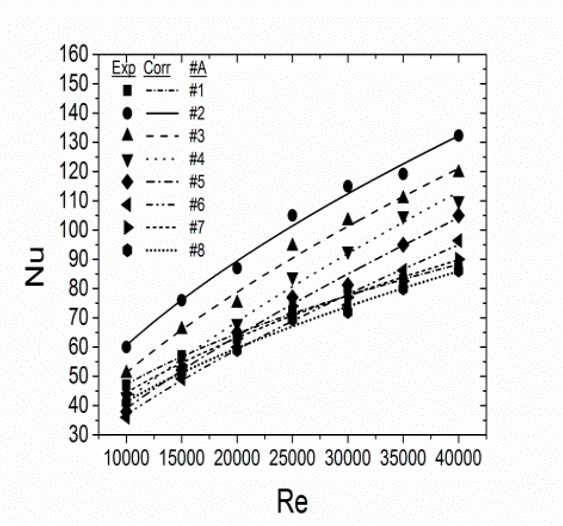

(b)

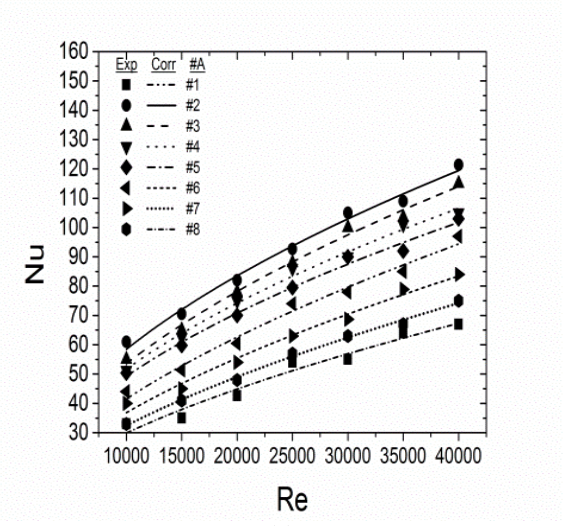

(c)

Figure 5. 9: Correlated Nusselt number, Open tip: a) Smooth, b) Ribs +60°, c) Ribs -60°.

5.1.3.2 Complex HTC correlation

In the previous simple correlation (equ. 5.2), for each specific #A region, the obtained curves fitting do well predict the variation of the Nusselt number when the Reynolds number increases. However, in the open literature, it has been often stated that the heat transfer is not the same along the radial direction [3, 12, 14, 22, 23, 24, and 61]. The new proposed complex correlation form considers the variation of the aero-thermal field along the radial direction of the L1 region. Consequently, the average Nusselt number is a function of *Re* and *Pr* in addition to the fraction of the radial distance *Xr*; using the following equation:

$$\overline{Nu_{\#Å}} = \left.\frac{\sum_{i=1}^{imax}\sum_{j=1}^{jmax}(Nu_{expij})}{imax.jmax}\right]_{\#\ Å=L1\ \text{region}} = c1.Re^{c2}.Pr^{c3}.Xr^{c4} \qquad (5.3)$$

Constants *c1*, *c2*, *c3* and *c4* are to be determined.

From the experimental results, the region #1 has the minimum HTC value. For this reason, it has been decided not to be taken into account during the curves fitting procedure.

After defining the different parameters of the proposed correlation and their constraints, a non-linear multiple variables fitting procedure was used to find the searched coefficients. Table 5. 3 summarizes the obtained coefficients for closed and open tip for the three surfaces and figures 5.10 and 5.11 illustrate the comparison between the obtained data using the complex correlation form and those from experimentation cases. Generally speaking, a good agreement between the data of the correlation and the experimental results with a relative error, which is, less than ±16%. In fact, a good fitting represents a good agreement between the data and the model, and it is reasonable to say that it represents a good estimation of the unknown parameters [64]. This seems reasonable but unfortunately not always true, and one may have a good fitting without having a good regression model. So, the difference in accuracies in our case might be attributed to the fact that the simple correlation form is a mono variable exponent function, whereas the second one is a complex nonlinear multivariable function.

In the open literature, no such kind of correlations was provided with interest to the effect of the radial position of pedestals on the heat transfer exchange (this phenomena is more emphasised in the rotating case), which is a step toward a good design of the internal cooling schemes of TE part of the blade.

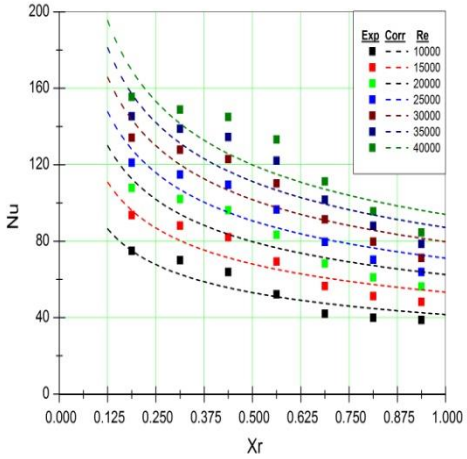

(a)

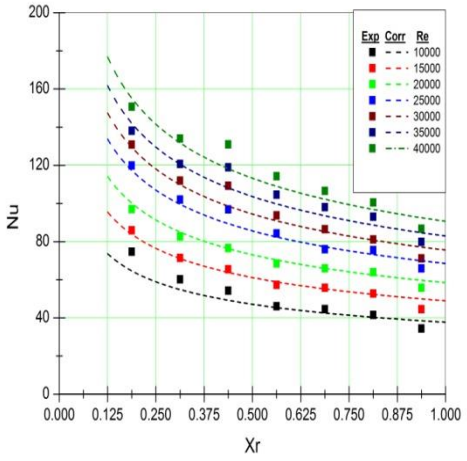

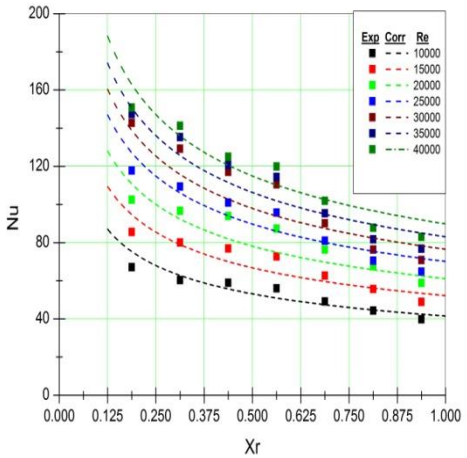

(c)

Figure 5. 10: Correlated Nusselt number, closed tip: a) Ribs +60° b) Smooth c) Ribs -60°.

Table 5. 3 : Coefficients of the Nusselt number correlations

	Surface case	*c1*	*c2*	*c3*	*c4*
Open tip	Smooth	0.12800	0.62260	0.39910	-0.33970
	Ribs +60°	0.13610	0.61690	0.39980	-0.26653
	Ribs -60°	0.27530	0. 54920	0.39970	-0.28470
Closed tip	Smooth	0.15128	0.61037	0.39800	-0.33033
	Ribs +60°	0.13347	0.62786	0.39960	-0.33563
	Ribs -60°	0.39301	0.52692	0.39500	-0.32011

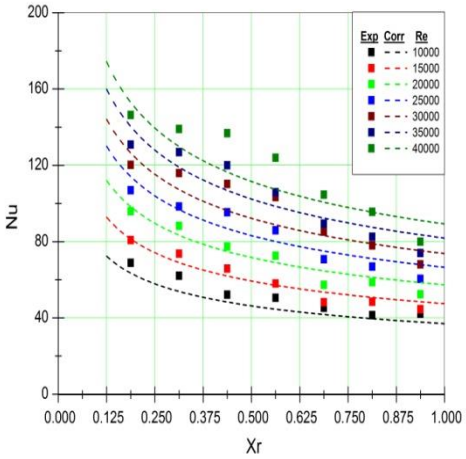

(a)

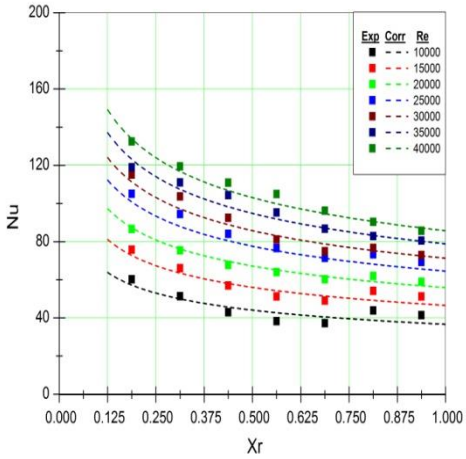

(b)

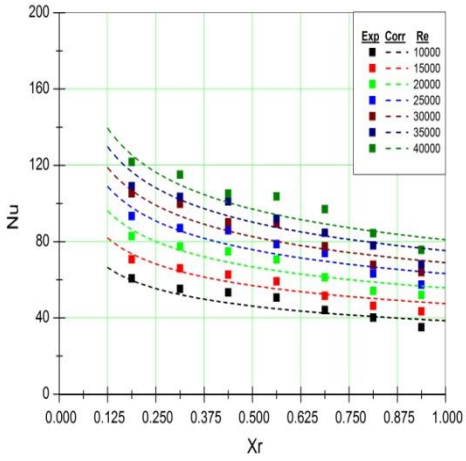

(c)

Figure 5. 11: Correlated Nusselt number, open tip, a) Ribs +60° b) Smooth c) Ribs -60 °.

5.2 Rotation effects

The overall flow behaviour under the rotation condition compared to the stationary case inside the channel can be commented by referring to the 2D HTC maps reported in the following subsections.

5.2.1 Closed tip

For a closed tip configuration, the comparison of figures 5.12 (b-c) and 5.13 (b-c) to figures 5.12 (a) and 5.13(a), respectively, highlights the effect of rotation compared to the stationary conditions. At first sight, in the central part of the L0 region the HTC values of rotation conditions are higher than those of the stationary case. Conversely, the flow in the channel exhibits a deviation towards the TE side that is stronger for Ro = 0.15 than for Ro = 0. This can be explained by taking into account the effect of the Coriolis forces which increase with the rotation number increase in the central part of the channel where the flow is forced to deviate towards the exit slots [25]. This deviation also explains, the extension of the recirculation zone near the redirecting wall towards the tip region. In the static condition, the core flow has a higher inertia than the slow flow in the boundary layers. Consistently, the former will tend to keep its radial direction while the boundary layer flow will be easily deviated towards TE. This leads to have a single concavity shape of the vector distributions. In fact, the *x* component of the pressure gradient induced by the Coriolis forces that act on the faster core flow causes an acceleration of the boundary layer flow along the radial direction, which explains the extension of high HTC values in the radial direction of the L0 region compared to the stationary case. Also, the velocity vector distributions assume a wavy shape distribution for higher Rotation number, but at radial positions closer to the channel tip, that is, after a sufficient space has been left for the development of the Coriolis effects. These effects are enhanced by the increase of the Reynolds number, which leads to a better efficiency of the coolant for Re= 40000 compared to Re= 20000 (comparison between figure 5.12 with figure 5.13) owing to the higher mass flow rate.

Regarding these local effects on the flow direction, the overall effect of the channel rotation is to flatten the velocity distribution and less thickening of the boundary layer on the lower and upper walls. Thus, the flow approaching the pedestal region, after being deviated by the redirecting wall, has no longer horseshoe vortices produced when the rotation number is increased, as seen in the case of stationary conditions. This can be attributed to a significant

acceleration of the near-wall flow caused by the rotational effects, which leads to thinner boundary layers and henceforward to the disappearance of the horseshoe vortices. Indeed, the boundary layer thickness affects the size of these secondary structures rigorously. Also, the inlet mass flow is discharged at the trailing edge with a linear distribution which is slightly increasing from #1 to #8. These conclusions are in good agreement with [25].

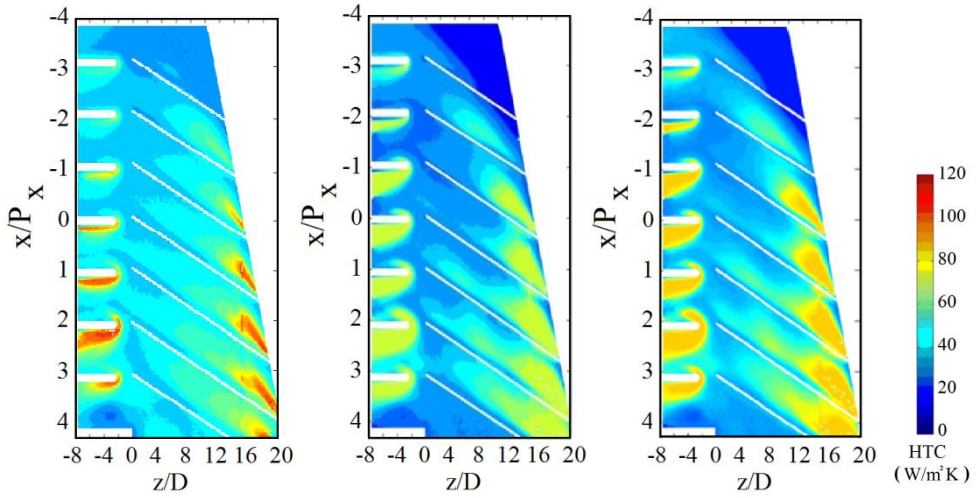

(a) (b) (c)

Figure 5. 12 : 2D maps of HTC [W/m^{2}K], with Rib +60° in region L0 in closed tip, for Re = 20000: a) Ro= 0, b) Ro= 0.10, c) Ro = 0.15.

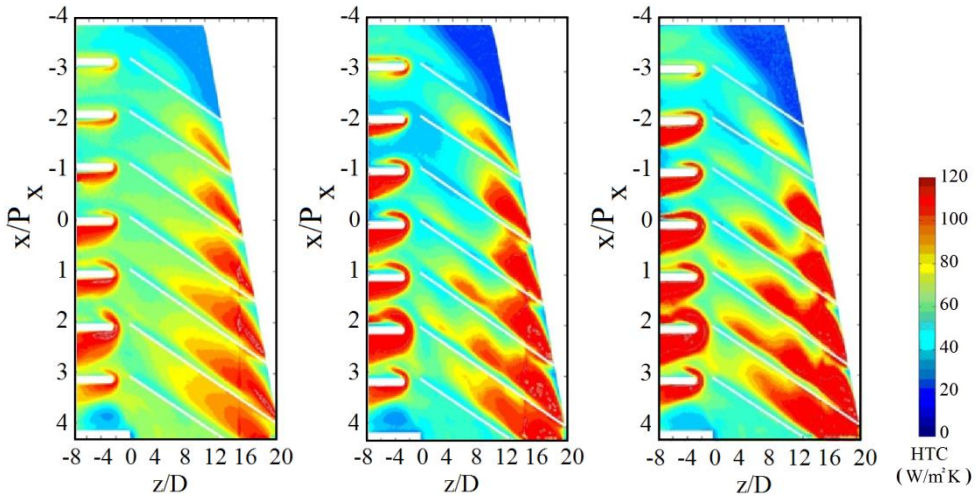

(a) (b) (c)

Figure 5. 13 : 2D maps of HTC [W/m^{2}K], with Rib +60° in region L0 in closed tip, for Re = 40000 : a) Ro= 0, b) Ro= 0.10, c) Ro = 0.15.

The reduced of the boundary layer thickness and the increased mass flow rate induce a better cooling efficiency at the pedestals L1 region as much as the rotation number is increasing,

compared to the stationary case. As reported on figure 5.14, the Nusselt ratio (Nu/Nu_{st}) increases with the the rotation number, for the different studied Reynolds number, allong the L1 region. It is clear that the increase in the Nusselt ratio depends on the inter-pedestal region.

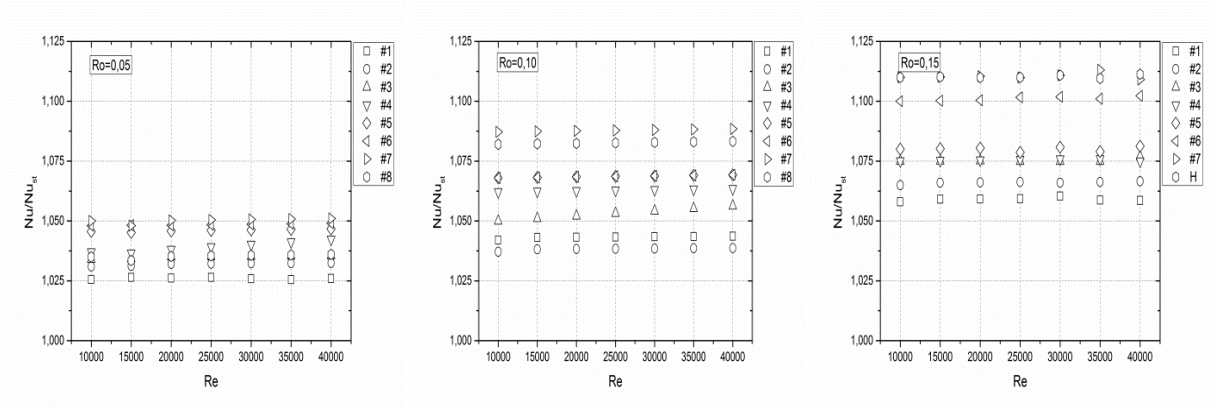

Figure 5. 14 : Ratio Nu/Nu_{st} versus the Reynolds number for different Rotation numbers along the L1 region, closed tip.

5.2.2 Open tip

Five holes at the blade tip region discharges 12.5 % of coolant air flow is discharged and the rest of the coolant is discharged through the trailing edge of the L1 region. The HTC follows the same behaviour of the closed tip. Figures 5.15 (b-c) and 5.16 (b-c) highlight in overall similar peculiar features, but the main differences are located near the tip region, because of the discharging flow leads to preserving the radial direction of the coolant air velocity, and for this reason the region of low HTC near the tip exit is less extended for all cases. The others typical features are conserved; indeed the recirculation region in #1 inter-pedestal. Also, the enhancement of the turbulence occurred at the L0 region, due to the centrifugal force which accelerates the flow towards the tip region. The existence of ribs at the L0 region, leads to improve the cooling of the heated plate by increasing its efficiency at this region. However, less coolant flow reaches L1 region, as compared to closed tip, which consequently affects the coolant efficiency.

Similar features as that noticed in the closed tip are highlighted with regard to the heat transfer enhancement due to existing ribs at the L0 region and the increase of HTC with the rotation number. It is also possible to notice the size extension of the recirculation zone at region #1 due to centrifugal force, compared to stationary case, and subsequently, HTC distribution is

more homogeneous than in the closed tip. The effect of the recirculation zone at the tip region is cancelled, and the combined effect of turbulence and Coriolis force induces a better cooling of the heated plate at L0 region as seen from 2D distributions of HTC in figures 5.15 (b-c) and 5.16 (b-c). However; it is noticed that the values of Nusselt ratio Nu/N_{st} are seen to be lower than those in case of closed tip as highlighted by figures 5.14 and figure 5.17. For example, for #7 and #8 regions, the increase in Nusselt ratio Nu/N_{st} is about 11 - 12% in the closed tip which becomes about 8% in the open tip. This difference is related to the existing recirculation zone in the closed tip and the restriction of passage area towards the trailing edge. In the open tip, this recirculation zone is less extended so that the coolant is turbulence but less accelerated and reaches the regions #7 and #8 with a higher film temperature that leads to decrease the coolant efficiency.

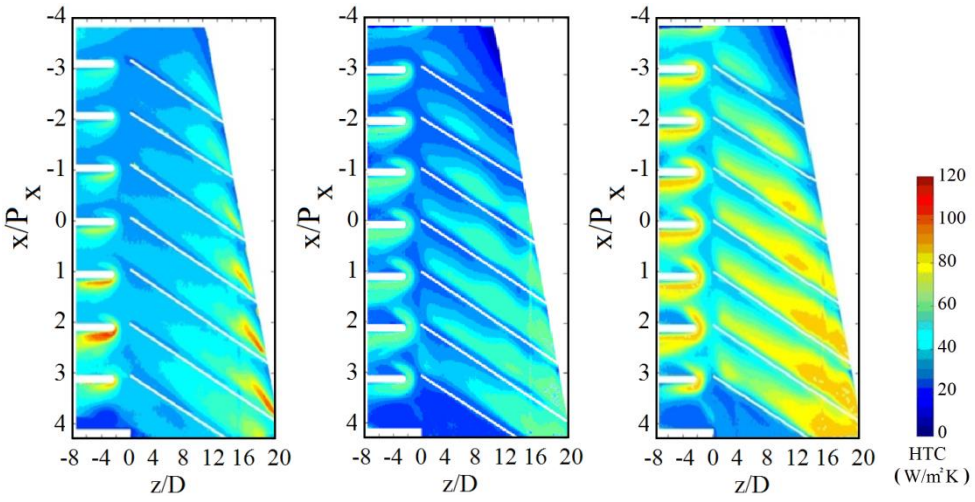

(a) (b) (c)

Figure 5. 15 : 2D maps of HTC [W/m^{2}K] open tip, regions L0+L1, with Rib +60° in region L0 for Re = 20000. a) Ro= 0, b) Ro= 0.10, c) Ro = 0.15.

As reported on figure 5.17 , the Nusselt ratio (Nu/Nu_{st}) increases along the L1 region with the increase of rotation number, for the different Reynolds number. It is clear that the increase of the Nusselt ratio depends on the inter-pedestal region, but in this case the increase is less high than the one depicted for the closed tip.

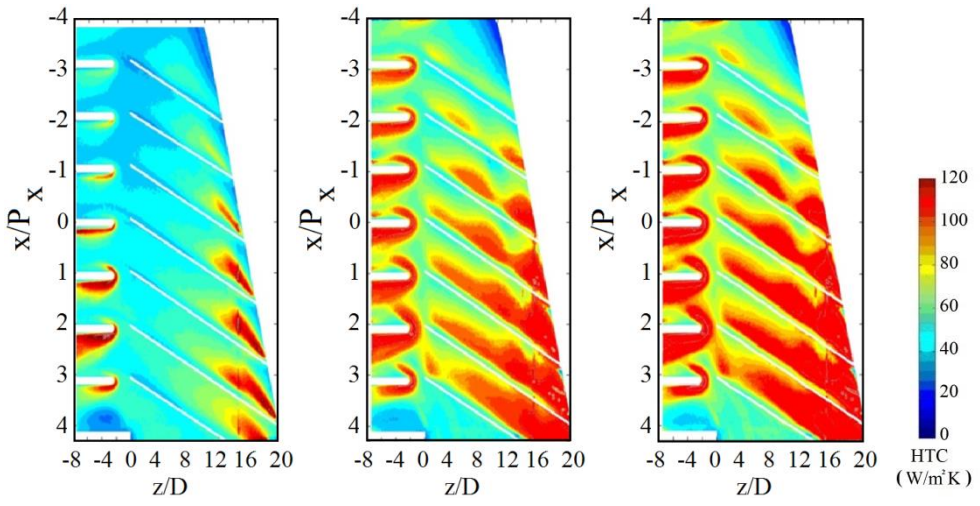

(a) (b) (c)

Figure 5. 16 : 2D maps of HTC [W/m^{2}K] open tip configuration, regions L0+L1, with Rib +60° in region L0 for Re = 40000 : a) Ro= 0, b) Ro= 0.10, c) Ro = 0.15

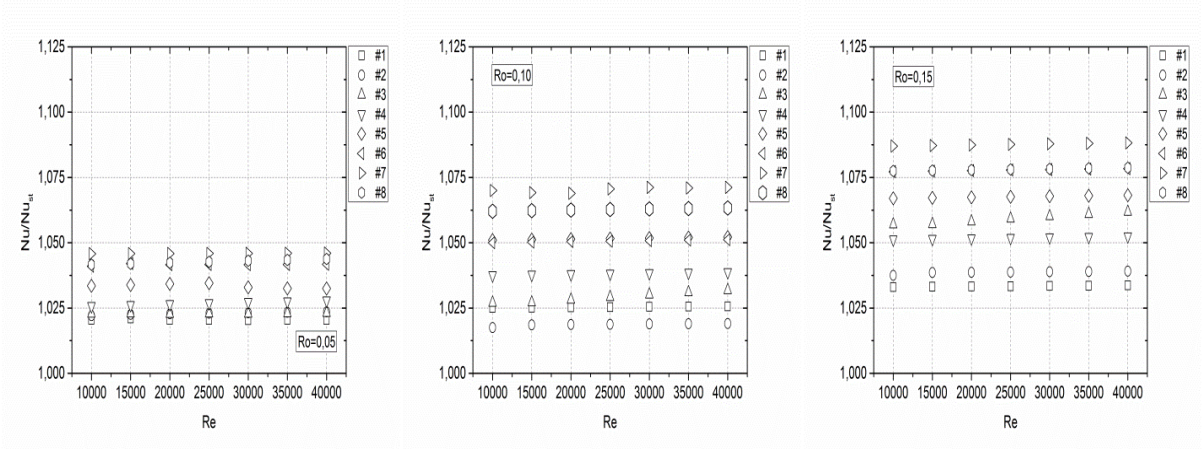

(a) (b) (c)

Figure 5. 17 : Ratio of Nu/Nust versus the Reynolds number for different Rotation numbers along the L1 region, Open tip.

5.2.3 Derived HTC correlations for the rotating conditions

Two different correlations are developed based on HTC local values used for estimating the averaged Nusselt number at L0 and L1 regions in terms of *Re, Ro, Pr* and the fraction of radial distance. A fitting function procedure has been applied to L1 region. For each studied Reynolds number tests were repeated six times, so that each data point is the average of six measurements. Over the range of Reynolds numbers all the data points of the two studied

geometries (open tip and closed tip) were fitted into a simple correlation and a complex correlation.

5.2.3.1 Simple correlation

This first simple form of correlation is proposed for a quick estimation of Nusselt number at each #A inter-pedestals region. First, the average Nusselt number is defined as a function of the Reynolds number and the rotation number. The Reynolds number is between 10000 -40000 and the Rossby number is from 0 to 0.15.

$$Nu = (a + b.Ro^{c}).Re^{d} \tag{5.4}$$

Where a, b, c and d are constants to be determined. In fact, because the stationary state the results have been taken into account to correlate the Nusselt number, the term $(a + b.Ro^{c})$ finds its form in order to reproduce both the stationary and the rotating state. In the stationary conditions Ro is equal to zero but the Nusselt number can not be equal to zero if the term $(a + b.Ro^{c})$ has been instead chosen to be $(a\,Ro^{c})$.

From Fig. 5.18 and 5.19 it is clear that HTC values increase with the Reynolds number, as it is explained by the fact that for each Rossby number for high the Reynolds number there is more coolant and a better cooling of the heated plate, both for an open tip and a closed tip. Also, the decrease of the average Nusselt number is going from the region #2 to the region #8. This is explained by the fact that the coolant arriving at the L1 region remains still fresh so that the film temperature is higher resulting in a better cooling of the heated plate. From the region # 2 towards the region # 8, the average Nusselt number values decrease. In fact, the coolant becomes hotter after interacting with the ribs and the heated plate in L0 region, due to turbulence and Coriolis effects which reduce the cooling efficiency as much as it goes toward the tip region. Also, it is seen that the regions #5, #6 and #7 have close values of the average Nusselt number, but the region #8 has a lower value in comparison with other inter-pedestals regions, except #1 region where the recirculation zone induces lower HTC values as less air passes through this region. These observations are still valid for all Rossby number from 0 to 0.15. The rotation induces an increase in the averaged HTC values due to the combined effect of turbulence, Coriolis and centrifugal forces which tend to increase with Rossby number.

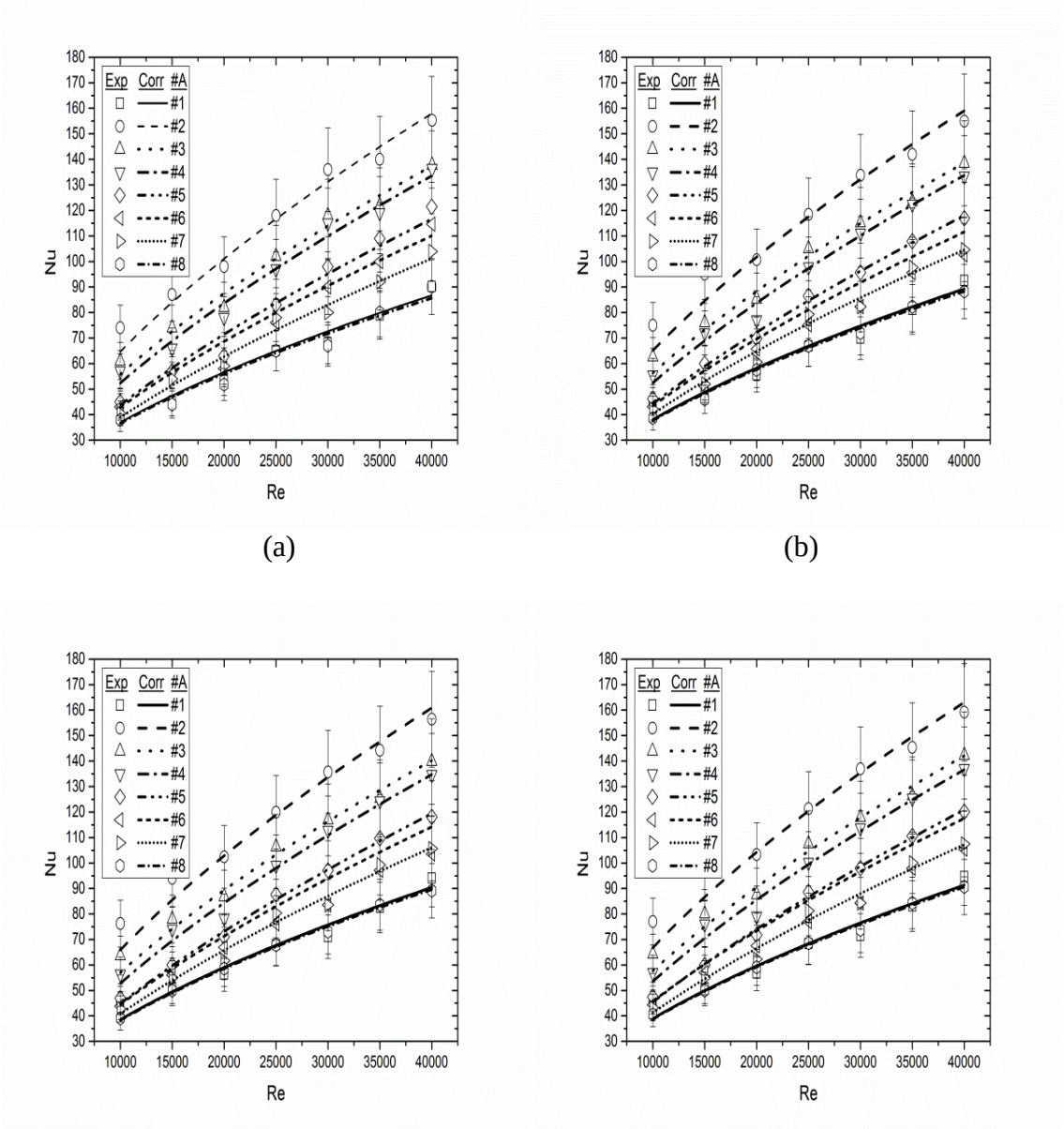

Figure 5. 18 : Nusselt number versus Re=10000-40000, Closed tip:
a) Ro = 0, b) Ro= 0.05, c) Ro = 0.10, d) Ro = 0.15.

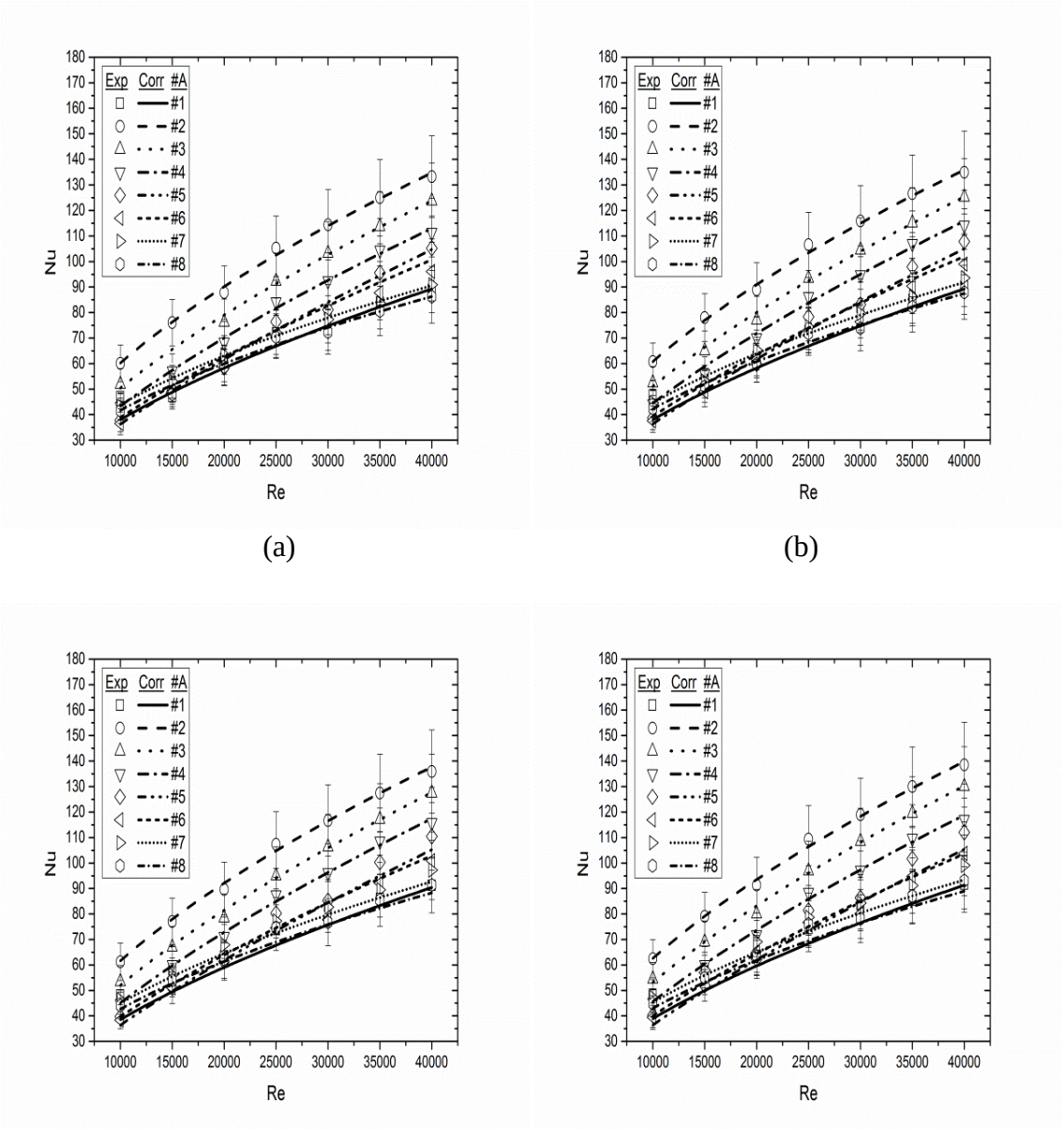

Figure 5. 19 : Nusselt number versus Re=10000-40000 for an open tip:
a) Ro= 0, b) Ro= 0.05, c) Ro = 0.10, d) Ro = 0.15

The obtained values of coefficients *a*,*b*,*c* and *d* and *n* in HTC correlations are summarized in tables 5.4 and 5.5, for the closed tip and open tip, respectively.

Table 5. 4 : Coefficients of Nusselt number correlation, closed tip.

Coefficient	*Region # A*							
	# 1	*# 2*	*# 3*	*# 4*	*# 5*	*# 6*	*# 7*	*# 8*
a	0.1279	0.1710	0.1310	0.1040	0.0651	0.0811	0.0676	0.1283
b	0.0191	0.0706	0.0470	0.2070	0.0183	0.0861	0.0110	0.0224
c	0.5425	1.3468	1.2031	2.3310	1.0732	1.4473	0.5222	0.5784
d	0.6152	0.6444	0.6501	0.6755	0.7069	0.6807	0.6899	0.6137

Table 5. 5: Coefficients of Nusselt number correlation, open tip.

Coefficient	*Region # A*							
	# 1	*# 2*	*# 3*	*# 4*	*# 5*	*# 6*	*# 7*	*# 8*
a	0.0720	0.1646	0.1337	0.1198	0.1032	0.0660	0.0985	0.1017
b	0.0899	0.0783	0.0791	0.0277	0.0325	0.03253	0.0492	0.0658
c	1.7801	1.3331	1.2930	0.8717	0.9204	0.8204	1.2220	1.3581
d	0.6722	0.6335	0.6450	0.6455	0.6550	0.6905	0.6455	0.6375

This first proposed correlation of Nusselt number is limited even it allows a quick estimation of the average and local Nusselt number. As noticed from these results the Nusselt number is varying along the radial distance from hub to tip region, because of changing in the coolant temperature due to interaction with the heated plate and the turbulence. For this purpose, another correlation that takes into account the effect of Reynolds number, Rossby number, Prandtl number and the radial hub to tip distance in the L1 region is proposed.

5.2.3.2 Complex correlation

The average Nusselt number is correlated as a function of *Re, Ro, Pr* in addition to the fraction of the radial distance Xr . The same procedure has been followed to estimate the average Nusselt number in the pixel matrix of the *L1* region, as explained previously.

$$Nu == (a + b.Ro^{c}) \, . Re^{d} \, . Pr^{e} . Xr^{f} \tag{5.5}$$

With *a, b, c, d, e* and *f* are the constants to be determined for all configurations both closed tip and open tip, considering the Reynolds number between10000 - 40000, the Rossby number 0 - 0.15, and the Prandtl number of coolant estimated at the film temperature T_f. In fact, the power coefficient of Prandtl number is constrained to be between 0.3 and 0.4, which is according to the values found in the open technical literature for the forced convection. The radial dimensionless

distance $\left(Xr = \frac{x}{L1\ lenght}\right)$ is obtained by dividing the radial distance, starting from the hub to the tip by the $L1$ region length. It is to say that Xr is different from the x/P_x ratio as defined in section 3. After defining the different parameters of the proposed correlation and their constraints, a nonlinear multiple variables procedure was used to fit adequate fitting curves defining the actual correlation. The obtained coefficients in Nusselt number correlation are presented in table 5.6.

Table 5. 6 : Coefficients in Nusselt number correlation

	A	*b*	*c*	*d*	*e*	*f*
Open tip	0.1405	0.0201	0.1022	0.6105	0.3995	-0.3171
Closed tip	0.1505	0.0812	0.7701	0.6115	0.3991	-0.3102

Figures 5.20 and 5.21 present the comparison between the proposed correlations and the experimental data for the closed tip and open tip, respectively. Generally, for each Reynolds number the curves are characterised by a decreasing trend along the L1 region from hub to tip. Indeed, higher values are found close to the hub at the region #2, but there are lower values seen at the region #8. This behaviour is still valid for all rotations, where it is noticed that the HTC values increase with a Rossby number from 0 to 0.15. All fitted curves of Nusselt number correlation are within an acceptable accuracy for the Reynolds number 10000 - 40000, and the Rossby number, between 0 – 0.15.

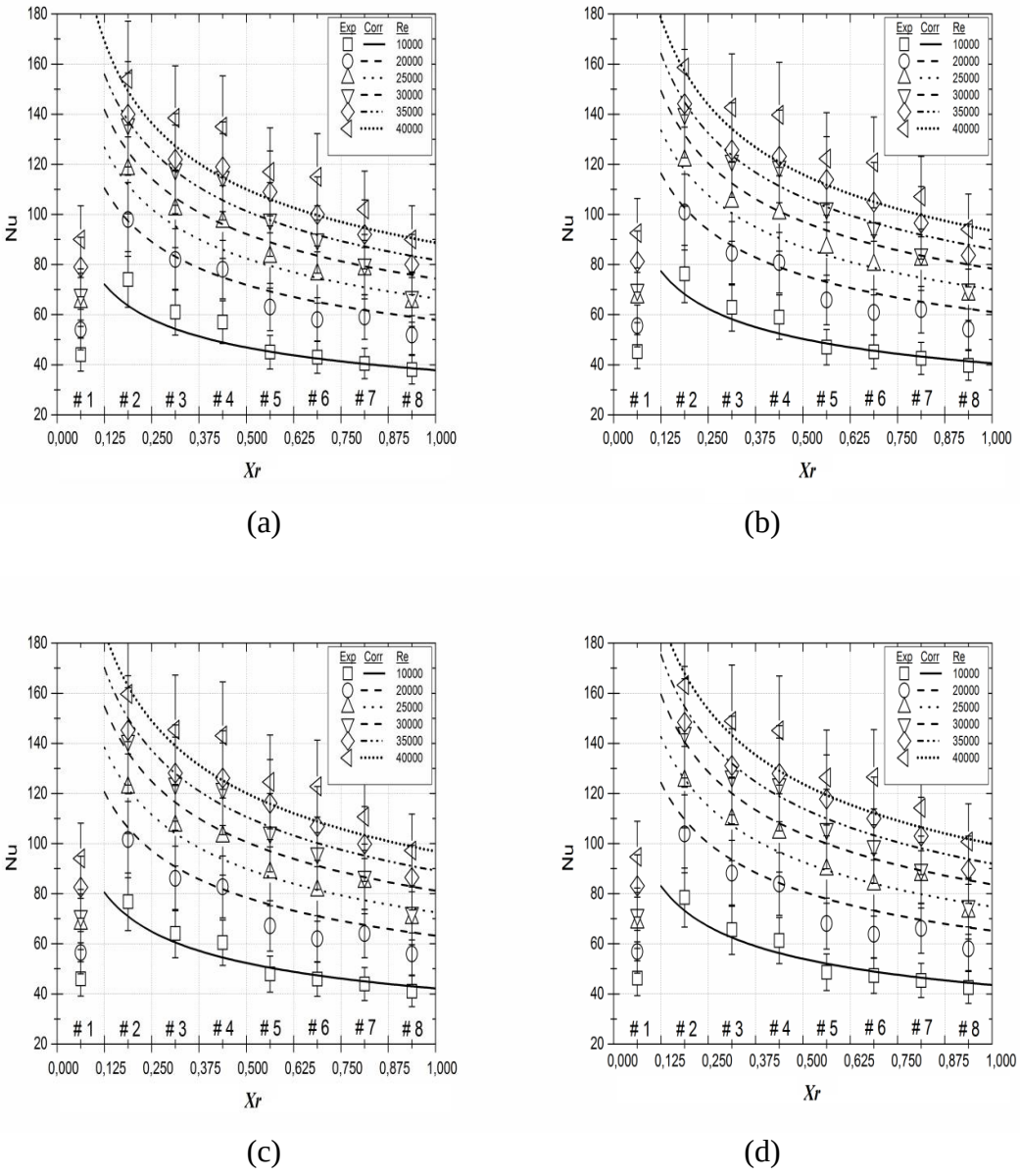

Figure 5. 20 : Comparison between the proposed correlation and the experimental data for the Ribs +60 and closed tip, along the radial distance for different Re number;
a) Ro =0, b) Ro =0.05, c) Ro =0.10 and d) Ro =0.15.

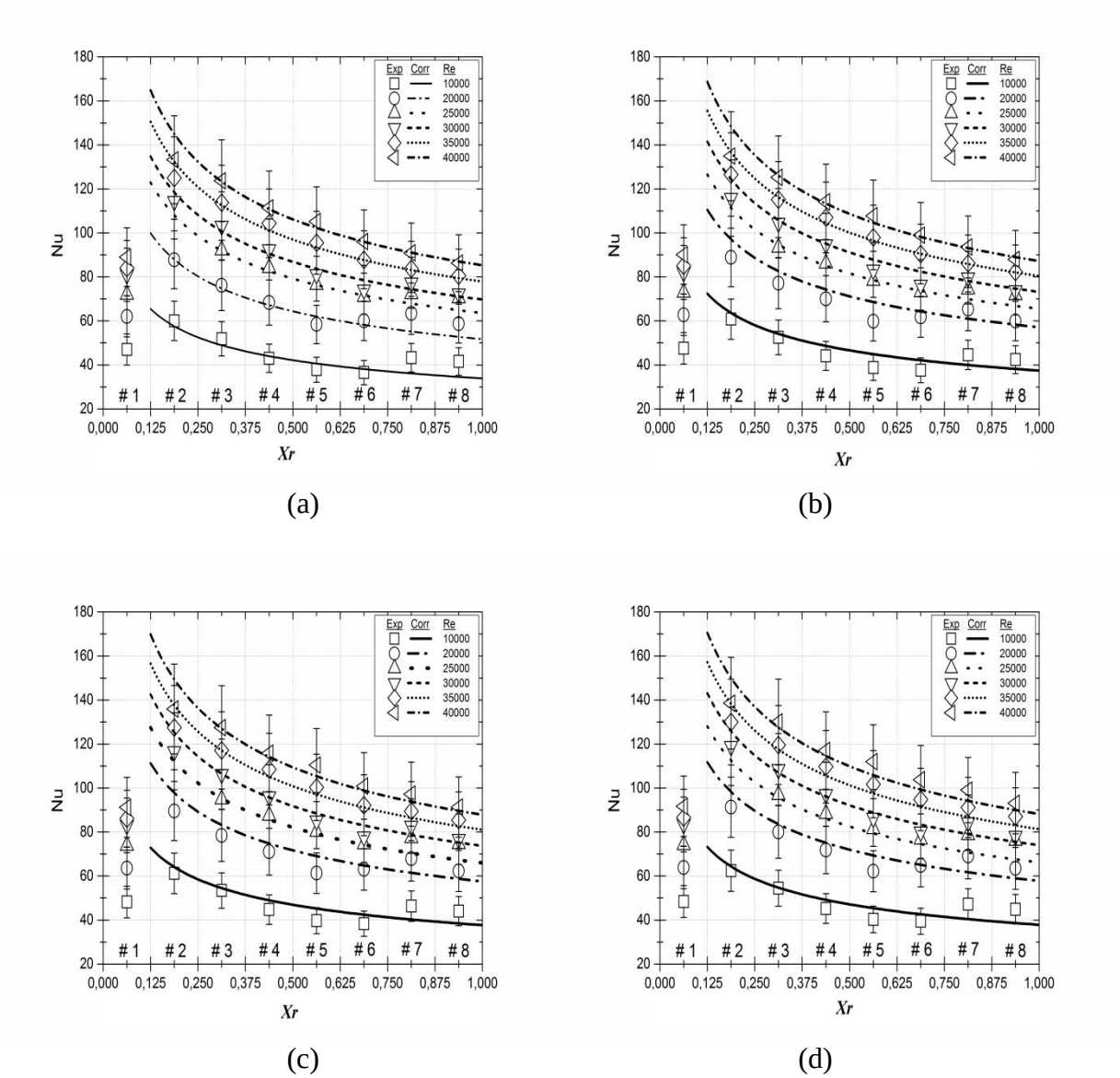

Figure 5. 21 : Comparison between the proposed correlation and the experimental data for the Ribs +60 and open tip, along the radial distance for different Re number;
a) Ro =0, b) Ro =0.05, c) Ro =0.10 and d) Ro =0.15.

In overall the percentage error is less than 16%. In fact, this good fitting represents a good agreement between the data and the model and we may conclude that the produced correlations may serve in predicting the average Nusselt number along the radial distance from hub to tip, for Reynolds number in between 10000 – 40000 and the Rossby number up to 0.15.

Conclusion:

In this study a non-intrusive TLC technique is used to investigate the heat transfer of a wedge shaped discharge duct of a an innovative gas turbine blade trailing edge cooling system scheme, using a closed tip and an open tip, for a Reynolds number in between 10000 - 40000 and a Rossby number in between 0 - 0.15. These parameters are quite good to extended to the real range of operating conditions of gas turbine applications. Based on the obtained results, the following conclusions can be made:

1. From 2D maps of HTC distribution maps, a first re-circulating zone appears at # 1 region near the hub, and another one (only with closed tip configuration) at the tip region. The size of these zones decreases by increasing the Reynolds number, for the same Rossby number. However, it increases by increasing the Rossby number under the same Reynolds number conditions due to combined the effect of the centrifugal and Coriolis forces.
2. The proposed geometry allowed comparing two different tip configurations without any great changes regarding structural modifications.
3. The Tip condition is shown to affect the cooling effectiveness.
4. The Coriolis force induces an axial acceleration to the fluid towards the trailing edge, and when it is combined to the centrifugal forces induces an extension of the low-HTC region near the redirecting wall and produces a global axialization of the flow.
5. The Reynolds number, Rossby number, Prandtl number and fraction of radial distance are quite sufficient parameters to quantify the heat transfer coefficient in order to evaluate the cooling effectiveness of the studied region of the turbine blade.

Chapter 6: Numerical study

Introduction

Steady-state RANS computations using the k-ω SST turbulence model and the isothermal steady airflows were conducted to solve the flow field of 30:1 scaled model (Fig 6.1) reproducing the innovative cooling scheme of a blade trailing edge (TE) of wedge discharging, and a row of enlarged pedestals and better understand its vortical structures developing inside of both static and rotating passages. The flow results are validated against the PIV measurements for Re = 20000 in the stationary and a rotating conditions for Ro= 0.23. The aerothermal results are comparable with experimental data obtained at Reynolds number = $\{20000, 30000\ and\ 40000\}$ and Rotation number in the range from 0 to 0.15. The results are reported in terms of detailed 2D maps of HTC over the suction side as well as an averaged Nusselt number evaluated inside the inter-pedestals ducts. These obtained results help to better describe the complex flow structures and to assess the aero-thermal performance of this cooling scheme.

6.1 Numerical methodology

The numerical simulations were conducted by using the solver ANSYS-Fluent 15.0. The energy equation was solved in term of total enthalpy for the stationary case and in term of rothalpy for the rotating case, since Navier-Stokes equations are solved in the rotating frame. The Navier-Stokes equations are solved using a SIMPLE-like (Semi-Implicit Method for Pressure-Linked Equations) algorithm with a convective diffusive equation for the pressure correction to impose the mass continuity considering the density variation. The convective schemes used a second order upwind interpolation scheme based on the NVA (normalized variable approach) known in the literature as self-filtered centered difference [51, 62] blended with a deferred approach with a first order upwind scheme. Turbulence was modelled by means of k − ω SST model with a hybrid near wall treatment, because it has been proved to predict reasonably well the flow field inside rotating channels [63]. All runs have been performed by assuming an isothermal air flow.

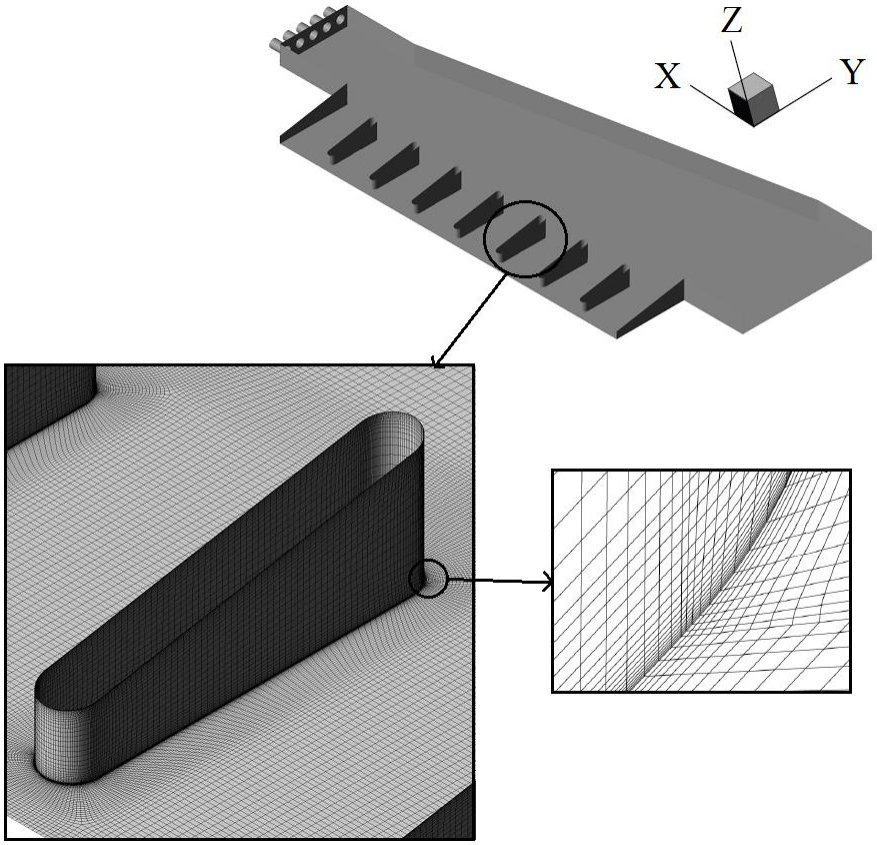

Figure 6. 1 : Computational domain and meshing.

The computational domain (Figure 6.1) is a multi-block structured mesh composed of 9.5 10^6 hexahedral cells. In fact, flow separations take place close to the pedestal surfaces which explains the need of very fine elements in the regions close to pedestals, where o- grids were used in order to obtain high orthogonally cells. Independence grid size was conducted to determine the most adequate mesh by verifying the stabilization of the recirculation bubble downstream of the sharp corner at the lowest radius and on the first pedestal. A value of $Y^+<1$ to guarantee the correct near-wall treatment and 15-20 elements inside the thermal layer on all viscous surfaces were used.

A porous media was imposed at the exit of the trailing edge. In fact, because as also reported by Andreini et al. [52], as the Rotation number exceeds a critical value of about 0.1, air is ingested from exit of trailing edge, due to the quite low pressure drop and high aspect ratio of the duct. A recirculation starts at the low radii because of the streamlines migration towards the tip due to centrifugal effects this, as also has been observed experimentally by Armellini et al. [45] and Pascotto et al. [53].

6.2 Boundary conditions

A velocity profile is imposed at the inlet while an ambient static pressure of 101325 *Pa* is maintained at the two exit sections. The inlet velocity profile was derived from the experimental data obtained by Armellini et al. [45] and Pascotto et al. [53] on an equivalent test rig at the University of Udine, in Italy. The inlet flow velocity was measured along the two symmetry planes of the entry rectangular section (Fig. 6.2) is slightly unbalanced due to the blockage effect of the redirecting wall. The velocity profile along the *y* axis is typically of a turbulent but not fully developed flow, in view of the short length of channel entry. The time averaged velocity profiles were used to perform a 2D interpolation to reconstruct the normal velocity for every inlet boundary face according to the equation reported by [45; 53]:

$$V_{inlet}\left(\frac{z}{D_h},\frac{y}{D_h}\right)=V_{meanZ}\left(\frac{y}{D_h}\right)\cdot\frac{V_{meanX}\left(\frac{z}{D_h}\right)}{V_{meanX}(0)} \tag{6.1}$$

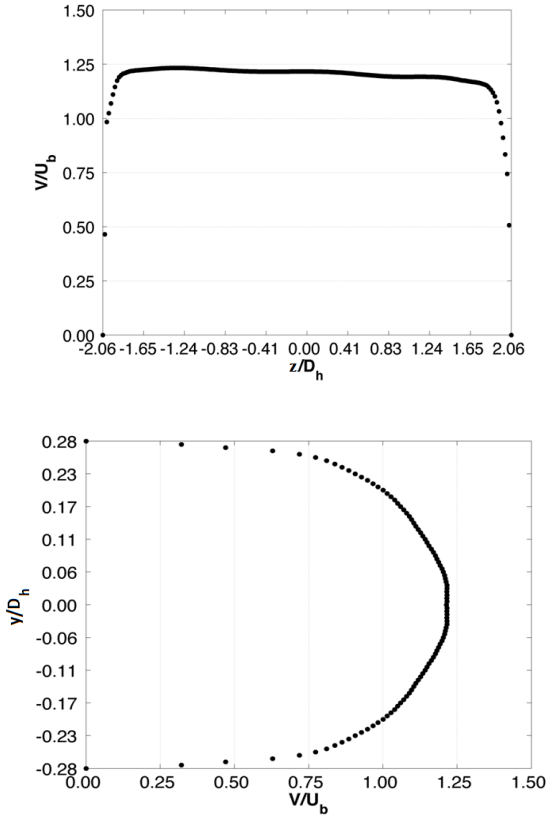

(a) V_{meanX} (z/D). (b) V_{meanZ} (y/D).

Figure 6. 2 : Inlet velocity profiles from experimentation of Armellini et al. [45]. Re = 20000, Ro = 0.

The inlet Reynolds number is based on the inlet hydraulic diameter D_h, corresponding to inlet bulk velocity U_b of approximately 5.2 *m/s* and 10.4 *m/s* for Re= 20000 and Re= 40000, respectively. An extrapolation of results corresponding to Re=20000 is done to get the velocity profile for Re=40000.

On the viscous walls, the adiabatic conditions and the no slip condition are applied except for the heated surface on which a constant heat flux ($\dot{Q}$= 1500[W/m^2]) is applied.

6.2.1. Mesh refinement near walls

Figure 6.3 gives an overview of Y^+ distribution for smooth and Ribs +60° surfaces along the three *x,y,z* directions on the bottom heated surface at a constant heat flux of 1500 W/m2. It can be seen that the Y^+ is clearly less than 1 for the two studied cases. Figure 6.3 highlights that the Y^+ values increase with the increase of the Ro number compared to stationary conditions. This increase may be due to the increase of turbulences due to the combined effects of Coriolis forces and axial acceleration of the flow.

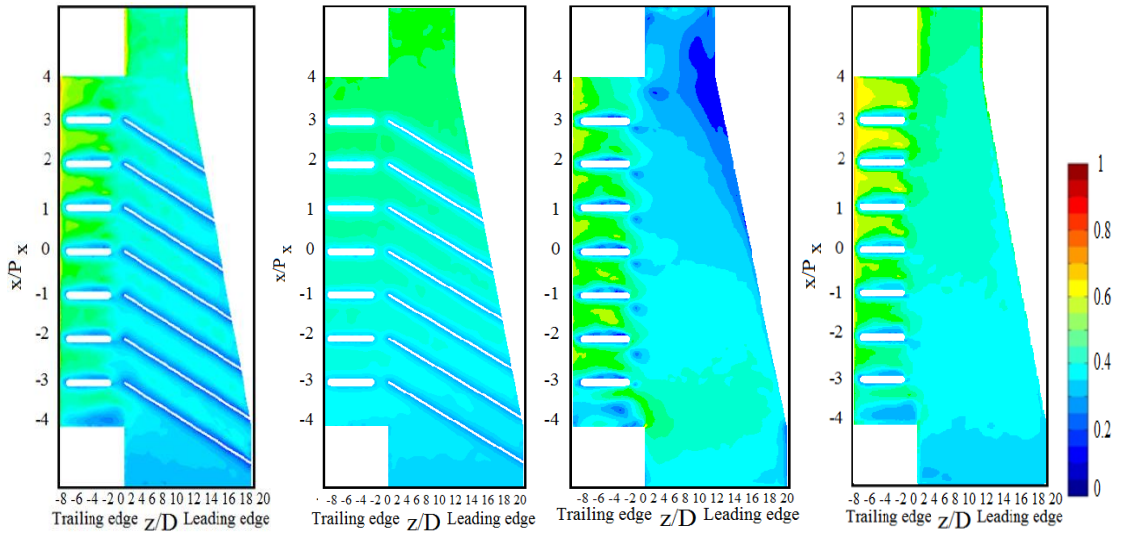

(a) (b) (c) (d)

Figure 6. 3 : 2D Y^+ maps distribution over the heated surface for Re=20000:
a) Ribs +60° open tip Ro= 0, b) Ribs +60° open tip Ro= 0 15,
c) Smooth surface closed tip Ro= 0, d) Smooth surface closed tip, Ro=0.15.

In the present study the numerical cases were confronted to those obtained experimentally. First, the numerical model has been compared to the experimental data at stationary and rotating condition at Ro=0.23 for Reynolds number of 20000 for only smooth

geometry the open and closed tip. Once the numerical simulation is validated, it was used to estimate the averaged Nusselt number at inter-pedestals regions for stationary and rotating conditions (Ro=0, 0.5, 0.10 and 0.15). Data are limited to Ro=0.15 because the test-rig cannot be used for Ro number higher than 0.17 when the Re equal to 40000 conditions. To reach higher values of Ro than 0.17, the test rig must have higher angular velocity which leads to high vibrations that can damage the test rig.

6.3 Results and discussions

6.3.1 Stationary case

The numerical model is validated for the case of smooth surface for both closed and open tip conditions, by comparing the numerical with experimental data under stationary and rotating conditions (Ro =0 to 0.23) at a Reynolds number of 20000 at the inlet condition. In the 2D maps of HTC the x/P_x is a dimensionless distance with the origin located on the mid span of L1 region, and z/D is a dimensionless distance with the origin located at the left plan of inlet section. x, P_x, z and D are the radial distance, inter-pedestals distance, axial distance and the distance from pedestal's leading edge to inlet section, respectively. In general, good agreements between numerical results and experiments results are well demonstrated through the figure 6.4, where the stream tracers in plane *xz* are reported for *y=0* .

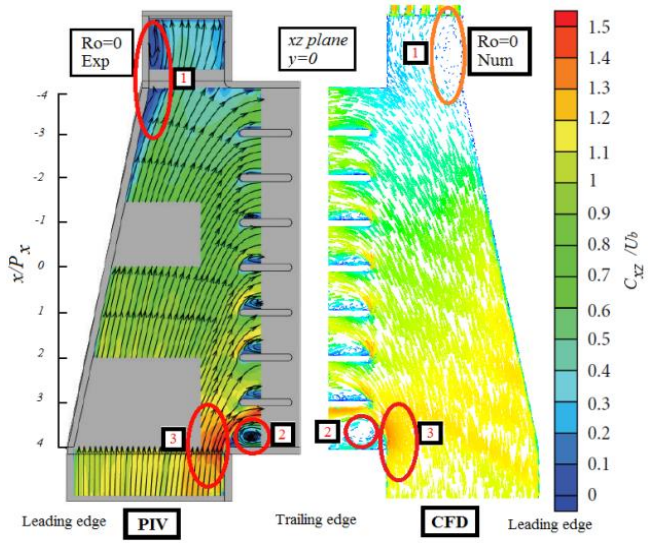

(a) (b)

Figure 6. 4: C_{xz}/U_b Velocity profile distribution, smooth surface, open tip, Re=20000, Ro=0: a) Experimental PIV data [52], b) Present numerical prediction.

This CFD model was able to capture both the main flow features and the velocity distributions as compared to the PIV data. The zones 1, 2 and 3 are well captured as shown by figure 6.4 and the flow paterns have practically the same positions and levels. In fact, the numerical model predicts very well the recirculating zone near the hub at the region # 1 in inter-pedestal, as well as the zone 1 near the tip.

For the closed tip (figure 6.5) highlights good qualitative agreement with experiments in term of HTC distribution. The CFD model captures well the recirculation zone at tip and hub, in *L1* there are high peaks of HTC close to the pedestal leading edge, but become lower at downstream along the channel. Another two regions of low-HTC value regions are located in the inter-pedestal vane near the hub and the tip along the redirecting wall, as they are attributed to the recirculation zones.

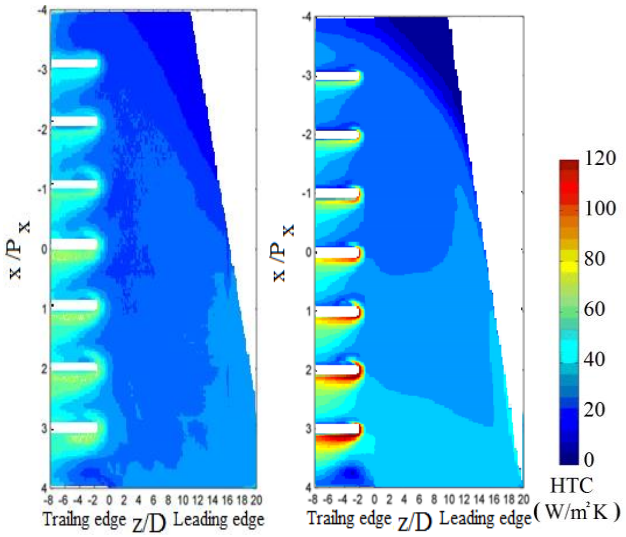

Figure 6. 5 : 2D maps of HTC [W/m^2 K], Smooth surface, Closed tip, Re=20000, Ro=0: a) Experimental, b) Numerical prediction

From the 2D maps of HTC (figure 6.5), it is noticed that the maximum HTC is reached on the leading edge of each pedestal at the stagnation point. As seen at the downstream of vanes, a horse shoe vortex is convected both over pressure and the suction side of the pedestal. This effect is maximum for the second pedestals but tends to decrease along the radial direction. The increase of the incidence angle on the leading edge and the subsequent recirculation bubble limits the increase in the heat transfer along the suction side. In the inter-pedestal vanes, an increment of HTC is clear from the pressure side to the suction side of the previous pedestal. This

phenomenon is due to the migration of cooling air from the above pressure side to the suction side.

To better quantify the agreement between numerical and experimental results, the HTC profiles inside the L1 region are reported along 4 span-wise lines (figure 6.6). The z/D=0 line corresponds to the entrance of L1 region, the z/D=-2 line to the pedestal leading edge, the z/D=-4 to the mid-channel position and z/D=-6 is located at the downstream of channel. The maximum value of HTC decreases along the L1 region for z/D= -2, -4 and -6. However, for z/D= 0, HTC is almost constant along the L1 region in the radial direction.

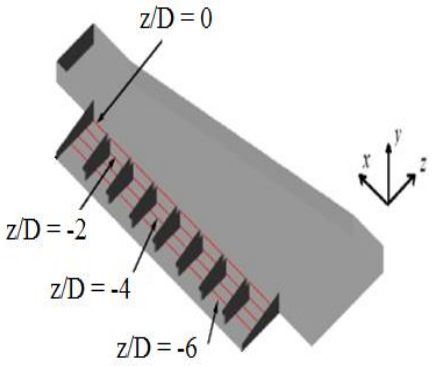

Figure 6. 6 : z/D Lines used to plot HTC

In overall the numerical results are said to be close to those of experimentation, but it is clearly seen that numerical predictions have higher values than experimental data, which are attributed to two possible reasons. The first is that the surface temperature is extracted from the obtained colour bitmap image (1296x964 pixels with a physical pixel size of 0.5*mm* x 0.5 *mm*) of the TLC painted surface color, through the quantification of the painted surface, using the *hue* parameter. However, some parts of TLC painted surface have a black color because they are over/less heated so the temperature of the surface at the black area is higher/lower than the maximum/minimum temperatures of the band-width activation temperature range of the used TLC. In this case, the pixels of the black areas have a special treatment to resolve the unavailability of the temperature information at these pixels. The given solution is to impose the maximum temperature of activation of the used TLC where areas are over heated, for example the recirculation zones near the tip and the hub. On the other hand, the minimum activation temperature of used TLC is imposed where areas are very cooled such as at of the leading edge and the downstream areas of the pedestals. This supposition may lead to some differences between numerical predictions and the experimental data. To avoid these black areas, the user

can increase the current intensity which is not really suitable because higher current intensity may damage and/or reduce TLC life span.

6.3.2 Rotation case

The rotational effect is analysed based on the numerical results obtained for Re = 20000 and Ro= 0.23 defined as:

$$Ro = \frac{\Omega \cdot D_h}{U_b} \approx \frac{\text{Coriolis Forces}}{\text{Inertial Forces}} \tag{6.2}$$

Where Ω is the angular velocity, D_h is the hydraulic diameter at the inlet section and U_b is the bulk velocity.

By considering a finite aspect-ratio on the flow path, it is fundamental to take into account the presence of Coriolis force; directed normal to the primary flow direction and axis of rotation. A pressure gradient is generated by the bulk velocity $\partial P/\partial x \approx 2\rho\,\Omega\,U_b$. For an outward flow, the trailing side of the blade is at high pressure (destabilized side) and the leading side is at low pressure (stabilized side).

The Coriolis force value is proportional to the velocity: approaching the walls that decreases due to no-slip condition and consequently is reduced; on the other hand the rotation-induced pressure gradient which is constant and this unbalanced of forces creates a net force which causes secondary flows in the cross sectional plane of the duct: the fluid is driven from the trailing side to leading side of the duct; also a return flow is established in the duct, creating two vortex pattern. The presence of the secondary flows alters the distribution of radial velocity and temperature, by increasing the friction and the heat transfer at walls with respect to the stationary case [24].

6.3.2.1 Closed tip conditions

Figure 6.7 illustrates the U velocity profile obtained experimentally and numerically in the inlet channel in the z direction at the x= 68.5 *mm* plane. As Ro increases, the flow imbalance towards the channel trailing side (z < 0) becomes stronger, as expected in view of the dependence of the potential flow effects on the channel angular velocity [52].

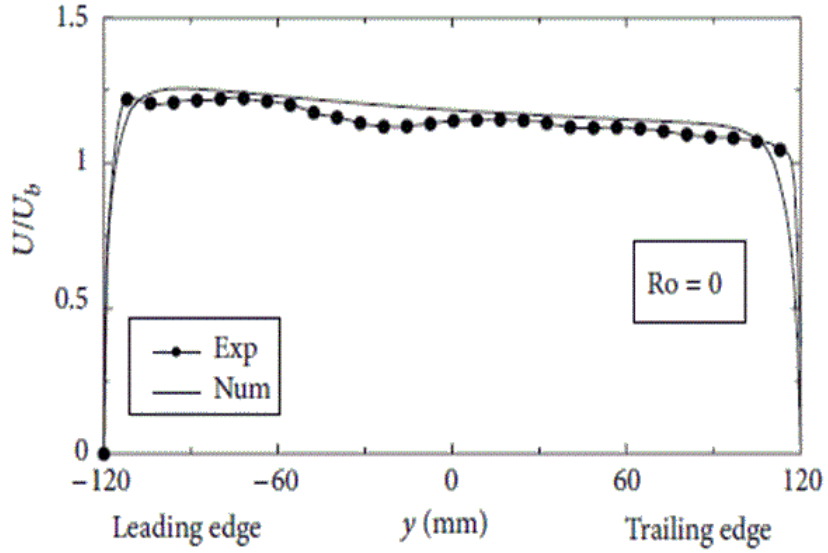

(a)

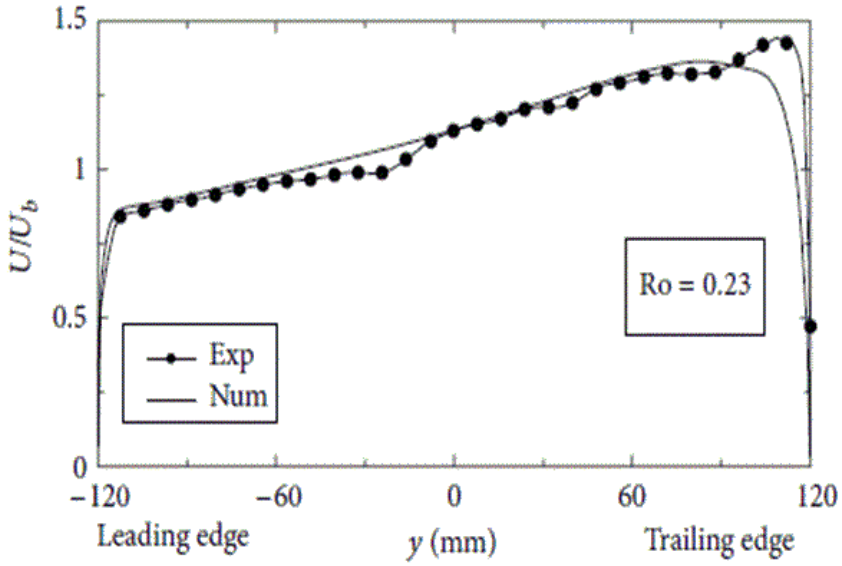

(b)

Figure 6. 7 : Comparison of experimental and numerical inlet velocity profiles, Smooth surface, closed tip, Re = 20000, a) Ro = 0, b) Ro = 0.23.

The effects of rotation on HTC distribution base on both numerical and experimental are illustrated by figure 6.8, while the spanwise profiles are presented in figure 6.9, for both numerical and experimental results. The centrifugal force produces a radial acceleration to the coolant, since for closed tip there is no outlet, and the pressure increases. On the other side, the Coriolis force induces an axial acceleration to the fluid towards the trailing edge. This combined effect apparently extends the low-HTC region near the redirecting wall and produces a global axialization of the air flow. In the central part of *L0* region and *L1* region, HTC values are higher compared with the stationary case. The high radial velocity acquired by the coolant increases the angle of attack on the pedestals, thus inducing a decrease of the heat transfer along the suction side due to the reduced mass flow and enlarged separation bubble of the suction side, and likewise the horse-shoe vortex is bended towards the pressure side. Concerning the spanwise distribution, for z/D=0 (figure 6.9a), it is possible to notice that the numerical results are close to experimental distribution. On the pedestal leading edge (z/D=-2, 6.10(b)), CFD seems to overestimate the peaks values of HTC. This difference is due to the fact that in experimental procedure, pixels over heated or cooled have a black colour because they are out of the band colour of the used TLC. To resolve this problem during the Matlab post-processing, the maximum temperature value supported by TLC is given to the overheated areas, and the lowest temperature of the band colour to areas overcooled. These suppositions may lead to differences between the experimental data and CFD results. Also, the fact to suppose that walls which are not heated are isolated, instead of taking into account heat losses, this may lead to less differences.

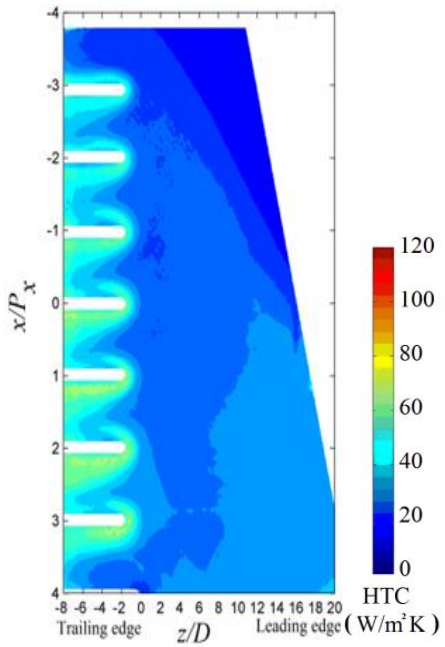

(a)

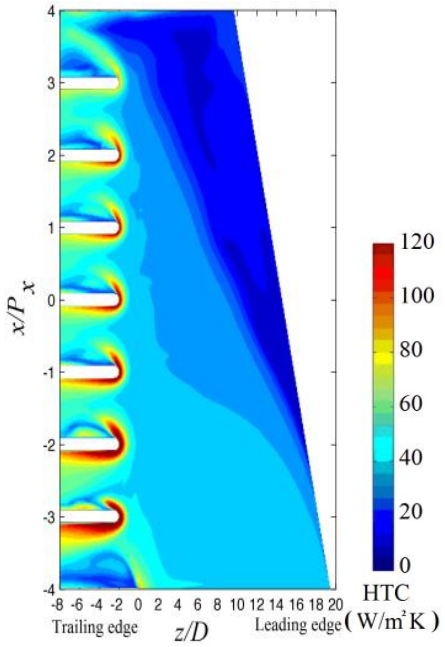

(b)

Figure 6. 8: 2D maps of HTC [W/m^2 K], Smooth surface, Closed tip, Re=20000, Ro=0.23
a) Experimental, b) Numerical predictions.

Downstream the channel, at the lines *z/D*=-4 and *z/D*=-6 (figure 6.9c and figure 6.9d), the same noticed remark as described above can be found, except for the first inter-pedestal vane: the experiments show a lower value of HTC as on the first pedestal over the suction side than that measured on the second one. By considering CFD predictions, the behaviour of HTC show that the peak reaches its maximum on the first pedestal suction side and then decreases along the radii. As revealed HTC values in the mid inter-pedestal predictions are reasonable compared to those obtained by [25].

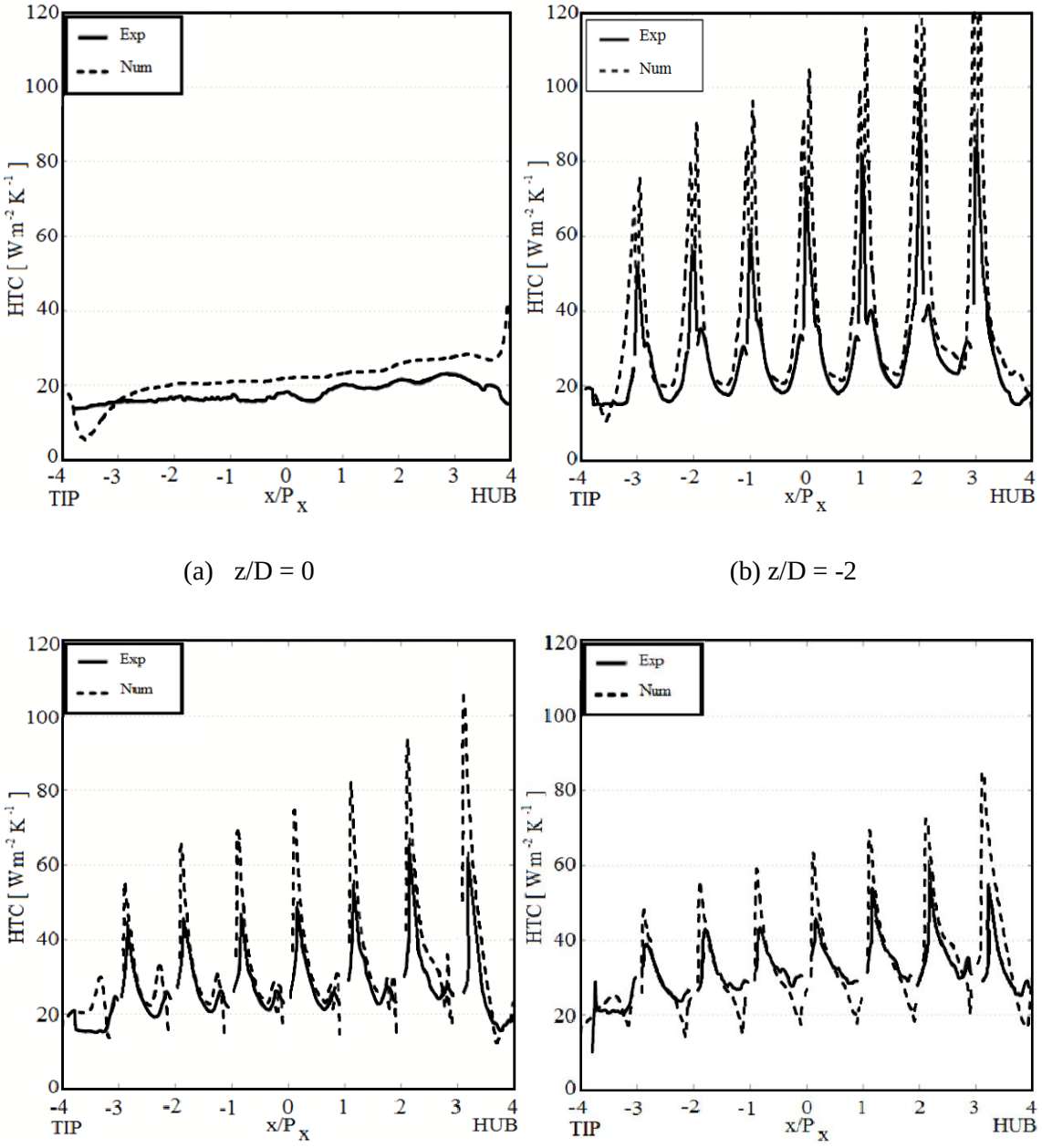

(a) z/D = 0 (b) z/D = -2

(c) z/D = 0 (d) z/D = -2

Figure 6. 9: HTC Spanwise profiles for, Smooth surface, Closed tip, Re=20000, Ro=0.23.

6.3.2.2 Open tip conditions

For the open tip, the HTC distributions as seen from figure 6.10 and figure 6.11 follow the same trends as in the case of closed tip, but there are some differences seen near the tip region. First, there is a reduction of the recirculation bubble which is evident for both the experiments and the predictions. Second, there is a clear difference in the last inter-pedestal vane # 8, where the effect on coolant at open tip has a greater radial velocity component which promotes the increment of HTC. By comparing between the numerical and experimental maps, it can be observed that the experimental HTC is less influenced by the tip outlet conditions than the numerical prediction. This can be attributed to the Matlab procedure itself, or related to the light response of the TLC and the sensitivity of the used camera.

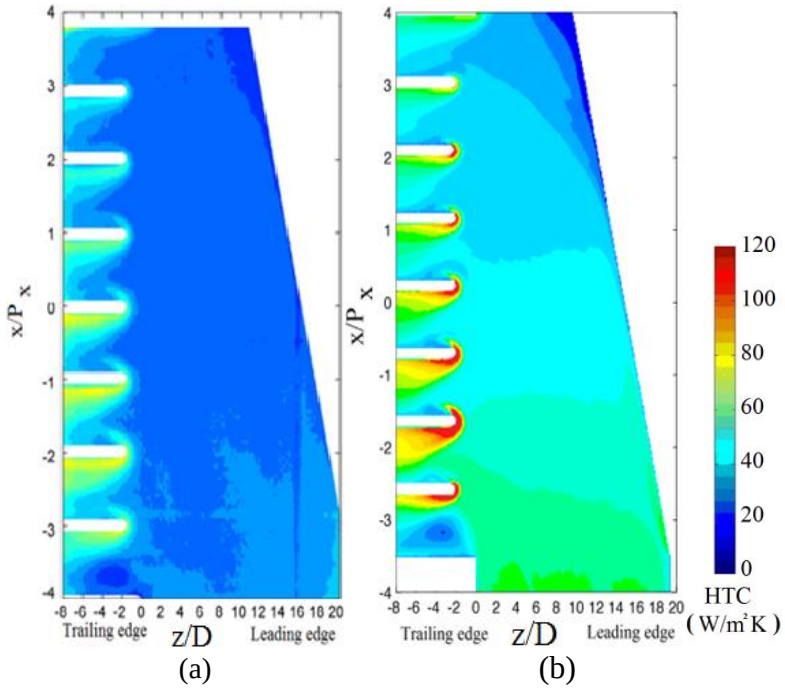

Figure 6. 10: 2D maps of HTC [W/m^2 K], Smooth surface, Open tip, Re=20000, Ro=0: a) Experimental, b) Numerical prediction.

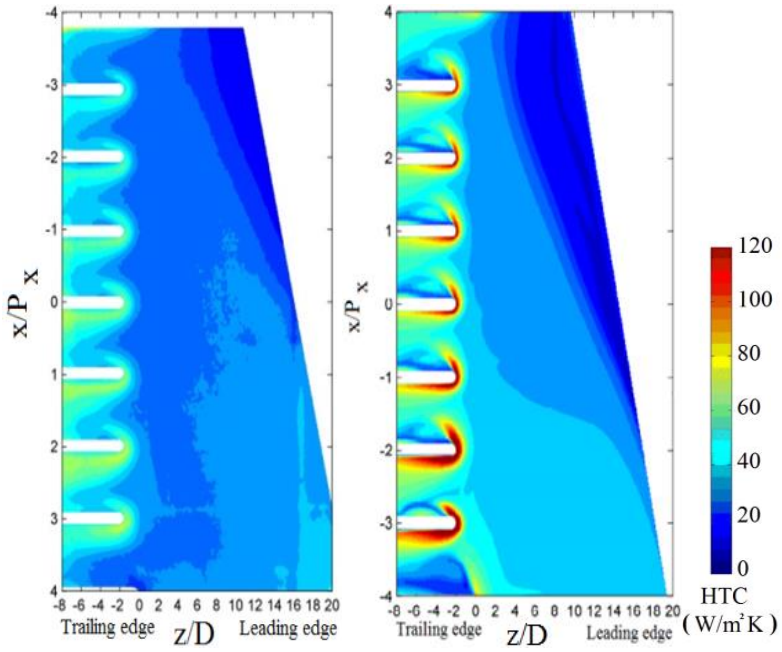

Figure 6. 11: 2D maps of HTC [W/m^2 K], Smooth surface, Open tip, Re=20000, Ro=0.23: a) Experimental b) Numerical prediction.

Concerning the HTC spanwise profiles (figure 6.12 and figure 6.13) they are varying with rotation, it seems that the peaks values of HTC for the case of open tip are less than with the closed tip, which can be explained by the fact that less flow rate exits from the tip region compared to the closed tip.

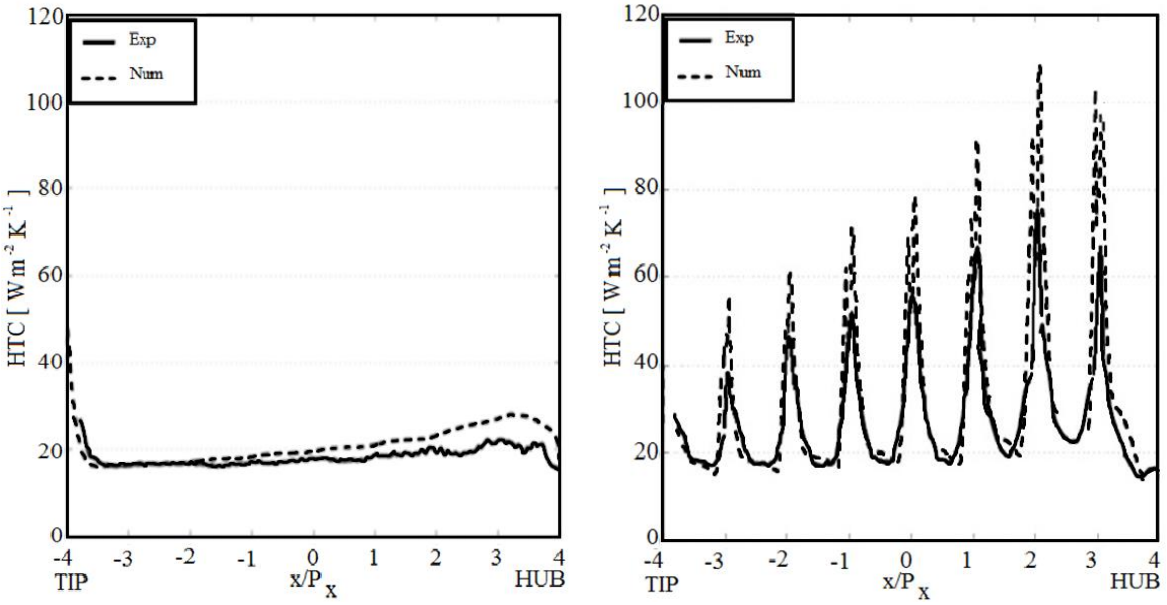

(a) z/D=0. (b) z/D=-2.

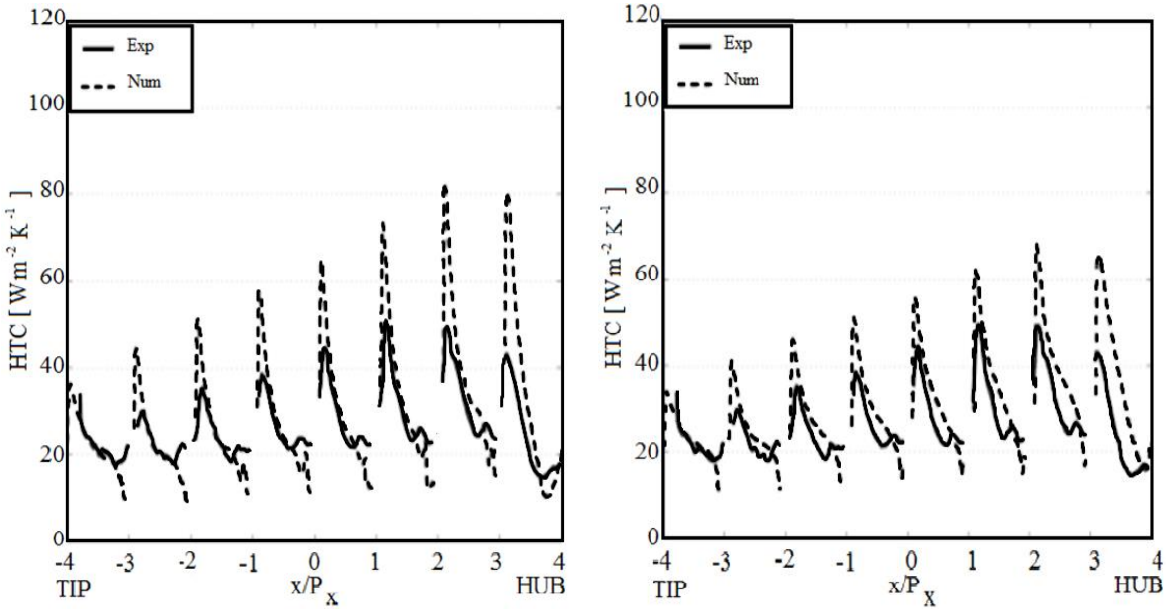

(c) z/D=-4. (d) z/D=-6.

Figure 6. 12 : Spanwise profiles of HTC: Smooth surface, Open tip, Re=20000, Ro=0.

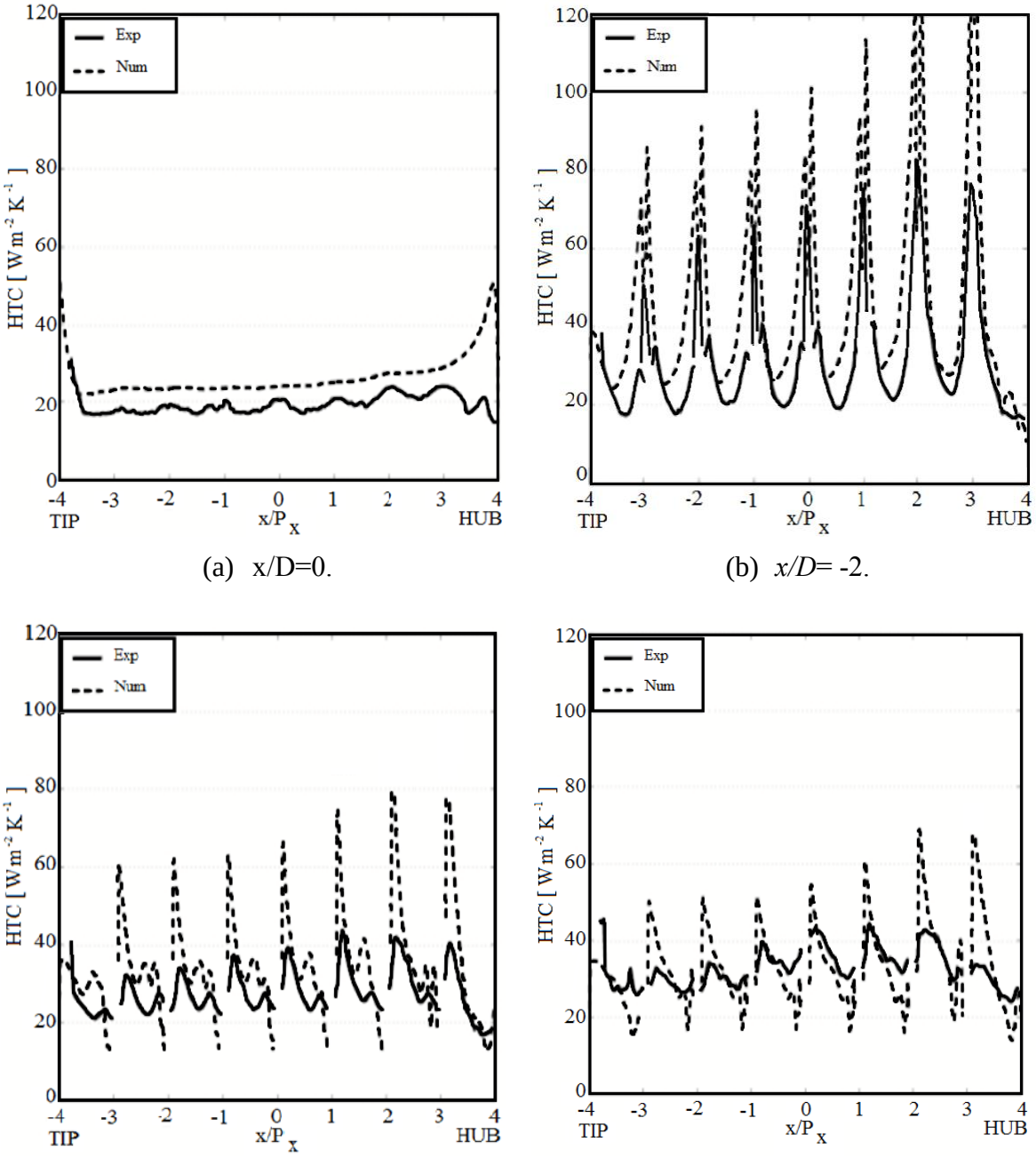

(a) x/D=0. (b) *x/D*= -2.

(c) *x/D*= -4. (d) *x/D*= -6.

Figure 6. 13 : HTC spanwise profiles, Smooth surface, Open tip, Re=20000, *Ro*=0.23

In the next are presented the results for the case of ribbed surface (Ribs +60°) for open tip under stationary with Ro= 0, Ro= 0.15 and Re=20000 and 40000.

From observation of figure 6.14, it is revealed that HTC reaches high values, especially near the inclined plane behind the ribs, but afterwards it tends to decrease from the hub to tip. Similarly, as for the smooth surface, the Ribs +60° surface has some particular features, with two noticed regions of low HTC attributed to a separation zone, the first in the inter pedestal vane near the hub (#1 region) and the second near the tip along the redirecting wall. The sizes of these zones of recirculation are seen to be reduced with the increase of *Re*, because more fresh air arrives at a higher velocity, hence increasing the cooling of hot plate at these two recirculation regions. Higher cooling effect is localised at the regions from # 2 to # 7 in comparison with regions # 1 and # 8. As seen the maximum HTC is reached on the leading edge side of each pedestal due to stagnation point and turbulence enhancement. Also, on the trailing edge side of each pedestal the distribution of HTC highlights the flow separation downstream of the pedestal channel. By arriving at L1 region, the air facing the pedestals is accelerated due to reduced passage area and subsequently the downstream area is well cooled than the upstream.

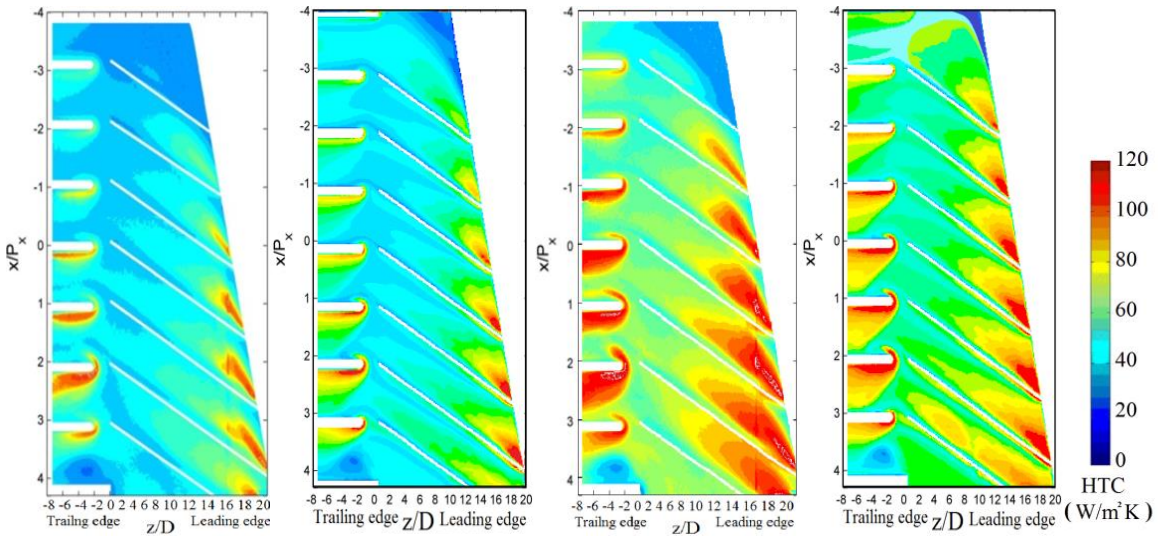

Figure 6. 14 : 2D maps of HTC [W/m^2 K], effect of Reynolds number, surface Ribs +60°, Closed tip: a) Re= 20000, Ro= 0, Experimental, b) Re= 20000, Ro= 0, Numerical, c) Re= 40000, Ro= 0, Experimental, (d) Re= 40000, Ro= 0, Numerical.

The comparison between predictions and experimental HTC maps for the smooth surface and the ribbed surface highlights that this latter has a better distribution of HTC, due to turbulence promotors making more fresh coolant arriving towards the heated surface. In contrary, for the smooth heated surface, due to development of the thermal and the dynamic boundary layers the cooling efficiency is lower.

Concerning the case of rotating case, figure 6.15 reveals that, in the central part of L0 and L1 regions, the value of HTC is higher than in the stationary case. Although, the centrifugal force displaces radially the coolant, the Coriolis force induces an axial acceleration to the fluid towards the trailing edge (Rectangle 2), and such a combined effect extends the low HTC region near the redirecting wall and produces a global axialization of the air flow. Therefore, the distributions on leading and trailing edges of each pedestal show higher values of HTC compared to the stationary case (figure 6.15 “Rectangle 3”, figure 6.17 and figure 6.19).

In fact the stagnation point moves downstream the pedestal channel and the separation becomes larger at the trailing side, and the peaks of HTC near the redirecting wall are stretched parallel with ribs orientation towards the trailing edge reducing the angle of attack of coolant at each pedestal and the global turbulence enhancement due to pedestals. Also, it can be seen, that the high Reynolds number tends to increase the turbulence behind the ribs, with more coolant towards the heated plate, hence resulting in a better cooling efficiency. In addition, HTC over the cooled regions behind the ribs have high values for Re=40000 more than for Re= 20000 (Figure 6.16 and figure 6.18).

In stationary conditions, higher Reynolds number induces a reduced size of recirculation zones near the hub (for the closed and the open tip) and near the tip (for closed tip only), because more fresh coolant reaches the recirculation zone and its size reduces as more coolant is imposed at entry.

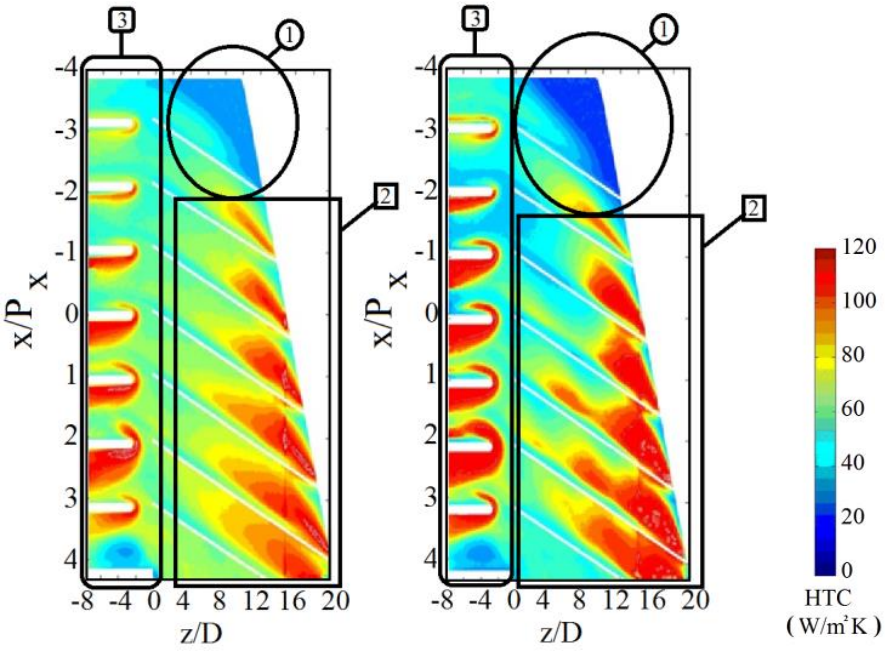

(a) (b)

Figure 6. 15 : 2D HTC [W/m^2 K] maps, effect of rotation, surface Ribs +60°, Closed tip, Re= 40000: a) Stationary, b) Rotation Ro=0.15.

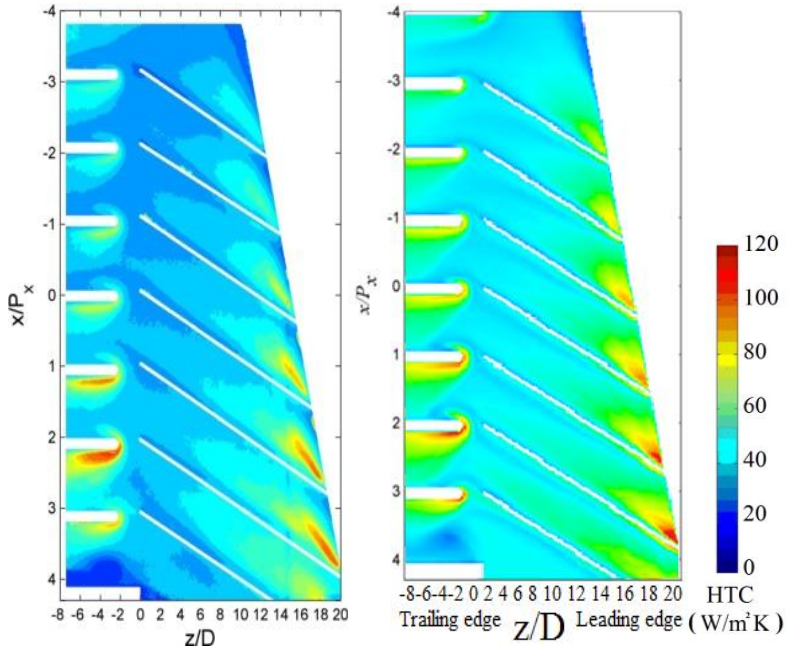

(a) (b)

Figure 6. 16 : 2D maps of HTC [W/m^2 K], surface Ribs +60°, open tip, Re= 20000, Ro=0: a) Experimental, b) Numerical prediction.

The high radial velocity acquired by the air increases the angle of attack on the pedestals, thus reducing of the augmentation of heat transfer along the suction side. In the same time it is incrementing the size of the separation bubble over the suction side, where a horse shoe vortex is bended towards the suction side. The other observation is the fact that the recirculation bubble in the first inter-pedestal zone increases in size. Furthermore the augmented heat transfer coefficient zone on the leading edge of the pedestals is extended inside L0 region.

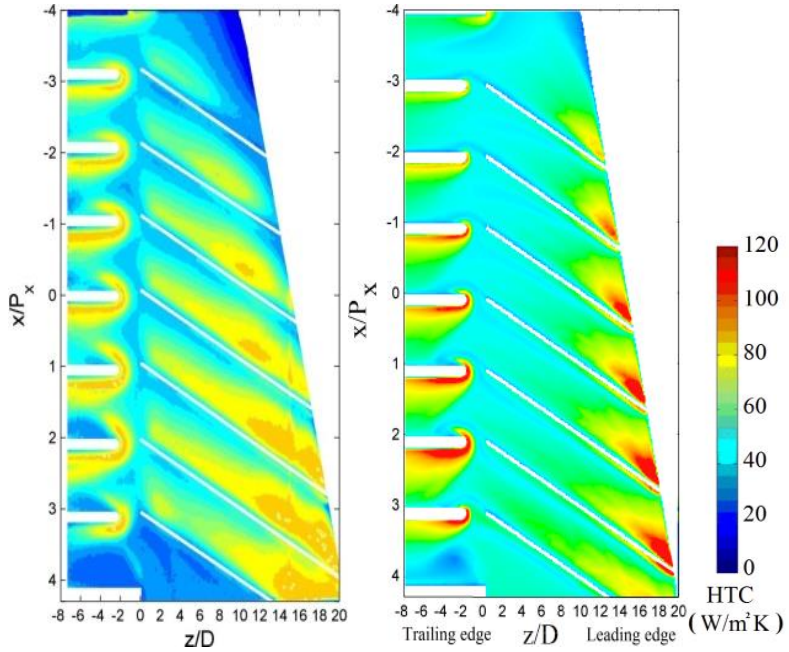

Figure 6. 17 : 2D maps of HTC [W/m^2 K], Open tip, Re= 20000, Ro=0.15:
a) Experimental, b) Numerical prediction.

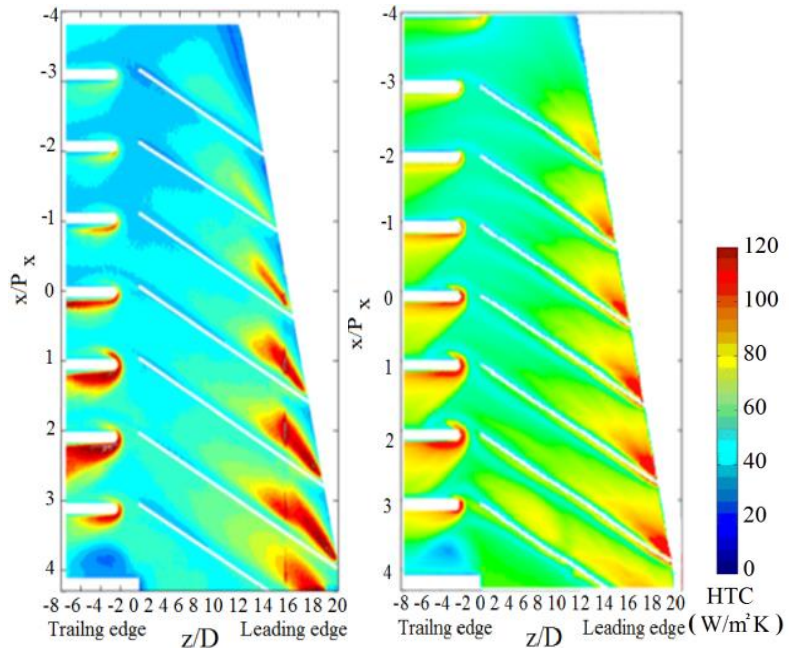

Figure 6. 18 : 2D maps of HTC [W/m^2 K], surface Ribs +60°, Open tip, Re= 40000, Ro=0: a) Experimental, b) Numerical prediction.

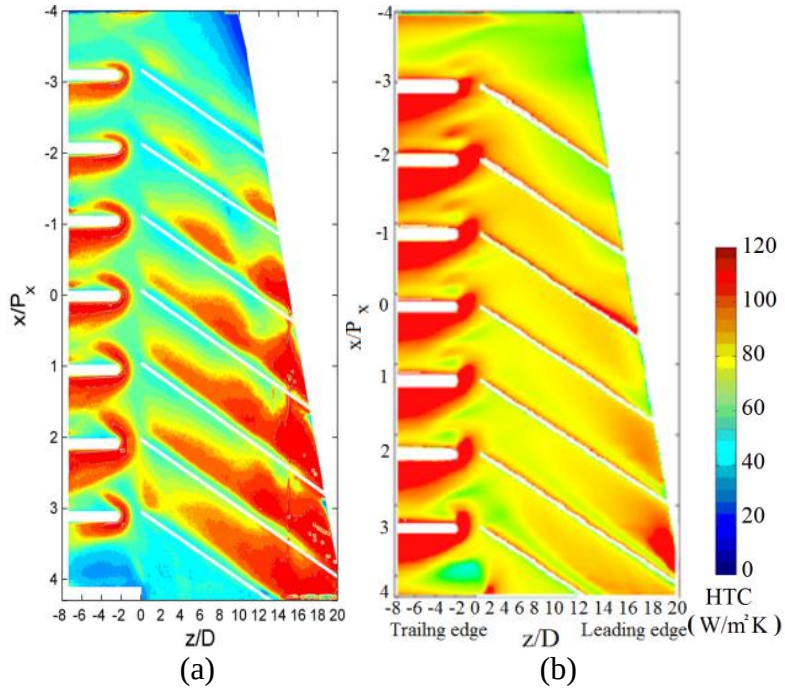

Figure 6. 19 : 2D maps of HTC [W/m^2 K], surface Ribs +60°, Open tip, Re= 40000, Ro=0.15: a) Experimental, b) Numerical prediction.

6.3.3 Averaged Nusselt number distribution at the L1 region

To better quantify the agreement between the experiments and the CFD prediction figures (6.20 and 6.21) present both the experimental and numerical results for the averaged Nusselt number in the inter-pedestal vanes for the smooth and +60° ribs surface, at Ro= 0, for Re= 20000 and Re= 40000. As seen the numerical results are close to experimental results within into account the uncertainty of ±17%. Along the blade height the averaged Nusselt value is shown to decrease which is in accordance with the obtained HTC distribution.

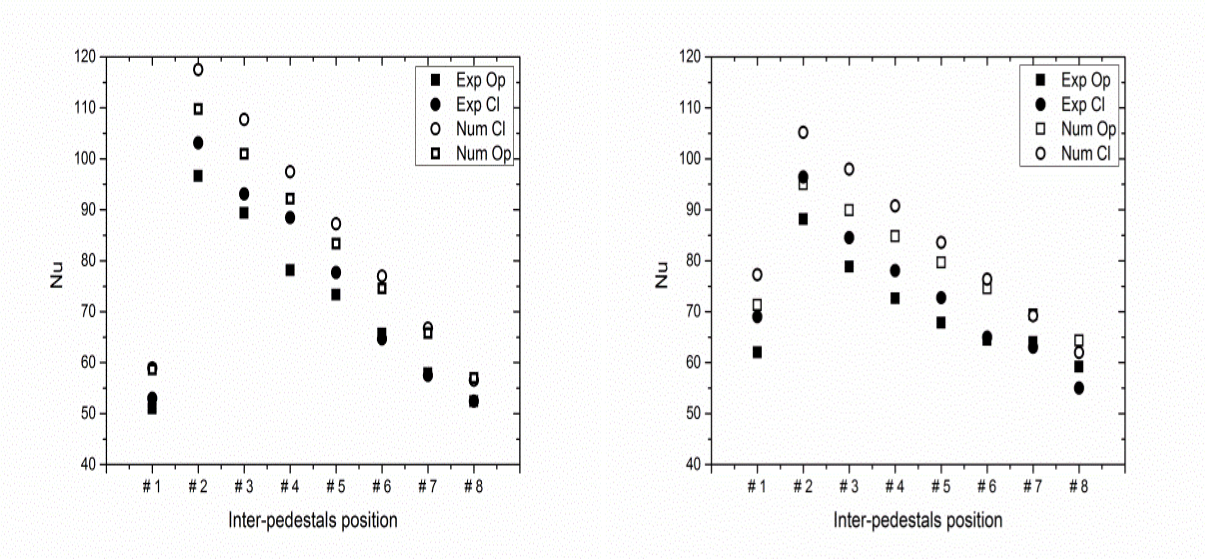

(a) (b)

Figure 6. 20 : Averaged Nusselt number variation at Re = 20000, Ro=0, Closed tip a) Smooth, b) Ribs +60 °

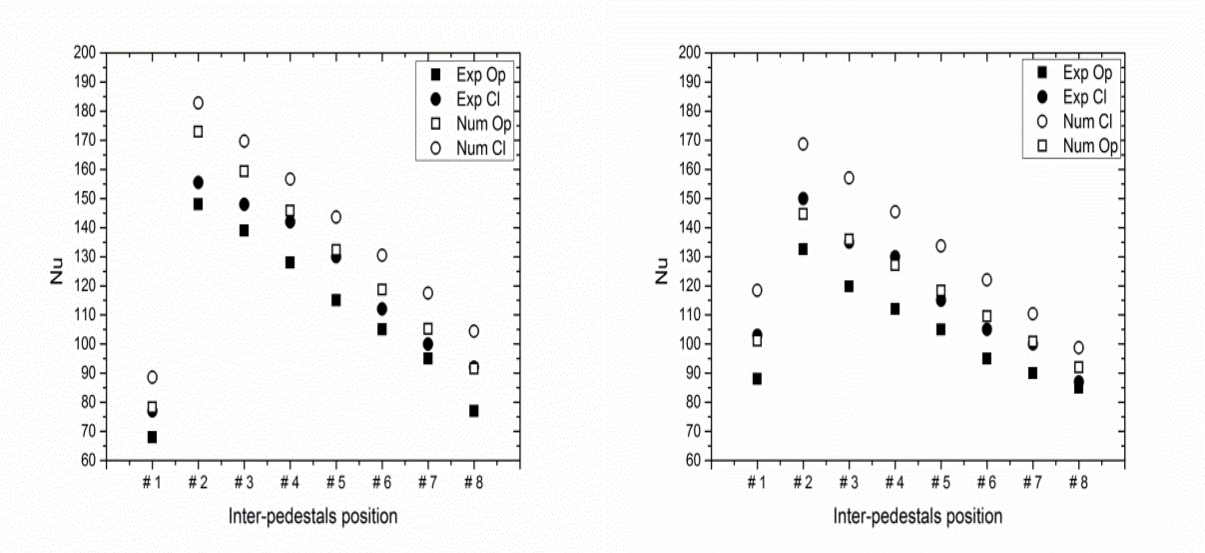

(a) (b)

Figure 6. 21 : Averaged Nusselt number variation at Re = 40000 Ro=0, Open Tip, a) Smooth surface , b) Surface Ribs +60 °

The averaged Nusselt number results show that the smooth surface has a better cooling compared to +60° ribs surface (Figures 6.20 and 6.21). This can be explained by the position of ribs which might affect the orientation of the flow towards the pedestals region [21]. However, L0 region of the surface Ribs +60° has higher HTC values than smooth surface at L0 region which is in accordance with the known results in literature. [25]

The increase in Reynolds number from 20000 to 40000 leads to an increase in HTC, due to the fact that more fresh coolant is passing through the inter-pedestal vanes. The closed tip produces a high averaged Nusselt number as compared to the open tip case as a more air flow rate exits from the trailing edge but this remark is not respected for inter-pedestal region # 8 which has a lower averaged Nusselt number for a closed tip as compared to open tip, which may be explained by the effect of the recirculation zone at tip on the coolant crossing the inter-pedestal region # 8. In fact, by reaching the recirculation zone at the tip region, the main coolant stream is redirected first by the inclined wall and secondly by the recirculation zone towards the exit of trailing edge. The distribution of velocity vectors at the y = 0 plan is shown on figure 6.22, highlights the interaction between the coolant main stream and the recirculation zone, thus leading to a rise in the coolant temperature before reaching the inter-pedestal region # 8. As consequence, the cooling efficiency is reduced at this region as compared to the open tip, because there is no recirculation zone near the tip.

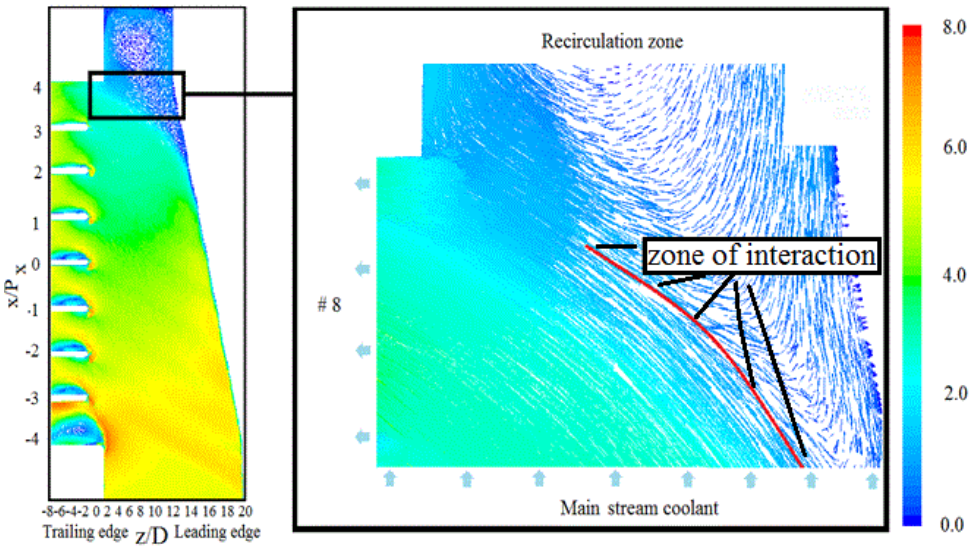

Figure 6. 22 : 2D maps of HTC [W/m^2 K]; interaction between the main stream flow and recirculation zone, *xz plane (y=0),* Surface Ribs +60°, closed tip, Re=20000, Ro=0.

The effect of the tip condition when the Re and Ro increase is illustrated by comparing the results of open tip to closed tip. Practically, the averaged Nusselt number values for the stationary conditions increase with the increase of Reynolds number as noticed by comparing Re= 20000 and Re =40000, for the same working conditions of Ro and Pr.

To compare the effect of increasing the Reynolds number combined to the rotation number, the ratio of the Nusselt number for rotation to the Nusselt number at stationary condition , for both Re=40000 to Re= 20000, is defined as:

$$Nu\ ratio = \frac{Nu/Nu_{st}\,]_{(Re=40000)}}{Nu/Nu_{st}\,]_{(Re=20000)}} \tag{7.3}$$

Figure 6.23 shows that the increase of the rotation number leads to changing the $Nu\ ratio$ for the Re= 40000 by the same amount for the Re= 20000. By concluding, a good agreement between numerical results and those obtained experimentally is found.

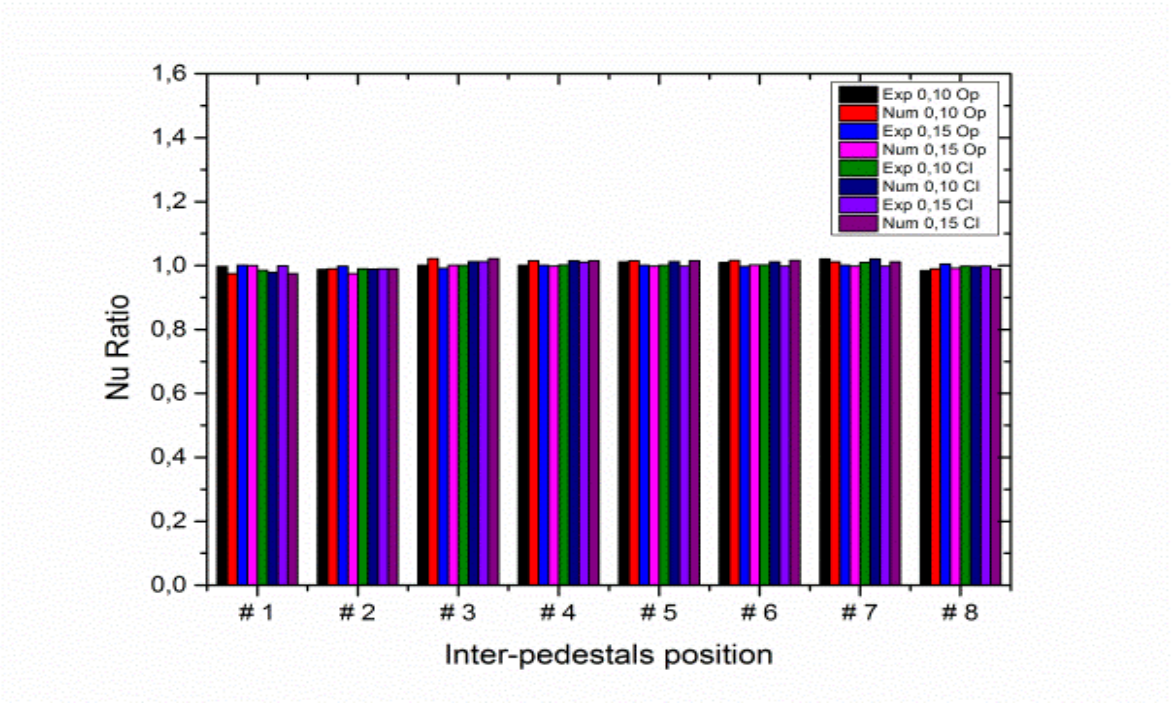

(a)

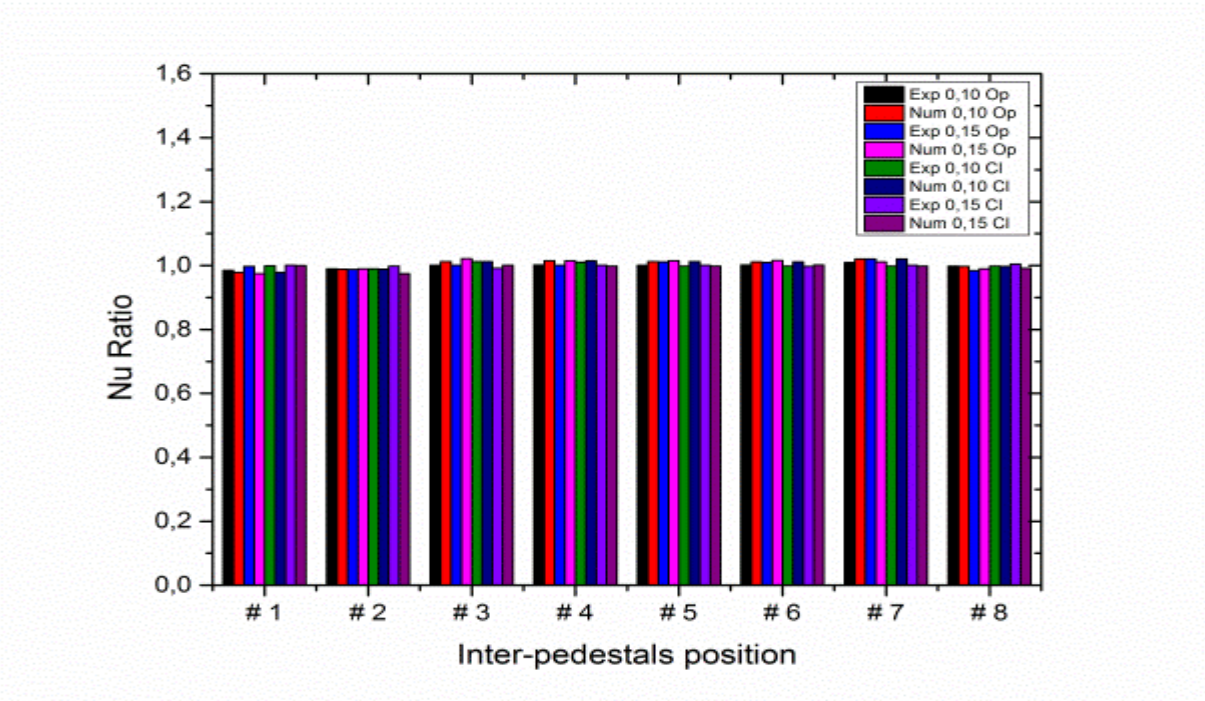

(b)

Figure 6. 23: Nu ratio variation (a) Smooth surface (b) Surface Ribs +60 °

Conclusion

In the present work, the experimental and the numerical investigations were conducted to study the heat transfer in innovative cooling system consisting of a wedge shaped duct with seven pedestals to drive the flow towards the trailing edge. The steady-state technique consisting in a thick heating sheet and wide band TLC under stationary and rotating conditions. Two different blowing conditions were studied: closed and open tip. An analysis at Reynolds number 20000 and 40000 includes the effects of the rotation up to up to *0.23* for two surface configurations: smooth surface and Ribs +60° surface.

The obtained results are presented firstly in terms of global HTC 2D distribution on the heated wall, along four lines located in the trailing edge region and secondly in terms of averaged Nusselt number of the L1 region. It was noticed that the ribs +60° surface has a lower cooling compared to smooth surface at L1 region due to ribs turbulence enhancement at the L0 region. In fact, the turbulence enhancement of the cooling air at the L0 region due to the existing of ribs leads to reduce its efficiency at the L1 region by reducing the film temperature. On other hand, ribs induce a better distribution and efficiency of the cooling over the heated surface. A further study of this difference can be advised in the next works.

Concerning the effect of rotation, it has been sighted that this later has several effects on HTC distributions. In the *L0* region, the intensification of the rotation speed promotes the averaged HTC value near the hub, and at the same time, it moves the center of region of the low HTC located near the tip towards the lower radii. In the *L1* region, for both blowing conditions the increase in *Ro* showed a change in HTC peaks value on the pedestals leading edges due to variation in the coolant incidence angle on pedestals. The same amount of increase of HTC peaks value is remarked at different Reynolds numbers when the rotation number increases.

The comparison of the numerical and experimental for the heat transfer results has confirmed that CFD is able of reproducing the HTC distributions on the heated wall with a reasonable accuracy but the over- estimations does not exceed 17%.

General Conclusions

Nowadays, the improvements in the design of aero-engines or gas turbines are principally motivated by the requisite of high specific thrust/power ratio. The advancement of the turbine blade cooling effectiveness is of great interest to achieve a high thermal cycle efficiency by developing new designs of rotating cooling channels and getting an in-depth knowledge of their complex flow structures. An experimental approach is always the first step to well understand the physical phenomenon besides a validating numerical approache. For that reason, this works was aimed to investigate the heat transfer in the trailing edge cooling device using enlarged pedestals, under both static and rotating conditions. In fact, this work is a continuity to that carried out by Bonnani [21] from the University of Florence, Italy.

The heat transfer of a turbine blade trailing edge characterized by a radial-axial discharge coolant device, and under effects of rotation and tip outflow conditions were evaluated experimentally using the non-intrusive TLC technique and predicted numerically by means of ANSYS-Fluent solver. The results relative to the suction side surface are reported in terms of 2D maps of HTC distributions and its spanwise profiles. The performance of three configurations (flat plate, ribs + 60° and ribs – 60°) to the coolant discharge conditions: The closed tip outlet presents only an axial discharge, whereas for the open tip with approximately 12.5% of inlet flow discharged radially from the tip outlet. The main conclusions are enumerated as following:

1- Experimental results are reported in terms of detailed 2D maps of HTC over the suction side as well as the averaged Nusselt number evaluated inside the pedestal ducts
2- For the flow field, some features have been noticed, especially the existence of recirculation zones, one near the hub at region # 1, for two both closed tip and open tip, but the other near the tip occurs only for the closed tip. These recirculation zones affect the distribution and the efficiency of the coolant. In fact, 2D maps of HTC show a better distribution of coolant over the L0 heated surface for the case of open tip.
3- The HTC distribution is strongly affected by the surface configuration. In the case of Ribs +60° surface there is a better distribution of HTC at the L0 region than for the other surfaces, which might be explained by the ribs positions and the turbulence effect.

4- The effect of increasing of Re from 10000 to 40000 leads to improving the HTC values for all studied configurations at the same rotation conditions. This conclusion is also supported by the work of Bonnani. [21]

5- Another parameter which has been taken into account in evaluating the cooling efficiency over all studied surfaces, which is the Rotation number of values of 0,0.1,0.15 and 0.23.

6- The obtained experimental data show a clear dependency between the Ro number and the HTC distribution. In fact, due to the high rotation number the centrifugal force displaces radially the coolant fluid, and the Coriolis force induces an axial acceleration to the fluid towards the trailing edge. This combined effect extend the low HTC region near the redirecting wall and produces a global axialization of the flow and leads to the change in the HTC values and by the way of the averaged Nusselt number.

7- A comparison between the Nusselt ratio shows that the increase of the Re does not affect significantly the averaged Nusselt ratio. Practically, we have the same variation of the Nusselt number for a fixed Rotation number compared to the stationary conditions.

8- A contribution to correlate the averaged Nusselt number at the trailing edge exit region based on two correlations for the three studied cooling surfaces and use only different tip conditions: The first one correlation is an exponent function based on the Reynolds number. In the second one, a complex exponent form is chosen to take into account the effect of Prandtl number, Rosby number and the fraction of the blade height. The obtained correlations produced a good fitting with the experimental data.

9- A numerical investigation was also carried out to predict the heat transfer phenomenon inside the innovative cooling scheme of the trailing edge. The CFD analyses used the steady-state RANS ANSYS-Fluent solver based on the kω-SST turbulence model and the isothermal steady air- flow. Calculations were validated against PIV measurements for Re = 20000 at stationary and rotating conditions (Ro= 0.23). The aerothermal results are comparable with the experimental data at the Reynolds number = $\{20000, 30000\ and\ 40000\}$ and the Rosby number in the range from 0 to 0.15. Generally speaking, there is a good agreement between the experimental and numerical data in terms of HTC distributions and the averaged Nusselt number with about 17% in accuracy. These predicted aero-thermodynamic fields helps to better visualize the flow behavior and assess the cooling performance of the turbine trailing edge wedge.

Finally this contribution is only a step to better understand the heat transfer of internal cooling systems of the central region of a trailing edge. To further improve our knowledge of the following points should be advanced in a next work:

1- Estimate the mass flow rate at each slot of inter-pedestals region in order to better estimate the Reynolds number.
2- Study the effect of inclination of the studied geometry for stationary and rotation conditions. Inclination angle must be the one used in practice with angles in between 30° and 60 *deg*.
3- Reach higher Reynolds number and Rosby number. In fact, the actual test rig is limited to Ro= 0.23 when Reynolds number is more than 25000. Reducing the test model dimensions and using other recording camera that may resolve the limited Rosby number of the actual test rig.
4- Study the heat transfer inside the innovative scheme cooling system numerically but taking into account the heat losses at PMMA faces instead of isothermal conditions.
5- Considering real gas conditions in the numerical simulation to estimate the variety of the obtained correlation in real gas turbines operation.

List of references

[1] T. Hawksley, Lecture. Adressed by Captain H. Riall Sankey on Heat Engines to the Institution of Mechanical Engineersin November 1917.

[2] Hunt R. J., The History of the Industrial Gas Turbine - Part 1: The First Fifty Years 1940-1990, idgtE, The Institution of Diesel and Gas Turbine Engineers, Bedford Heights, Manton Lane, Bedford MK41 7PH, publication: 582, 2011.

[3] J. C. Han., S. Dutta. and S. V. Ekkad., 2000, Gas turbine heat transfer and cooling technologies. Taylor & Francis, ISBN 156032841X, New York , NY 10001.

[4] J. E. Hart, "Instability and secondary motion in a rotating channel flow," Journal of Fluid Mechanics, vol. 45, pp. 341–351, 1970.

[5] C. G. Speziale, "Numerical study of viscous flow in rotating rectangular ducts," Journal of Fluid Mechanics, vol. 122, pp. 251– 271, 1982.

[6] C. G. Speziale and S. Thangam, "Numerical study of secondary flows and roll-cell instabilities in rotating channel flow," Journal of Fluid Mechanics, vol. 130, pp. 377–395, 1983.

[7] J.P. Johnston, R.M. Halleen, and D.K. Lezius, 1972. Effects of spanwise rotation on the structure of two dimensional fully developed turbulent channel flow, J. Fluid Mech., Vol. 56, pp. 533-557.

[8] D. K. Lezius and J. P. Johnston, 1976, Roll-cell instabilities in rotating laminar and turbulent channel flows. Journal of Fluid Mechanics, vol 77, pp:153 – 175.

[9] E. Metzger, S. W. Haley, 1982, Heat transfer experiments and flow visualization for arrays of short pin fins, ASME Paper 82GT138.

[10] E. Metzger, R. A Berry, and J. P. Bronson., 1982, Developing heat transfer in rectangular ducts with staggered arrays of short pin fins. ASME journal of Heat Transfer, pp 104(1):700706.

[11] E. Metzger, W. B. Shepard, and S. W. Haley, 1986, Row resolved heat transfer variations in pinfin arrays including effects of nonuniform arrays and flow convergence. ASME Paper, 86GT132.

[12] Z. Wang,. Ireland. P. T, and Jones. T. V, 1993, Detailed heat transfer coefficient measurements and thermal analysis at engine conditions of a pedestal with fillet radii. ASME Paper GT1993329.

[13] Z. Wang., T. V. Jones., Ireland. P. T, and Kohler. S. T, 1994, Measurements of local heat transfer coefficient over the full surface of a bank of pedestals with fillet radii. ASME Paper GT1994307 .

[14] M. E. Taslim and T. Li, 1998, "Measurements of heat transfer coef- ficients in rib-roughened trailing-edge cavities with crossover jets," ASME Paper 98GT-435,

[15] M. E. Taslim and A. Nongsaeng, 2011. “Experimental and numerical cross-over jet impingement in an airfoil trailing-edge cooling channel,” Journal of Turbomachinery, vol. 133, no. 4, Article ID 041009.

[16] J. J. Hwang. and C. C. Lui, 1999, Detailed heat transfer characteristic comparison in straight and 90deg turned trapezoidal ducts with pinfin arrays. International Journal of Heat and Mass Transfer, Vol: 42, pp: 4005–4016.

[17] J. J. Hwang. and C. C. Lui, 2002, Measurements of endwall heat transfer and pressure drop in a pinfin wedge duct. International Journal of Heat and Mass Transfer, Vol:45, pp:877–889.

[18] B. Facchini., C. Carcasci, and L. Innocenti., 2003, Heat transfer and pressure drop evaluation in thin wedge shaped trailing edge. ASME Paper GT200338197.

[19] S. W. Chang, T.-M. Liu, S. F. Chiou, and S. F. Chang, 2007,“High rotation number heat transfer of rotating trapezoidal duct with 45-deg staggered ribs and bleeds from apical side wall,” in Proceedings of the ASME Turbo Expo, pp. 909–921, Montreal, Canada.

[20] A. P. Rallabandi, Y.-H. Liu, and J.-C. Han, 2010, “Heat transfer in trailing edge wedge-shaped pin-fin channels with slot ejection under high rotation numbers,” in Proceedings of the ASME Turbo Expo, pp: 369–380, Glasgow, UK.

[21] N. Kulasekharan and B. Prasad. 2008, Effect of coolant entry orientation on flow and heat transfer in the trailing region channels of a gas turbine vane. Proceedings of ASME Turbo Expo 2008: Power for Land, Sea and Air, ASME Paper GT2008-50951.

[22] C. Bianchini, L. Bonanni, C. Carcasci, B. Facchini, and L. Tarchi. 2010, “Experimental survey on heat transfer in an internal channel of a trailing edge cooling system”. 65 Associazione Termotecnica Italiana National Congress.

[23] C. Bianchini, B. Facchini, F. Simonetti, L. Tarchi, and S. Zecchi. 2010, Numerical and experimental investigation of turning flow effects on innovative pin fin arrangements for trailing edge cooling configurations. In Proceedings of ASME Turbo Expo 2010: Power for Land, Sea and Air, ASME Paper GT2010-23536.

[24] L. Bonnani, C. Carcasci, B. Facchini, and L. Tarchi. 2012, “Experimental survey on heat transfer in a trailing edge cooling System: effects of rotation in internal cooling ducts”. ASME Paper GT2012-69638.

[25] H. Wu, Liu Y, Xu G, 2013, “Measurements of heat transfer and pressure in a trailing edge cavity of a turbine blade’. Chinese Journal of Aeronautics”, Vol: 26(2), pp: 294–308.

[26] F. Coletti,1, D. Lo Jacono, I. Cresci, and T. Arts1, 2014, Turbulent flow in rib-roughened channel under the effect of Coriolis and rotational buoyancy forces, Journal of PHYSICS OF FLUIDS, Vol: 26, 045111.

[27] E. E. Donahoo, A. K. Kulkarni, A. D. Belegundu, and C. Camci. 2001, Determination of optimal row spacing for a staggered cross-pin array in a turbine blade cooling passage. Journal of Enhanced Heat Transfer, Vol: 8, pp: 41–53.

[28] L. J. Hamilton, D. S. Adametz, E. K. Lind, and A. Gropinath. 2002, Numerical analysis of the performance of a staggered cross-pin array heat exchanger. 8th AIAA/ASME Joint thermophysics and Heat Transfer Conference,.

[29] A. Ooi, G. Iaccarino, P. A. Durbin, and M. Behnia, 2002, "Reynolds averaged simulation of flow and heat transfer in ribbed ducts," International Journal of Heat and Fluid Flow, Vol. 23(6), pp. 750–757.

[30] M. Loh`asz, P. Rambaud, and C. Benocci, 2003, "LES simulation of ribbed square duct flow with fluent and comparison with PIV data," in Proceedings of the the 12th International Conference on Modelling Fluid Flow, Fluid Flow Technologies, Budapest, Hungary.

[31] D. D. Luo, C. W. Leung, T. L. Chan, and W. O. Wong, 2005, "Simulation of turbulent flow and forced convection in a triangular duct with internal ribbed surfaces," Numerical Heat Transfer A, Vol. 48(5), pp. 447–459.

[32] A. K. Viswanathan and D. K. Tafti, 2006, "Detached eddy simulation of turbulent flow and heat transfer in a two-pass internal cooling duct," International Journal of Heat and Fluid Flow, vol. 27, no. 1, pp. 1–20,.

[33] S. Spring, Y. Xing, and B. Weigand, 2012, "An experimental and numerical study of heat transfer from arrays of impinging jets with surface ribs,"Journal of Heat Transfer, vol.134 , no.8 , Article ID 082201.

[34] A. K. Saha and S. Acharya, 2007 ,"Turbulent heat transfer in ribbed coolant passages of different aspect ratios: parametric effects," Journal of Heat Transfer, vol. 129, no. 4, pp. 449–463.

[35] P. D'Agaro and G. Comini. 2008, Thermal-performance evaluation of coolant passages with staggered arrays of pin fins. International journal of Heat and Mass Transfer, Vol: 44, pp: 815–825.

[36] G. Delibra, D. Borello, K. Hanjalic, and F. Rispoli. 2009, URANS of flow and endwall heat transfer in a pinned passage relevant to gas-turbine blade cooling. International Journal of Heat and Mass Transfer, Vol: 30, pp: 549–560.

[37] E. Di Carmine, B. Facchini, and L. Mangani. 2008, Investigation of innovative trailing edge cooling configurations with enlarged pedestals and square or semi-circular ribs. Part II - numerical results. Proceedings of ASME Turbo Expo 2008: Power for Land, Sea and Air, ASME Paper GT2008-51048.

[38] C. Prakash and R. Zerkle. 1992, Prediction of turbulent flow and heat transfer in a radially rotating square duct. Journal of Turbomachinery, Vol: 114.

[39] H. Iacovides, D. C. Jackson, G. Kelemenis, B. E. Launder, and Y. M. Yuan. 2001, Flow and heat transfer in a rotating u-bend with 45° ribs. International Journal of Heat and Fluid Flow, Vol: 22, pp: 308–314.

[40] M. Schuler, H. Dreher, S. O. Neumann, B.Weigand, and M. Elfert. 2010, Numerical predictions of the effect of rotation on fluid flow and heat transfer in an engine-similar two-pass internal cooling channel with smooth and ribbed walls. In Proceedings of ASME Turbo Expo 2010: Power for Land, Sea and Air, ASME Paper GT2010-22870.

[41] C. Prakash and R. Zerkle. 1995, Prediction of turbulent flow and heat transfer in a ribbed rectangular duct with and without rotation. Journal of Turbomachinery, Vol: 117.

[42] K. Tafti and A. M. Elyyan. 2010, Investigation of Coriolis forces effect of flow structure and heat transfer distribution in a rotating dimpled channel. Proceedings of ASME Turbo Expo 2010: Power for Land, Sea and Air, ASME Paper GT2010-22657.

[43] F. Coletti, M. Scialanga, and T. Arts, 2011, "Experimental investigation of conjugate heat transfer in a rib-roughened trailing edge channel with crossing jets," Journal of Turbomachinery, Vol. 134(4), Article ID 041016.

[44] A. Armellini, F. Coletti, T. Arts, and C. Scholtes, 2010 ,"Aerothermal investigation of a Rib-Roughened trailing edge channel with crossing-Jets—part I: flow field analysis," Journal of Turbomachinery, Vol. 132(1), Article ID 011009.

[45] A. Armellini, L. Casarsa, and C. Mucignat, 2011, "Flow field analysis inside a gas turbine trailing edge cooling channel under static and rotating conditions," International Journal ofHeat and Fluid Flow, Vol: 32(6), pp: 1147–1159.

[46] H. Iacovides, D. Kounadis, B. E. Launder, J. Li, and Z. Xu, 2005 , "Experimental study of the flow and thermal development of a row cooling jets impinging on a rotating concave surface," Journal of Turbomachinery, vol. 127, no. 1, pp. 222–229.

[47] M. Elfert, M. Schroll, and W. F¨orster, 2010, "PIV-measurement of secondary flow in a rotating two-pass cooling system with an improved sequencer technique," in Proceedings of the ASME Turbo Expo, pp. 555–567, Glasgow, UK.

[48] A. K. Saha and S. Acharya, 2005, "Unsteady RANS simulation of turbulent flow and heat transfer in ribbed coolant passages of different aspect ratios," International Journal of Heat and Mass Transfer, Vol. 48(23-24), pp. 4704–4725.

[49] J. Pallares and L. Davidson, 2000, "Large-eddy simulations of turbulent flow in a rotating square duct," Physics of Fluids, Vol: 12(11).

[50] F. N. Felten and G. M. Laskowski, 2007, "Large eddy simulations of fully developed flow through a spanwise rotating infinite serpentine passage," in Proceedings of the ASME Turbo Expo, pp. 397–411.

[51] G. M. Laskowski and P. A. Durbin, 2007, "Direct numerical simulations of turbulent flow through a stationary and rotating infinite serpentine passage," Physics of Fluids, Vol. 19(1), Article ID 015101.

[52] A Andreini, C Bianchini, A Armellini, L Casarsa, 2011, Flow field analysis of a trailing edge internal cooling channel, ASME 2011 Turbo Expo: Turbine Technical Conference and Exposition, pp: 1247-1258.

[53] M. Pascotto, A. Armellini, L. Casarsa, C. Mucignat, and P. Giannattasio, 2013, Effects of Rotation at Different Channel Orientations on the Flow Field inside a Trailing Edge Internal Cooling Channel, International Journal of Rotating Machinery Vol: 2013, Article ID 765142.

[54] H. I. Anderson, 2010 ,"In Introduction on the effects of turbulence, Lecture Series, Von Karman Institute for Fluid Dynamics.

[55] R.Yu, Y.Xu, 2012, "Uncertainty Analyses and Its Application to Turbulent Heat Transfer Measurements", Advances in Condensed Matter Physics Journal, Vol. 2012, Article ID 898104.

[56] F. Maiuolo, B. Facchini, L. Tarchi., and N. Ohlendorf, 2013, "Experimental investigation on the heat transfer in a turbine airfoil leading edge region: Effects of the wedge angle and jet impingement geometries", 10th European Turbomachinery Conference 130-ETC.

[57] F. Maiuolo, B. Facchini, L. Tarchi., and N. Ohlendorf; 2013, "Experimental investigation on the heat transfer of a leading edge cooling system: Effects of jet-to-jet spacing and showerhead extraction. ASME paper, 2013GT94759.

[58] F. Maiuolo, PhD thesis, Experimental Analyses of Gas Turbine Airfoil Leading Edge Cooling Systems, University of Florence, Italy, 2013.

[59] G. Caciolli, A. Andreini, B. Facchini, L. Tarchi, D. Coutandin, A. Peschiulli, and S. Tadei, 2012, "Density ratio effects on the cooling performances of a combustor liner cooled by a combined slot/ effusion system". ASME Paper, 2012GT68263.

[60] ASME, 1985, "Measurement Uncertainty" Instrument and Apparatus, Vol. ANSI/ASME PTC 19.1 of Performance Test Code.

[61] S. J. Kline., and F. A. Mc Clintock., 1953, Describing uncertainties in single sample experiments. Mechanical Engineering, Vol: 75, pp: 3–8.

[62] D. R. H. Gillespie et al, 2000, Detailed flow and heat transfer coefficient measurements in a model of an internal cooling geometry employing orthogonal interesting channels, ASME TurboExpo, May 8-11 Germany, Munich, Germany.

[63] Andrei. L, Andreini. A, Bonanni. L, and Facchini. B, 2010, "Heat transfer in internal channel of a blade: effects of rotation in a trailing edge cooling system", 10th International Symposium on Experimental Computational Aerothermodynamics of Internal Flows, ISAIF paper, pp: 10-99

[64] FOXES TEAM, Tutorial on Numerical Analysis with Optimiz.xla , Optimization, Nonlinear Fitting and Equations Solving, Volume, 2nd Edition, May 2006. pp: 71-72.

[65] M. J. Moran., H. N. Shapiro., Munson. B. R, and D. P. DeWitt., 2002, Introduction to Thermal Systems Engineering : Thermodynamics, Fluid Mechanics, and Heat Transfer, Wiley, John & Sons, Incorporated, edition 1, September 2002, 0471204900, pp:345.

[66] A. Incropera, B. DeWitt, T. Birgman, A. Lavine, 2007, Fundamentals of Heat and Mass transfer, 6th edition, Wiley, London, UK.

[67] Bonnani, 2013, Investigation on a Trailing Edge Cooling System, PhD thesis, University of Florence.

[68] Hallcrest, *Handbook of Thermochromic Liquid Crystal Technology*, 1991.

[69] Y. Rao and S. Zang, "Calibrations and the measurement uncertainty of wide-band liquid crystal thermography," *Measurement Science and Technology*, vol. 21, no. 1, Article ID 015105, 2010.

[70] P. T. Ireland, A. J. Neely, D. R. H. Gillespie, and A. J. Robertson, "Turbulent heat transfer measurements using liquid crystals," International Journal of Heat and Fluid Flow, vol. 20, no. 4, pp. 355–367, 1999.

[71] P. T. Ireland and T. V. Jones, "Liquid crystal measurements of heat transfer and surface shear stress," Measurement Science and Technology, vol. 11, no. 7, pp. 969–986, 2000.

[72] C. Camci, K. Kim, and S. A. Hippensteele, "A new hue capturing technique for the quantitative interpretation of liquid crystal images used in convective heat transfer studies," Journal of Turbomachinery, vol. 114, no. 4, pp. 765–775, 1992.

[73] D. J. Farina, J. M. Hacker,R. J.Moffat, and J. K. Eaton, "Illuminant invariant calibration of thermochromic liquid crystals," Experimental Thermal and Fluid Science, vol. 9, no. 1, pp. 1–12, 1994.

[74] M. Behle, K. Schulz, W. Leiner, and M. Fiebig, "Color-based image processing to measure local temperature distributions by wide-band liquid crystal thermography," Applied Scientific Research, vol. 56, no. 2-3, pp. 113–143, 1996.

[75] D. R. Sabatino, T. J. Praisner, and C. R. Smith, "A high-accuracy calibration technique for thermochromic liquid crystal temperature measurements," Experiments in Fluids, vol. 28, no. 6, pp. 497–505, 2000.

[76] T. L. Chan, S. Ashforth-Frost, and K. Jambunathan, "Calibrating for viewing angle effect during heat transfer measurements on a curved surface," International Journal of Heat and Mass Transfer, vol. 44, no. 12, pp. 2209–2223, 2001.

[77] T. B. Roth and A. M. Anderson, "The effects of film thickness, light polarization, and light intensity on the light transmission characteristics of thermochromic liquid crystals," Journal of Heat Transfer, vol. 129, no. 3, pp. 372–378, 2007.

[78] R.Wiberg and N. Lior, "Errors in thermochromic liquid crystal thermometry," Review of Scientific Instruments, vol. 75, no. 9, pp. 2985–2994, 2004.

[79] N. Abdullah, A. R. A. Talib,H. R.M. Saiah, A. A. Jaafar, and M. A. M. Salleh, "Film thickness effects on calibrations of a narrowband thermochromic liquid crystal," Experimental Thermal and Fluid Science, vol. 33, no. 4, pp. 561–578, 2009.

[80] Y. Rao, S. Zang, and C. Wan, "Effect of coating thickness on the calibration and measurement uncertainty of a wide-band liquid crystal thermography," Chinese Optics Letters, vol. 8, no. 4, pp. 395–397, 2010.

[81] MATLAB 2007 R2007a help document, The MathWorks Inc.

[82] F. MAYINGER, 'SCALLING AND MODELLING LAWS IN TWO PHASE FLOW AND BOILING HEAT TRANSFER', Institut Fur Verfahrebstechnik, Technische Universitat, Hannover, West Germany. http://www.td.mw.tum.de/tum-td/de/forschung/pub/CD_Mayinger/040.pdf

Appendix A:

Errors estimations

For this point, the reference of Kline and McClintock [61] allows the estimation of the HTC uncertainty detail is as follows: All the experimental data derived are measured with devices and sensors that are characterized by their accuracy.

The uncertainty analysis is divided into two parts: •

1. Determination of the uncertainty in direct measurements,
2. Determination of the uncertainty in the results derived from those measurements.

Each direct measurement should be given the related uncertainty interval within which the true value should lie. For example, a certain temperature measurement might be expressed as: T = 330K ±0.5K.

In case of a set of measurements, as in the present work, for the determination of the mass flow rate and the heat transfer coefficient that are derived from direct measurements, the global uncertainty on the indirect result R is a given as function of the independent variables x_1, x_2, x_3, ..., x_n and their uncertainties:

$$R + \Delta R = f(x_1 + \Delta x_1, x_2 + \Delta x_2, \dots, x_n + \Delta x_n) \quad \text{(A.1)}$$

$$\Delta R = \sqrt{\left(\frac{\partial R}{\partial x_1} x_1\right)^2 + \left(\frac{\partial R}{\partial x_2} x_2\right)^2 + \cdots + \left(\frac{\partial R}{\partial x_n} x_n\right)^2} \quad \text{(A.2)}$$

Applying the equation reported above (equ. 1), it is possible to estimate the global uncertainties of the mass flow and heat transfer coefficient measurements. The mass flow rate was measured with an orifice-meter. Therefore, the global uncertainty is given by the combination of the uncertainty in the primary measurement of the relative pressure and temperature. The Global measurement uncertainty was found to be $\varepsilon_m = 2 - 4\%$.

As regards the heat transfer coefficient, the global uncertainty ΔHTC can be expressed as:

$$\Delta HTC_{(i,j)} = f(\Delta \dot{q}, \Delta \dot{q}_{loss}, \Delta T_w, \Delta T_{room})_{(i;j)} \quad \text{(A.3)}$$

By applying equ. A.2 to the ΔHTC, the obtained results of the ratio $\Delta HTC_{(i,j)}/HTC$ are presented in figure A.2 below highlighting the fact that the ratio $\Delta HTC_{(i,j)}/HTC$ is about 10% for the

studied case. This procedure is repeated for all the studied cases, and the obtained results of the ratio $\Delta HTC_{(i,j)}/HTC$ are in between 8% to 12%.

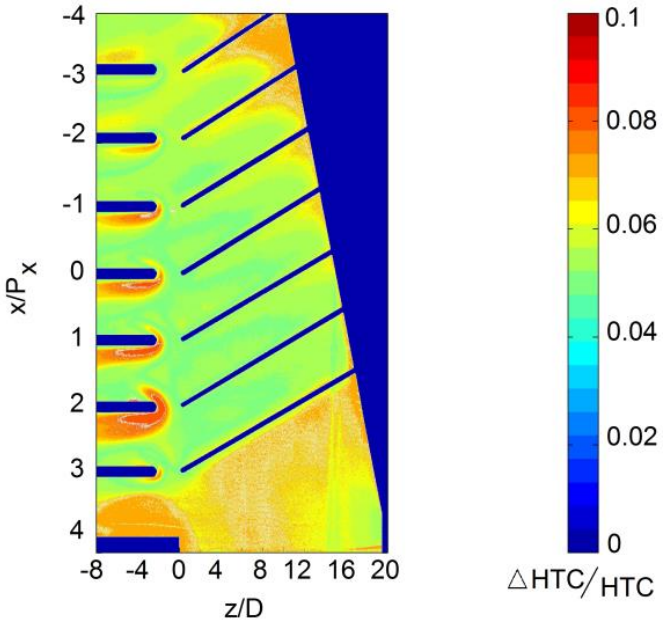

Figure A. 2 : **ΔHTC/HTC** variation, Re=20000, Closed tip, Ribs +60°.

Appendix B [55]

1. Introduction:

Thermochromic liquid crystal (TLC) is a cholesteric liquid crystal material. The cholesteric materials form a similar structure; however, under different temperatures the orientations of adjacent liquid crystal molecule planes are different with certain angles, which results in the reflection of different wavelengths of the visible spectrumof light when illuminated with white light and then show different colors [68–70]. Such optical characteristics of the TLC depend on its temperature and are repeatable and reversible. The accurate relations between the TLC colors and temperatures can be built through careful calibration experiments, which then can be used for precise temperature measurements of any surface.

Currently, the TLC can be provided with the operating temperature between −30°C and 150°C. The TLC may have the bandwidth (the active temperature range) of 1°C to 20°C, in which the liquid crystal can be applied for the temperature measurements by changing color: smoothly fromred to blue. The response time of TLC is about 3 ms [70]. Pure TLC materials are organic compounds that can easily degrade when exposed to chemical contamination and to ultraviolet (UV) light. Currently, people can use microencapsulation process to reduce the degradation. The microsized TLC particles are microencapsulated within transparent polymer shells (PMMA), which can significantly improve the stability of liquid crystal materials and make them capable of being handled easily. The TLC materials are currently supplied by the Hallcrest Ltd. (Glenview, USA) and Merck Ltd. (Pool, UK).

TLC thermography, as a powerful nonintrusive optical technique for temperature measurement, is capable of providing a high-accuracy continuous temperature field measurement, especially for a complex structured heat transfer surface [69, 71]. However, before the TLC is used for the temperature measurement, the hue-temperature calibration must be conducted. In the past two decades, many studies have been conducted on the calibration methods of the TLC. Rao and Zang [69], Camci et al. [72], Farina et al. [73], Behle et al. [74], Sabatino et al. [75], and Chan et al. [76] studied experimentally the effects of the lighting angles and viewing angles on the hue-temperature calibration curves of the TLCs. Roth and Anderson [77], Wiberg and Lior [78], Abdullah et al. [79], and Rao et al. [80] studied experimentally the effects of the coating thickness on the TLC hue-temperature calibration curves. These previous researches only indicated that the lighting angle and the coating thickness can significantly affect the TLC hue-temperature calibration curves. It should be pointed out that, though previous

studies have indicated that such factors as lighting angles and coating thickness can influence the TLC hue-temperature calibration curves, reports on how the temperature measurement uncertainty of the TLC is influenced by those factors are still quite limited.

In this presentation, the effects of the measurement parameters on the measurement uncertainty of the TLC thermography is discussed.

2. Parametric Analysis on the Measurement Uncertainty of TLC:

There are many factors that can affect the TLC thermography measurement uncertainty, such as the TLC bandwidth, the color imaging processing techniques, the coating thickness, the quality of the TLC coating, and the lighting angle, and so forth. In order to study the effects of those parameters on the measurement uncertainty of the TLC, a calibration experimental apparatus was constructed as is shown in Figure 1. The TLC thermography system consists of a Hitachi (HVD30P) 3CCD RGB camera with a zoom lens, cold lighting source, a data acquisition system, an image acquisition system, and the related data processing software. The calibration device consists of a transparent Plexiglas cover plate, a copper plate with a film heater, and two type K thermocouples (0.5 mm in diameter) with the measurement uncertainty of ±0.1°C.

By adjusting the voltage over the film heater, the copper plate's surface temperature can be controlled precisely and rapidly. The surface of the copper base plate was first painted black paint and then a layer of liquid crystal (10–40 μm in thickness). The supplied microencapsulated TLC slurry (Hallcrest SPN100R40C20W) has an operating temperature range of 40–60°C. The changing color under the varying temperature is recorded by the 3CCD RGB camera. The TLC images are then processed by a self-developed data processing program, and the corresponding TLC hue-temperature relationship can be obtained. With the calibration experimental system, the authors have studied the effects of the influencing parameters on the measurement uncertainty of the TLC. 2.1. Effect of the Bandwidth of TLC on the Measurement Uncertainty. According to the working bandwidth, the TLC can be generally divided into the narrowband TLC and wideband TLC. A narrowband TLC has an active temperature range of 1°C, and a wideband TLC can have an active temperature range of 5°C, 10°C, or 20°C. As the bandwidth of the TLC decreases, the sensitivity of hue to temperature increases, and then the measurement accuracy of the TLC increases. The previous literatures showed that the measurement uncertainty of the narrowband TLCs is about ±0.1°C [79], ±0.1– 0.3°C [74], and ±0.2–0.4°C [75] for the TLCs

with the bandwidth of 5°C and 10°C, respectively. The TLC with the bandwidth of 20°C has the measurement uncertainty of about ±0.4–0.5°C [69].

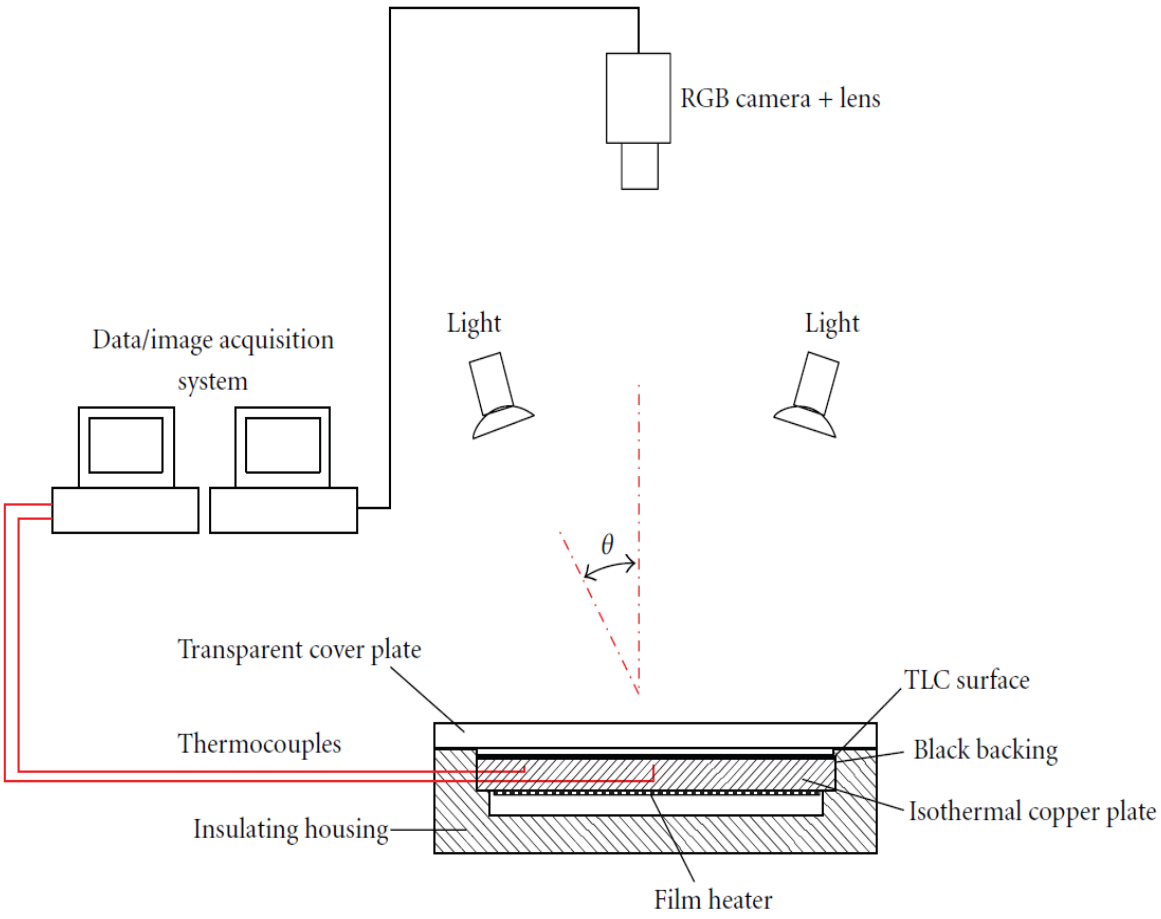

Figure B. 10: The TLC calibration experimental apparatus. [55]

3. Effect of Image Processing on the Measurement Uncertainty.

Figure 1 shows the raw hue and the median filtered hue calibrations of the TLC. The calibration experiment was done with the finely prepared TLC coating with a thickness of 25 μm, and the lighting angle is 27°. The hue value can be calculated by the following algorithms [81].

R, G, and B are, respectively, red, green, and blue components of the liquid crystal image pixel.

$$Hue = tan^{-1}\left[\sqrt{3}(G-B)/(2R-G-B)\right]/2\pi \quad (4.1)$$

$$S = \sqrt{2/3}.\sqrt{R^2+G^2+B^2-RG-GB-RB} \quad (4.2)$$

$$I = \frac{R+G+B}{3} \quad (4.3)$$

It can be seen that the hue curve becomes much smoother than the unfiltered curve. The noise in the hue curves has been effectively removed. To check the reproducibility of the hue curve of the TLC, a second heating process was conducted. Figure 2 shows good reproducibility of the hue curve of the TLC. To estimate the measurement uncertainty of the TLC, the method described in [75] was used. A series of constant temperature TLC color images (100 × 100 pixels) of calibration were examined. The constructed polynomial fitting of the temperature-hue relation was employed to convert each sample image to the corresponding temperature field, and the standard deviation in temperature was determined for each image. Using a 95% confidence interval, the uncertainty for each discrete temperature/image was estimated as twice the standard deviation value. Figure 3 shows the uncertainty in temperature measurement versus the actual temperature measurement. The measurement uncertainty based on the raw hue calibration ranges from 0.1 to 1.6°C with a mean of 0.98°C, and the measurement uncertainty based on the median filtered hue ranges from 0.04 to 0.87°C with a mean of 0.42°C. Therefore, a median filtering technique can significantly improve the measurement accuracy of the TLC. It is also noteworthy that the TLC shows a region-wise measurement uncertainty distribution. Over the temperature range of 41–45°C, due to a higher sensitivity of hue to temperature, the TLC has a higher measurement accuracy, and the median filtered hue calibration has a mean measurement uncertainty of 0.17°C.

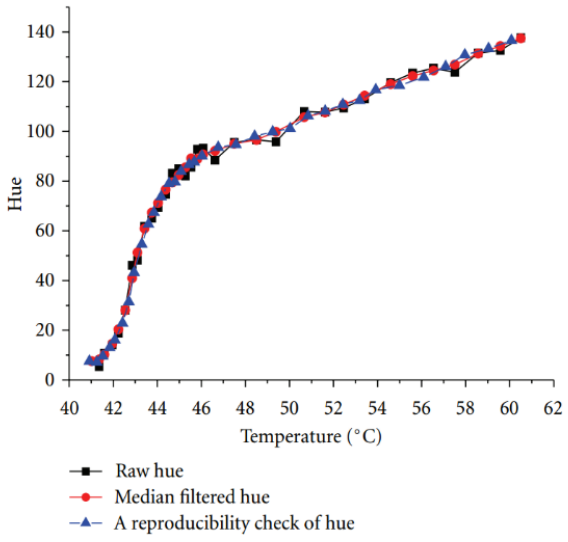

Figure B. 11: The raw hue and the median filtred hue calibrations of the TLC. [55]

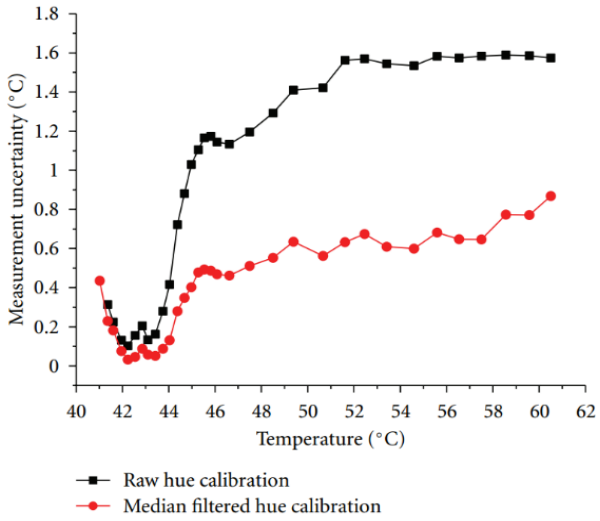

Figure B. 12: The measurement uncertainty in the raw hue and the median filtered hue calibrations. [55]

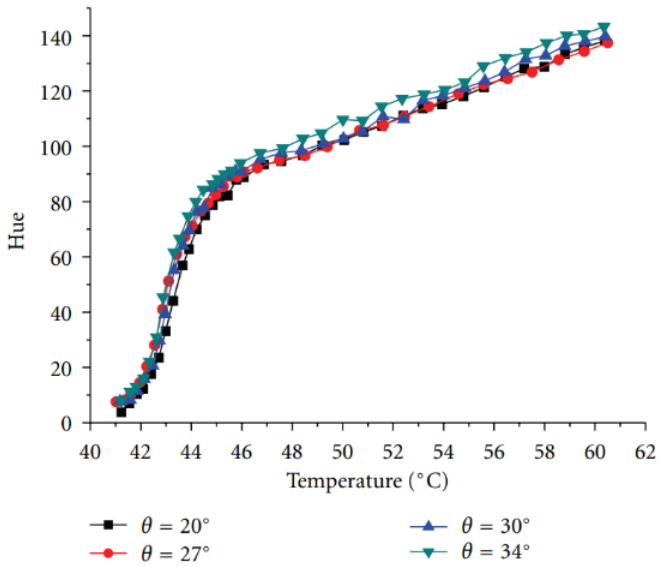

Figure B. 13: Effect of the lighting angle on the curve of the TLC coating.[55]

4. Effect of Lighting Angle on the Measurement Uncertainty

The TLC calibration was conducted at various lighting angles of 20°, 27°, 30°, and 34° with the finely prepared TLC coating based on the calibration experimental system as Figure 1. Figure 4 shows the effect of the lighting angles on the hue calibration. The lighting angle has a notable effect on the hue-temperature curve, and as the lighting angle increases, the hue curve shifts upward. Figure 5 shows the effect of the lighting angles on the uncertainty in temperature measurement versus the actual temperature measurement. It can be found that the measurement

uncertainty increases with the lighting angle. The average measurement uncertainty with the lighting angle of 34° is about 25% higher than that the lighting angle of 20°. The reason should be that as the lighting angle decreases, the lighting intensity on the coating of the TLC is stronger, which leads to a stronger reflection of the color signal and thereby a higher measurement accuracy. The effect of the lighting angle on the measurement uncertainty is more distinctive in the temperature range of 45–60°C, which corresponds to the region of low TLC hue sensitivity. Therefore, in order to get a higher measurement accuracy, the lighting angle should be kept as small as possible providing the experimental space and arrangements allow. Behle et al. [74] studied the effect of lighting angle within the range of 0–70° on the temperature measurement uncertainty of the TLC. They have shown that the measurement uncertainty increases with the lighting angle, and the average measurement uncertainty with the lighting angle of 35° is about 20% higher than that with the lighting angle of 20°, which agrees with the experimental results in the present work.

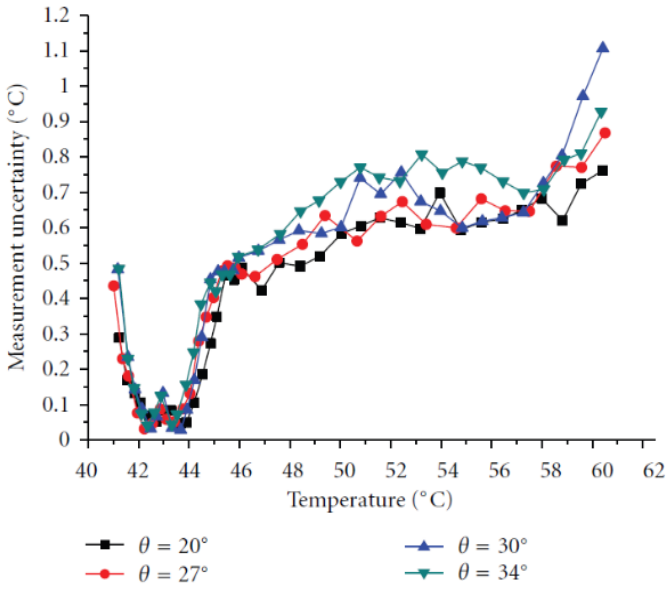

Figure B. 14: Effect of the lighting angle on the measurement uncertainty.[55]

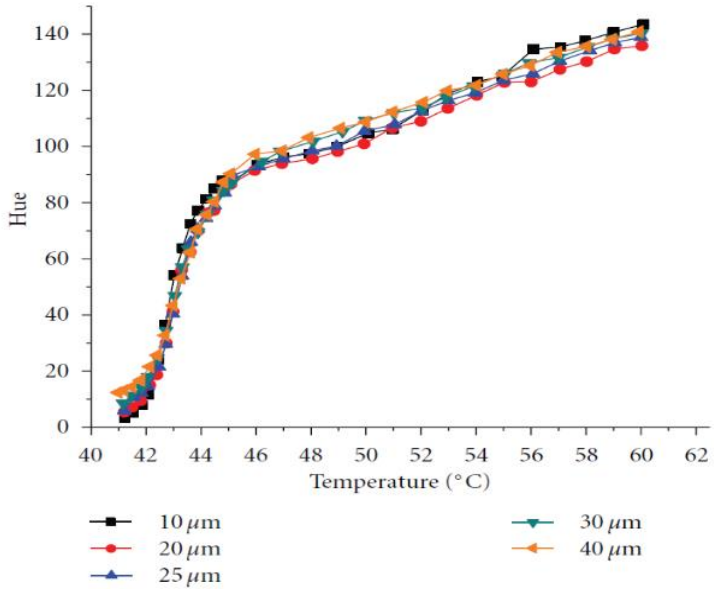

Figure B. 15: Effect of the TLC coating thickness on the curves.[55]

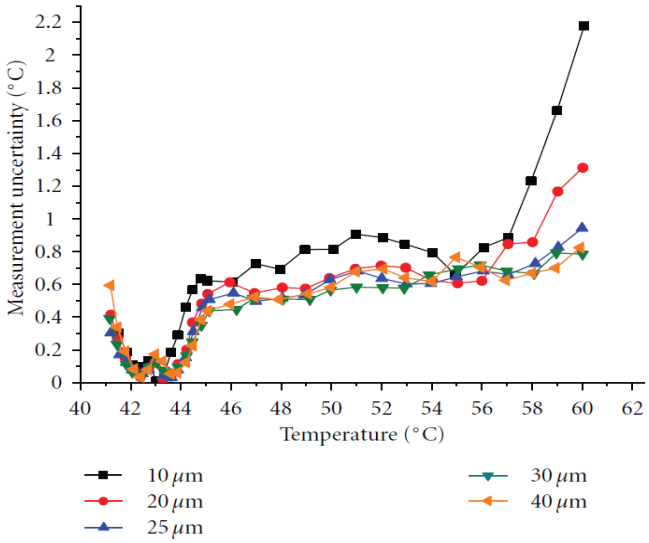

Figure B. 16: Effect of the TLC coating thickness on the measurement uncertainty. [55]

5. Effect of TLC Coating Thickness on the Measurement Uncertainty.

The coating thickness is also an important factor affecting the TLC measurement uncertainty. Figure 6 shows the hue curves of the TLC coatings with different thickness of 10 μm, 20 μm, 25 μm, 30 μm, and 40 μm. The lighting angle is 27°. It can be found that the coating thickness has a notable effect on the hue-temperature curve, and as the coating thickness increases, the hue curve shifts upward.

Figure 7 shows the effect of coating thickness on the measurement uncertainty. It can be found that, except for the TLC coating thickness of 10 μm, the measurement uncertainties of the other TLC coatings show similar values with a mean of about 0.45° C over the calibratable temperature range of 41–60℃, and a thicker TLC coating shows a relatively smaller measurement uncertainty. Figure 7 also indicates that the effect of the TLC coating thickness over 20 μm is non-distinctive on the measurement uncertainty.

The TLC coating with the thickness of 10 μm shows a distinctively higher measurement uncertainty, which is because that the coating is very thin, leading to a weaker reflection of the color signal and correspondingly a higher noise level in the hue.

6. Effect of Coating Quality on the Measurement Uncertainty.

Due to the congregation of the micro-sized TLC particles in the slurry, the suspended congregated particles can be of relatively larger size of 10–20 μm. The TLC coating on the copper surface can be roughly prepared. The TLC coating can also be finely prepared by the following procedures: the TLC slurry was first diluted with an equal amount of distilled water and carefully mixed and fine-filtered; then the TLC slurry was repeatedly sprayed and dried on the black backing on the surface (1–5 μm TLC particle diameters). To examine the effect of the coating quality on the TLC hue curve calibration and the measurement uncertainty, comparative calibration experiments were conducted with a roughly prepared TLC coating and a finely prepared TLC coating under the same lighting condition (the lighting angle = 27°). Both coatings have the same thickness of 25 μm. Figure 8 shows the comparison of the hue curves of the rough coating and the fine coating. It is found that, the rough TLC coating and the fine TLC coating show different hue curves over the same monotonically calibratable temperature range. The fine TLC coating has a wider hue range, which means that the fine coating has a higher hue sensitivity to temperature and a higher resolution of the measurement.

Figure 9 shows the uncertainty in temperature measurement of the two coatings versus the actual temperature measurement. The measurement uncertainty of the fine coating ranges from 0.04℃ to 0.87℃ with a mean of 0.42℃; however, that of the rough coating ranges from 0.1℃ to 1.2℃ with a mean of 0.72℃. The fine coating shows a considerably higher measurement accuracy than the rough coating. The reason could be that compared with the fine coating, the surface of the rough coating is much rougher, and the thickness non-uniformity

produces a larger noise level. Therefore, in order to get a high measurement accuracy, a finely prepared coating should be used for the actual TLC temperature measurement application.

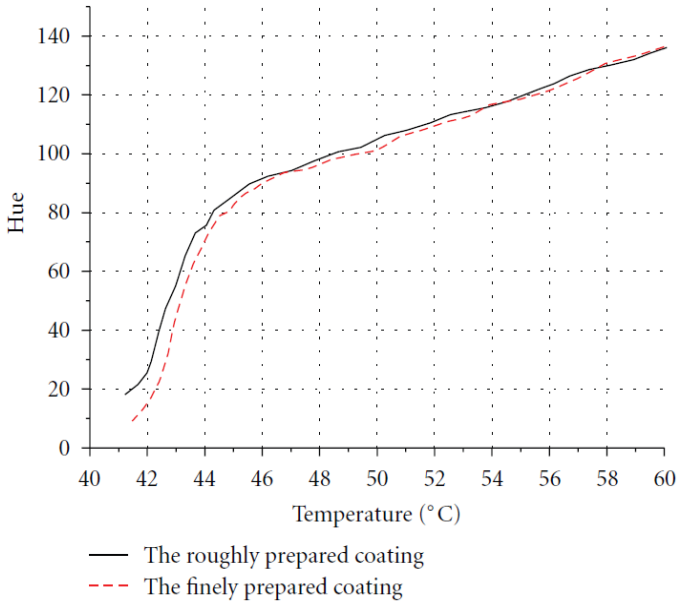

Figure B. 17: The hue curves comparison between the rough and the fine TLC coatings.[55]

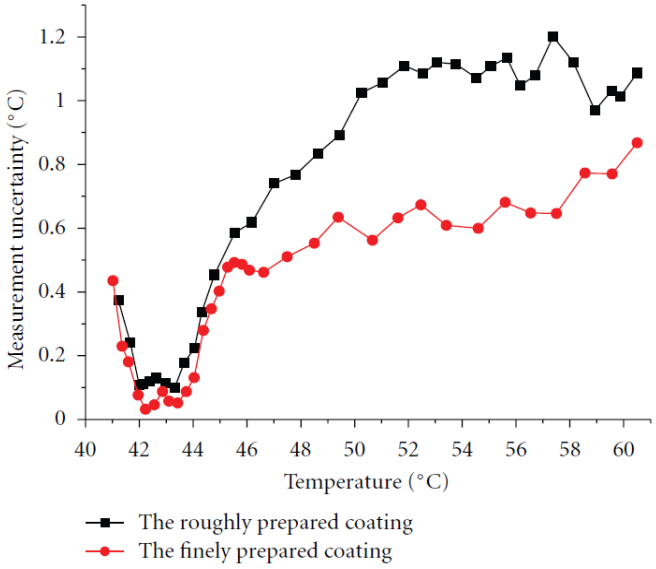

Figure B. 18 : The measurement uncertainty for the rough and fine TLC coatings.[55]

Appendix C

The measurement result on the HTC distribution is so non-uniform, does it agree with the real turbine blade application?

The measurement result on the HTC distribution is conducted using the steady state TLC technique. This approach allowed us to get an insight of the local distribution of the HTC values inside the studied TE geometry. Usually, researchers use thermocouples to estimate the temperature of a heated small plates carefully inserted inside the studied geometries (Han et al [1],] and Hwang et al [16], which is not giving the local information (Fig. C.1). In fact, each thermocouple gives a single temperature of the point where it is positioned inside the inserted heated plate. Researchers suppose that the temperature distribution is uniform along the heated plate, which is physically, and us it has been proved using the TLC technique, not real. Plates are not isotropic, and going along the plate, the heat exchange is not the same, which concludes to say that the temperature distribution over the heated plate is not the same. But, even knowing these critics, researchers were able to propose correlations of the Nusselt number of their geometries. The reported work of Hwang et al. [17] for example, show that the Nusselt number, and consequently the HTC is not uniform along the studied geometries.

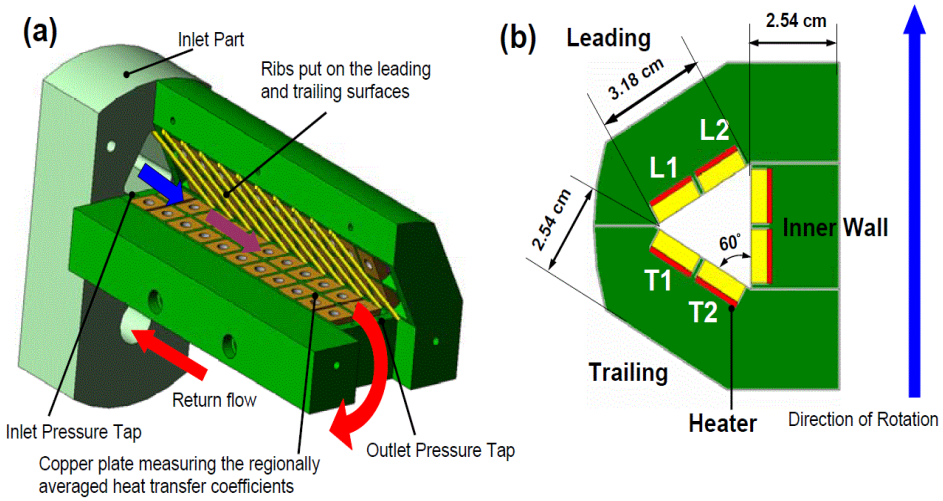

Figure C. 4: (a) Details of the trailing test section (b) Cross sectional view of the test section.

- To better compare our results to those of the open literature, we can refer to the work of Wu et al. [25] (Fig. C.2) who used TLC transient method to estimate the heat transfer coefficient at trailing edge part of the blade using a different geometry than our geometry. It can be seen clearly that the HTC distribution over the trailing edge part is not uniform as illustrated on Fig. 2 of his paper. Also, it can be concluded that our Nusselt number distribution has the same trend and range as the one reported by Wu et al. [25].

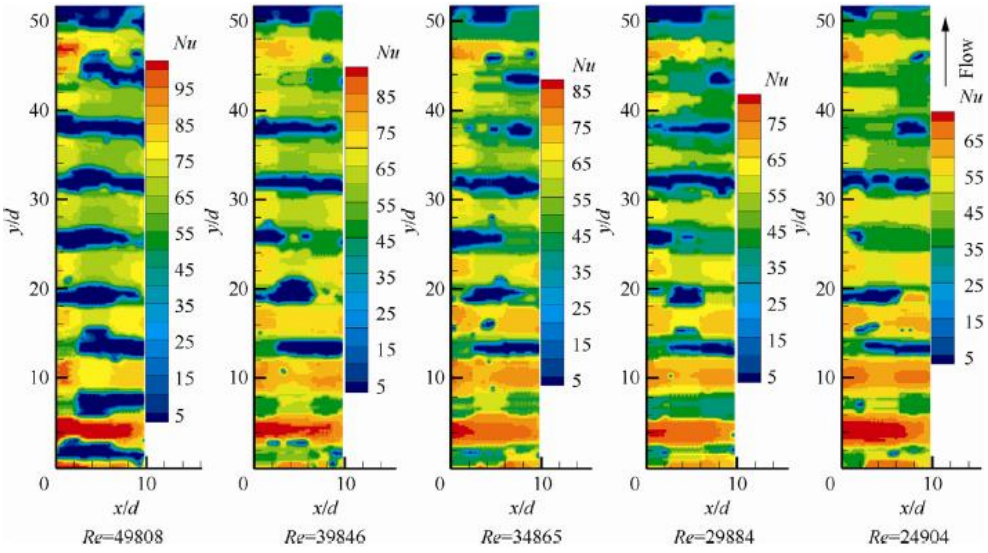

Figure C. 5 : Heat transfer contour on the section side of the second passage without bleed flow [25]

- Also, in Hwang et al. [16] the Nusselt number variation with the Reynolds number using converging duct of the trailing edge is similar to the one found in our work in term of the trend variation: augmentation of the Nusselt number with increase of the Reynolds number. Also, the Nusselt number range is between 40 and 170 (fig. C.3). In our case it is found to be between 34 and 160.

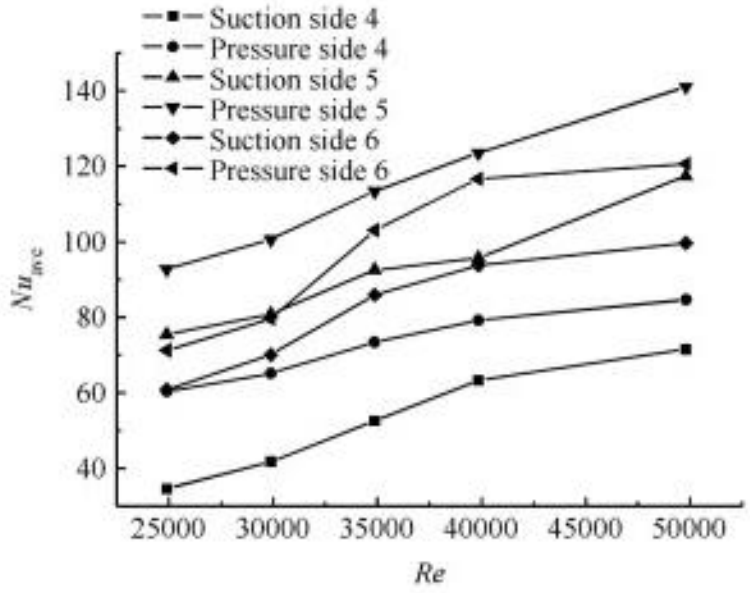

Figure C. 6 : Comparison of Nu_{ave} between the section and pressure sides. [c]

The agreement with the real gas turbines blade application, it is too hard to say if the finding results are extrapolated or not because there is always differences between the laboratory tests and the one of real application. One of reasons is that the use of PMMA instead of the real

metal's blade. Due to heat losses differences influenced by the thermal conductivity of the blade's metal.

- In our present, we followed the same steps as many other researchers, to better understand the studied phenomenon by completely a dissimilar approach. As reported in our manuscript, these results may help during the Pre-design of cooling systems procedure.

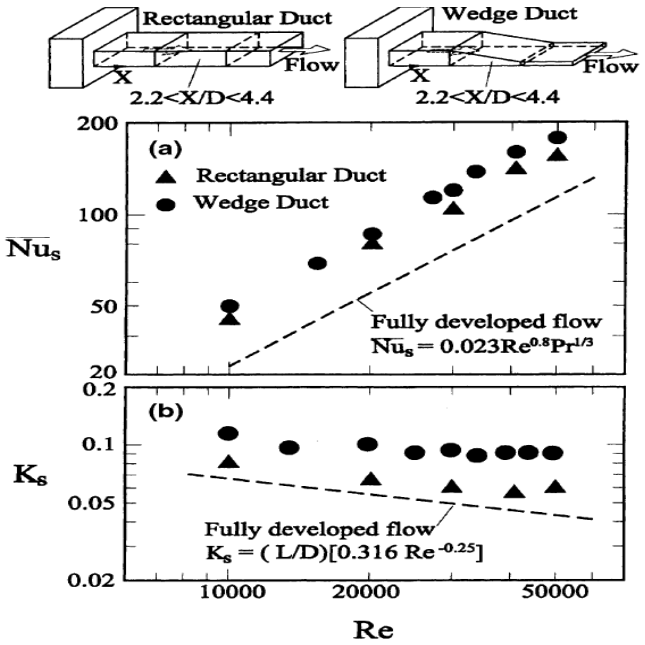

Figure C. 4. Nusselt versus Reynolds variation of TE ducts. [16]

Appendix D

What significance of this 30:1 scaled model is? Does scaling have an effect to heat transfer ?

The blade part, subject of this study, is a component of the HP stage of a gas turbine. These components, which present dimension equal to a few millimetres, are continuously in contact with coolant flows of temperatures from 600*K* up to 900*K* and pressures variable from *15 e 40 bar*. Exactly reproduce the effective machine conditions, de facto, is impossible. High pressure and high temperature and small dimensions do not give a scientific study reliable. Therefore, the will to obtain less prohibitive conditions it is necessary to impose a *scaling* of the problem, using the theory of similarity.

The Measurements obtained from a scaled models can be reported to the real object through some non-dimensional parameters as Reynolds number, Mach, Prandtl etcetera. Therefore a scaled model can be bigger than the component is reproduces, this allowing a detailed measurement. The scale is selected taking into account at the same time the dimensionless parameters and the requirement for structural strength. About subsonic flow and Mach test conditions values do not significantly influence the flow behaviour. Also, the *Pr* number depends only on the considered gas (dry air in ours experiments) and not on temperature.

With the aim of reproducing the conditions of a real engine, Reynolds and Rotation numbers were monitored, which are defined as follows:

Reynolds number: $Re = (\dot{m}D_h)/(\mu A_h)$ (D.1)

Rosby number : $Ro = \frac{\Omega . D_h}{U_b} \propto \frac{Coriolis\ Forces}{Inertial\ forces}$ (D.2)

Nusselt number $Nu = \frac{h.D_h}{k}$ (D.3)

Where Ω is the angular velocity, *Dh* is the hydraulic diameter at the inlet section and *Ub* is the bulk velocity. Typical values of Re and Ro in real cooling ducts vary from $Re \simeq 10k$ up to $Re \simeq 40k$ and $Ro = 0$ up to $Ro \simeq 0{:}4$. (we performed also Rotation cases).

Many researchers have reported that the scaling helps to develop the understanding of the gas turbines phenomenon (for example: Han et al.[3] ,Pascotto et al. [53] and Wu et al. [16]) and their researches were done using scaled models because it is too hard to get a useful information using a tiny model.

On the other hand, in the open literature; MAYINGER et al. [82] stated in his paper that:

"…The transfer of experimental results obtained under scaled conditions to the reality in an industrial plant is an old problem of engineering. There must be a sufficient similarity of the main parameters influencing the precedents in the test equipment and in the original set-up. This

similarity can be of geometrical, mechanical, static, dynamic, thermal, thermodynamic, electrical and mechanical nature.

In single phase hydrodynamics and heat transfer we are accustomed to use scalling and modelling laws since many years. The occurrences are analogous in adiabatic flow if:

The velocity field, the temperature field and the pressure field(supersonic flow) are similar. Only regarding subsonic flow the velocity and temperature fields are described by the well-known constitution laws for mass, energy and momentum. From these dimensionless numbers like :

$$\frac{x}{l}, \frac{y}{l}, \frac{z}{l}, Re = \frac{w.l}{v}, Fr = \frac{w^2}{g.l}, Eu = \frac{\Delta p}{\rho\, w^2}, Nu = \frac{h.l}{k}, Gr = \frac{l^3.g.\beta.\vartheta}{v^2}, Pr = \frac{\tau.C}{k}$$

are derived and similarity is assumed, if these dimensionless numbers are identical in the test and in the original conditions. Usually , it is easy to guarantee the geometrical similarity by choosing the same ratios of length $\frac{x}{l}, \frac{y}{l}, \frac{z}{l}$, i.e. to make all dimensions of the test object proportional to a characteristical length l of the original set-up. The other dimensionless numbers represent ratios of forces or energies (e.g. the Nusselt number) which cannot be made identical in the model and in the original as it can easily be seen from the different exponents of the parameters. The velocity is in the Reynolds number of the first power and in the Froude number of the second one. The Reynolds number is the ratio of inertia and viscous forces and the Froude number contains the Buoyancy force. This means, that in miwed convection either the forced flow or the buoyant induced one can be scaled only. In addiction the velocity and the temperature field can be influenced by the thermodynamic properties – in single phase flow mainly the viscosity, density, specific heat and thermal conductivity. …..Therefor, already in single phase flows scaling or similarity laws have a restricted and only approximate validity…. ”

Taking into account statements of F. MAYINGER **[**82**]** and knowing that our case is a subsonic flow where the Mach values do not significantly influence the flow behaviour. Moreover, the fact of using a dry air in our experiments, the Prandtl number depends only on the considered gas and not on temperature, which concludes to say that our experiments results refelect well the real gas turbine applications and may help designers during the pre-design step of internal cooling system of the trailing edge part of the blade.

ملخص:

تم تقييم الخصائص الهوائية الحرارية لحافة ذنب خاص بنظام التبريد الداخلي لشفرة تربين غازي من خلال التجريب و المحاكاة العددية في ظروف السكون و الدوران. النموذج المدروس يكمن في نسخة قياس 30 إلى1 مطابقة لممر بدون و بوجود مولدات الاضطراب مع وجود صف من 7 أعمدة عريضة .تم إختبار ستة نماذج من أجل عدد *راينولدس بين 10000 و 40000* و عدد روزبي حتى 0,23 . التجارب تم إجراؤها باستعمال تقنية البلورات السائلة ذات قاعدة كرومية حرارية و بالمقابل تم إختيار طريقة المعادلات المتوسطة لراينولدس ونافيي- ستوكس بإستعمال البرنامج Ansys Fluent و نموذج $k\ \omega -$ SST لتمثيل الإضطراب مع تدفق الهواء في حالة إستقرار متساوي الحرارة داخل الممرات في ظروف السكون و الدوران . النتائج المحصل عليها تم عرضها في شكل مخطط ثنائي الأبعاد لتوزيع معامل التبادل الحراري من جهة السطح إضافة إلى اقتراح علاقات إرتباط عدد نوسلت المتوسط كدالة ذات متغيرات: هي عدد راينولدس و عدد براندل و عدد روزبي و مسافة لا بعدية. النتائج المحصل عليها تعتبر ذات أهمية كبيرة للمصممي الشفرات التربينية الغازية.

كلمات مفتاحية: البلورات السائلة ذات قاعدة كرومية حرارية ، نظام تبريد داخلي للشفرات التربينية ، حافة الذنب لشفرة تربينية، معامل التبادل الحراري، عدد نوسلت، عدد راينولدس، عدد روزبي، التحليل العددي لديناميكا الموائع.

Résumé :

Les performances aérothermiques d'un système de refroidissement interne du bord de fuite d'une aube de turbine à gaz sont évaluées expérimentalement et numériquement dans les conditions stationnaires et rotatives. La géométrie étudiée est un modèle à échelle 30 : 1 représentative d'une conduite sans et avec perturbateurs avec une ligne de 7 vannes élargies. Six géométries sont testées par le moyen de la technique TLC pour un nombre de Reynolds entre 10000-40000 et un nombre de Rotation jusqu'à 0.23. En outre, l'analyse CFD est basée sur ANSYS-Fluent et un modèle de turbulence $k\ \omega -$ SST tout en considérant un écoulement d'air iso-thermique stationnaire à l'intérieur de la géométrie étudiée pour les conditions fixes et rotatives. Les résultats sont présentés sous forme de cartes 2D illustrant le coefficient d'échange thermique sur la surface en dépression en plus de corrélations pour le nombre de Nusselt moyenné fonction de Re, Pr, Ro et une fraction de la hauteur de l'aube. Les résultats obtenus sont d'un grand intérêt pour les concepteurs des systèmes de refroidissement pour les aubes de turbines à gaz.

Mots clés: Cristaux Liquides Thermo-chromiques, Système de refroidissement interne des aubes, Bord de fuite d'une aube, Coefficient d'échange thermique, Nombre de Nusselt, Nombre de Reynolds, Nombre de Rosby, CFD.

Abstract:

The aerothermal performances of a trailing edge internal cooling system of a high pressure gas turbine blade were evaluated experimentally and numerically in the stationary and rotating conditions. The investigated geometry consists in a 30:1 scaled model reproducing an innovative typical wedge shaped discharge ribbed duct, with one row of 7 enlarged pedestals. Six different cooling schemes were tested based on TLC technique, at Reynolds number in between 10000-40000 and Rotation number up to 0.23. On the other hand, CFD analysis used commercial ANSYS-Fluent solver based on $k\ \omega -$ SST turbulence model and an isothermal steady air flow inside the studied geometry for both the stationary and rotating conditions. The obtained results are reported in terms of 2D maps of HTC plotted on the suction side surface and correlations of averaged Nusselt number as function of *Re, Pr, Ro* and a fraction of the blade height. The obtained results are useful to the designers of gas turbine blades cooling systems.

Keywords: Blades cooling system, Internal cooling, Blade trailing edge, Thermo-chromic liquid crystals, Heat transfer coefficient, Nusselt Number, Reynolds number, Rotation number, CFD.